

**Simulations of the Compact Toroidal Hybrid Using the Finite Element  
Extended MHD Code NIMROD**

by

Jonathan Hebert

A dissertation submitted to the Graduate Faculty of  
Auburn University  
in partial fulfillment of the  
requirements for the Degree of  
Doctor of Philosophy

Auburn, Alabama  
August 1, 2015

Keywords: Stellarator, Torsatron, NIMROD, CTH

Copyright 2015 by Jonathan Hebert

Approved by

James D. Hanson, Chair, Professor of Physics  
David Ennis, Assistant Professor of Physics  
Yu Lin, Professor of Physics  
Kaijun Liu, Assistant Professor of Physics  
David Maurer, Associate Professor of Physics

## Abstract

Magnetohydrodynamic (MHD) modeling of magnetic confinement devices is an important tool in the understanding of plasma processes. With the nearly axisymmetric tokamak being the leading candidate for a plasma fusion reactor, much of the work in plasma modeling has been focussed on two-dimensional modeling. Recently, the importance of three-dimensional effects has become apparent in the control of disruptive modes such as the Edge Localized Mode (ELM)<sup>1,2</sup> and the resistive wall mode<sup>3,4</sup>. Thus modeling of three-dimensional plasma configurations is a critical step forward in the process of designing a viable plasma fusion reactor.

This dissertation describes modeling of the Compact Toroidal Hybrid (CTH) stellarator/tokamak hybrid at Auburn University using the extended MHD code NIMROD.<sup>5</sup> The CTH has a high degree of toroidal shaping and a circular boundary and is thus a good candidate for modeling with NIMROD. Building on initial work by Schlutt et al.,<sup>6</sup> ohmic heating, temperature dependent thermal diffusivity, initial temperature and density profiles, temperature dependent resistivity, and time dependent loop voltages were added to the model to increase physical fidelity. This updated model is used to investigate current hesitations in the current rise of CTH discharges.

Initial modeling shows large, symmetry-breaking islands growing with an  $m = 2, n = 1$  structure. These islands have a large effect on plasma current and temperature profiles and the growth rate of the associated magnetic mode scales similarly to the resistive interchange mode ( $\gamma \sim \eta^{1/3}$ ). The growth of large islands for lower rotational transforms is investigated using the driving loop voltage as a feedback mechanism to keep the total plasma current constant. Doing this, symmetry-breaking islands formed for  $\iota = 1/3$ , but the growth time-scale was much longer than the time-scale of hesitations in the experiment. To sharpen edge

gradients, the perpendicular thermal diffusivity was lowered. This change greatly affected the current drive, causing symmetry-breaking islands to grow for rotational transforms as low as  $\iota = 1/10$ .

## Acknowledgments

I would like to begin by thanking my friends. Whether helping me talk through a problem or being there to let me blow off some steam, I know I can always count on them. My time in graduate school would have been much less enjoyable without them.

This work would not have been possible without the help of Jacob King, Scott Kruger, and Carl Sovinec of the NIMROD team. Their help in the running and interpretation of NIMROD was invaluable.

Most of all, I would like to thank all of my family members, but especially my mom and dad. Through all the highs and lows, my parents have been behind me, encouraging and supporting. There is no way I would be where I am today without their love and support, and words cannot express how appreciative I am.

This material is based upon work supported by the U.S. Department of Energy, Office of Science, Office of Fusion Energy Sciences under Award Number DE-FG02-03ER54692.

This research used resources of the National Energy Research Scientific Computing Center, a DOE Office of Science User Facility supported by the Office of Science of the U.S. Department of Energy under Contract No. DE-AC02-05CH11231.

## Table of Contents

Abstract . . . . .	ii
Acknowledgments . . . . .	iv
List of Figures . . . . .	viii
List of Tables . . . . .	xvi
1 Motivation . . . . .	1
1.1 Expansion of NIMROD stellarator modeling . . . . .	1
1.2 Investigation of current ramp dynamics . . . . .	2
1.3 Dissertation organization . . . . .	4
2 CTH and NIMROD . . . . .	5
2.1 Plasma fusion . . . . .	5
2.2 Confinement schemes . . . . .	6
2.2.1 Tokamak . . . . .	7
2.2.2 Stellarator . . . . .	8
2.2.3 Compact Toroidal Hybrid (CTH) . . . . .	9
2.3 Modeling efforts . . . . .	12
2.3.1 The NIMROD code . . . . .	12
2.4 CTH/NIMROD model . . . . .	14
3 The Physics Model . . . . .	16
3.1 Initial model . . . . .	16
3.2 Adding ohmic heating . . . . .	18
3.3 Adding temperature dependent thermal diffusivity . . . . .	19
3.4 Adding initial temperature and density profiles . . . . .	22
3.5 Adding temperature dependent resistivity . . . . .	25

3.6	Adding time dependent loop voltage . . . . .	27
4	Comparison of Full Model To Experiment . . . . .	29
4.1	Model of shot 13030823 . . . . .	29
4.1.1	Introduction and shot overview . . . . .	29
4.1.2	Goals of run . . . . .	31
4.1.3	Model specifics . . . . .	31
4.1.4	Presentation of results . . . . .	35
4.2	Constant current investigation of island growth . . . . .	49
4.2.1	Introduction and motivation . . . . .	49
4.2.2	Model specifics . . . . .	49
4.2.3	Presentation of results . . . . .	50
4.3	Decreasing perpendicular thermal transport . . . . .	54
4.3.1	Introduction and motivation . . . . .	54
4.3.2	Model specifics . . . . .	55
4.3.3	Presentation of results . . . . .	55
5	Results, conclusions, and discussion . . . . .	65
5.1	Model changes . . . . .	65
5.1.1	Additional physics . . . . .	65
5.1.2	Plasma initialization . . . . .	66
5.2	Computational results . . . . .	67
5.2.1	CTH model with improvements . . . . .	67
5.2.2	Constant current run . . . . .	68
5.2.3	Lower perpendicular thermal conductivity . . . . .	68
5.3	Further work . . . . .	69
	Appendices . . . . .	72
A	Synthetic Diagnostics - NIMNOSTICS . . . . .	73
A.1	Introduction . . . . .	73

A.2	Code structure . . . . .	73
A.3	Example . . . . .	74
B	NIMROD Calculation of Rotational Transform . . . . .	76
B.1	Separation of field lines . . . . .	77
B.2	Centroid calculation . . . . .	77
B.3	Magnetic axis choice . . . . .	78
B.4	Calculation of “poloidal” angle . . . . .	78
B.5	Calculation of rotational transform . . . . .	78
C	Using NIMROD to model CTH . . . . .	80
C.1	Initial magnetic field . . . . .	80
C.1.1	mgrid . . . . .	80
C.1.2	Importing to NIMROD . . . . .	81
C.2	Initial temperature profile . . . . .	84
C.3	Initial density profile . . . . .	86
C.4	Final suggestions . . . . .	87
	Bibliography . . . . .	88

## List of Figures

1.1	Measured plasma current (blue) and edge rotational transform (red, horizontal lines for $\iota = 1/7, 1/6, 1/5, 1/4,$ and $1/3$ ) as calculated by V3FIT in a CTH shot. Note the hesitations in current drive, and their coincidence with rational values of edge rotational transform. . . . .	2
2.1	Conceptual drawing of the ITER tokamak, currently under construction. Note the toroidal uniformity of the vacuum vessel. (©ITER Organization, 2011) . . .	7
2.2	CAD model of the Wendeslstein 7-X stellarator. Note the irregularity of the confining coils (dark blue) and the shaping of the resulting plasma (yellow). Reprinted from “Status of Wendelstein 7-X Construction,” by L. Wegener, 2009, <i>Fusion Engineering and Design</i> , Vol. 84, No 2-6, Pgs. 106-112. Copyright 2009 by Elsevier Limited. Reprinted with permission. . . . .	10
2.3	The Compact Toroidal Hybrid magnetic field coils. Red - Helical Field; Yellow - Toroidal Field; Green - Ohmic Transformer; Gray - Error Correction Coils; Blue - Vertical Field. The 3D shaping of the helical field coil results in a five-fold periodicity in CTH plasmas. . . . .	11
2.4	A circular cross section divided (upper left), transformed into logical space (upper right), and an individual cell with all quadrature points shown for $N_p = 2$ . . . .	15
3.1	Comparison of NIMROD (blue) and CTH (red) vacuum flux surfaces at a full (left) and half (right) field period . . . . .	17



3.2	Current density (black) and temperature (red) at 1ms for a simulation with ohmic heating, a constant electrical diffusivity of $630\text{m}^2/\text{s}$ , and a constant loop voltage of 1V. These values were chosen for illustrative purposes and do not reflect experimental conditions. Note the effect of ohmic heating: increasing temperature in regions where plasma current is driven. Also note the anomalous heating near $r = 0.5\text{m}$ . . . . .	20
3.3	Current density (black) and temperature (red) at 1ms for a simulation with ohmic heating, a constant electrical diffusivity of $630\text{m}^2/\text{s}$ , a constant loop voltage of 1V, and anisotropic heat conduction, with $\kappa_{\parallel}/\kappa_{\perp} = 10^5$ . These values were chosen for illustrative purposes and do not reflect experimental conditions. The anomalous heating from figure 3.2 has been remedied by the parallel heat conduction. Note also the effect of the perpendicular heat conduction, smoothing the temperature to a peaked profile. . . . .	23
3.4	Evolution of temperature when setting an initial temperature profile. This simulation only evolves the temperature, with no plasma current being driven. (a) The desired maximum temperature is set over the domain except the wall, which is kept cold. (b) The temperature evolves with anisotropic thermal diffusivity. Heat on open field lines flows to the cold boundary, heat on closed field lines stays in plasma volume. (c) Final state used as initial conditions in model. . . .	25
3.5	Comparison of perturbed (orange) and unperturbed (blue) loop voltage. Note the lower amplitude of and wiggles in the perturbed loop voltage. The diagnostic which measures the loop voltage also captures the response of the plasma to the ohmic drive. . . . .	28

4.1 Overview of CTH shot 13030823 showing measured plasma current (top), measured  $dB_{\theta}/dt$  (middle), and V3FIT calculated edge rotational transform (bottom). The hesitations in plasma current are reflected in the  $dB_{\theta}/dt$  signal as fluctuations. During current hesitations, V3FIT calculates the rotational transform at the edge of the plasma to be near a low-order rational value. . . . . 30

4.2 Measured line-averaged electron density from an interferometer for a chord at the mid-plane (black) and equidistant above (red) and below (blue) the mid-plane for the full shot (a) and the current ramp phase (b). . . . . 33

4.3 Effect of varying background densities on the rate of ohmic current drive at  $T = 0$  eV to drive as little plasma current as possible. At  $n = 10^{17}\text{m}^{-3}$  (blue) and  $n = 10^{18}\text{m}^{-3}$  (orange) the modeled plasma current overtakes experiment (black) while for  $n = 10^{19}\text{m}^{-3}$  (purple) it does not. . . . . 33

4.4 Plasma current comparison between experiment (black) and NIMROD with initial peak temperature of 30 eV (red), 25 eV (green), 20 eV (purple), 15 eV (gray), 10 eV (orange) and 5 eV (blue). 30 eV was chosen over 25 eV as the initial temperature for the modeling in section 4.1.4 due to the favorable comparison with experimental values later in time. . . . . 34

4.5 Comparison of plasma current from experiment (black) with NIMROD model (orange). The plasma current matches well early in time, but as hesitations are missed in the model, the currents begin to diverge. Vertical lines represent times shown in later time sequence figures. . . . . 35

4.6 Comparison of rotational transform as calculated by V3FIT (blue) and NIMROD (orange) early in the current ramp. Though the NIMROD model misses the current hesitations seen in experiment and reflected in V3FIT, the rotational transform matches well between NIMROD and V3FIT. Note the greater extent of the NIMROD profiles as well as the downward turn near the edge of the V3FIT profiles. These are thought to be caused by the absence of physical limiters in the NIMROD model. . . . . 36

4.7 Time sequence of surface of section plots early in the current ramp at  $\phi = 0$ . Though many rational values of  $\iota$  are being traversed, so magnetic islands grow in the plasma volume. . . . . 38

4.8 Time sequence of surface of section plots late in the current ramp at  $\phi = 0$ . A symmetry-preserving  $m = 15, n = 5$  island chain grows in the plasma, as seen in (b). The growth of this chain begins more island growth, with an  $m = 5, n = 2$  and an  $m = 12, n = 5$  chain growing in (d) and (e). An  $m = 2, n = 1$  island grows near the magnetic axis in (f). . . . . 39

4.9 Time sequence of parallel plasma current density ( $\lambda = \mu_0 \mathbf{J} \cdot \mathbf{B} / B^2$ ) early in the current ramp at  $\phi = 0$ . The current forms a hollow profile. . . . . 40

4.10 Time sequence of parallel plasma current density ( $\lambda = \mu_0 \mathbf{J} \cdot \mathbf{B} / B^2$ ) late in the current ramp at  $\phi = 0$ . As islands grow in the plasma, they have a noticeable effect on the plasma current density profiles. When islands are small and symmetry-preserving, the edge of the current density profile becomes wavy, as is seen in (a)-(d). As the islands, grow, so does their effect on the plasma current, as seen in (e) and (f). . . . . 41

4.11	Time sequence of temperature early in the current ramp at $\phi = 0$ . The perpendicular thermal diffusivity and initial temperature profile create a peaked temperature profile from the hollow current density profiles of figure 4.9. . . . .	42
4.12	Time sequence of temperature late in the current ramp at $\phi = 0$ . As islands grow in the plasma, they have a noticeable effect on the temperature profiles. These effects are not as marked as in the current density profiles of figure 4.10, however.	43
4.13	Growth of magnetic energy for $n = 1$ (red) and $n = 2$ (blue) as a function of time. The magnetic energy growth in these two modes is representative for all modes $n = 5j \pm 1$ and $n = 5j \pm 2$ (see figures 4.14 and 4.15). A symmetry-preserving $m = 15, n = 5$ island is seen beginning at $t = 4.4$ ms. . . . .	45
4.14	Growth of magnetic energy for $n = 5j \pm 1$ with $j = 1, 2, 3, 4$ . All of the modes follow behavior similar to the $n = 1$ toroidal mode, seen in figure 4.13. . . . .	46
4.15	Growth of magnetic energy for $n = 5j \pm 2$ with $j = 1, 2, 3, 4$ . All of the modes follow behavior similar to the $n = 2$ toroidal mode, seen in figure 4.13. . . . .	47
4.16	Dependence of growth rate of $n = 5j \pm 1$ magnetic mode on resistivity. The fit line has a slope of $\gamma = 0.337$ . The growth rate of the observed magnetic mode varies similarly to that of the resistive interchange mode ( $\gamma = \eta^{1/3}$ ). . . . .	48
4.17	Loop voltage (left) and plasma current (right) for simulation holding $I_p$ constant. The loop voltage control given in equation 4.8 is activated at the dashed line. . . . .	50

4.18 Time sequence of surface of section plots at  $\phi = 0$  for constant  $I_p$  simulation showing the growth and merging of  $\iota = 1/3$  islands. Red surfaces have rotational transform  $\iota = 1/3 \pm 0.005$ . (b) The  $\iota = 1/3$  surface enters in a wide band in the middle of the plasma with an  $m = 15, n = 5$  island formed near the edge of that region. (c)-(d) Increasing rotational transform splits the  $\iota = 1/3$  surface in two. (e) The  $m = 15, n = 5$  island begins to merge. (f) The fully merged  $m = 3, n = 1$  island. . . . . 51

4.19 Closeup at  $\phi = 0$  of one set of islands merging showing only selected surfaces. Red surfaces have rotational transform  $\iota = 1/3 \pm 0.005$ . (a) The  $\iota = 1/3$  surface forms an  $m = 15, n = 5$  island chain. (b) The chain begins merging, with the middle three islands combining first. (c) The outer islands combine with the inner islands and the  $\iota = 1/3$  surface now forms an  $m = 3, n = 1$  chain. . . . . 52

4.20 Growth of magnetic energy for  $n = 1$  (red) and  $n = 2$  (blue) as a function of time. As in figure 4.13, the magnetic energy growth in these two modes is representative for all modes  $n = 5j \pm 1$  and  $n = 5j \pm 2$ . . . . . 53

4.21 Comparison of plasma current from experiment (black) and from NIMROD model with lowered value of perpendicular thermal diffusivity for initial peak temperatures of  $T = 30\text{eV}$  (blue) and  $T = 15\text{eV}$  (orange). The lower  $\kappa_{\perp}$  drives current in the model faster than before. To agree with the rate of plasma current drive in experiment, the peak of the initial temperature profile must be lowered to 15 eV. . . . . 56

4.22 Plasma current comparison between experiment (black) and NIMROD model with a lowered value of perpendicular thermal transport (orange). As in 4.5, the NIMROD plasma current matches well early in time with the experimental plasma current. As hesitations are missed in the model, however, the currents diverge. . . . . 58

4.23 Current comparison highlighting times in which the  $t = 1/9$  (between dashed lines),  $t = 1/8$  (between dotted lines), and  $t = 1/7$  (between dot-dashed lines) island chains are at the edge of the plasma. The times when these symmetry breaking islands appear near the edge of the plasma correspond well to the times of early hesitations in experiment. . . . . 59

4.24 Surface of section plots at  $\phi = 0$  for a lower value of perpendicular thermal diffusivity. Symmetry-breaking magnetic islands appear early in the model, with  $t = 1/9$  shown in (b)-(c),  $t = 1/8$  shown in (d)-(e), and  $t = 1/7$  and  $t = 1/6$  shown in (f). . . . . 60

4.25 Time sequence of current density ( $\lambda = \mu_0 \mathbf{J} \cdot \mathbf{B}/B^2$ ) contours at  $\phi = 0$  for a lower value of perpendicular thermal transport. The current is driven in a hollow profile, similar to figure 4.9, but the profiles are heavily affected by the presence of magnetic islands. . . . . 61

4.26 Time sequence of temperature contours at  $\phi = 0$  for a lower value of perpendicular thermal transport. The temperature profiles are heavily affected by the presence of magnetic islands. The lower value of  $\kappa_{\perp}$  keeps heat closer to where it is generated, resulting in changing the initially peak profile in (a) to the hollow profile in (f). . . . . 62

4.27 Growth of magnetic energy for  $n = 1$  (red) and  $n = 2$  (blue) as a function of time for model with lower value of perpendicular thermal diffusivity. As in figure 4.13, the magnetic energy growth in these two modes is representative for all modes  $n = 5j \pm 1$  and  $n = 5j \pm 2$ . . . . . 63

4.28 Dependence of growth rate of  $n = 5j \pm 1$  magnetic mode on resistivity. The fit line has a slope of  $\gamma = 0.330$ . The growth rate of the observed magnetic mode varies similarly to that of the resistive interchange mode ( $\gamma = \eta^{1/3}$ ). . . . . 64

5.1	Location and extent of molybdenum limiter at $\phi = 348^\circ$ overlaid on current density ( $\lambda = \mu_0 \mathbf{J} \cdot \mathbf{B} / B^2$ ) contours at the same angle. Note the overlap of the limiter and the plasma current. This shorter path to the boundary could reduce the driven plasma current, possibly producing hesitations. . . . .	71
A.1	Chords of the three-channel interferometer on CTH. . . . .	75
B.1	“Poloidal” angle as a function of puncture number . . . . .	79
C.1	The NIMROD grid produced by the inputs in table C.1 representing CTH. The uneven spacing of the nodes is due to setting <code>poly_distribution='gll'</code> . This setting uses Gauss-Lobatto spacing which can result in better conditioned matrices for the large values of <code>lphi</code> necessary for CTH runs. . . . .	83

## List of Tables

C.1	<code>&amp;grid_input</code> variables describing the NIMROD mesh . . . . .	81
C.2	<code>&amp;physics_input</code> variables for loading fields into NIMROD . . . . .	82
C.3	<code>&amp;numerical_input</code> variables for loading fields into NIMROD . . . . .	82
C.4	<code>&amp;closure_input</code> variables for loading fields into NIMROD . . . . .	82
C.5	<code>&amp;equil_input</code> variables for setting the initial magnetic field . . . . .	84
C.6	<code>&amp;closure_input</code> variables for setting the initial magnetic field . . . . .	84
C.7	<code>&amp;numerical_input</code> variables for controlling the length of the simulation . . . . .	84
C.8	<code>&amp;init_input</code> variables for resetting from a dump file . . . . .	84
C.9	<code>&amp;equil_input</code> variables for setting an initial temperature profile . . . . .	85
C.10	<code>&amp;numerical_input</code> variables for setting an initial temperature profile . . . . .	85
C.11	<code>&amp;closure_input</code> variables for setting an initial temperature profile . . . . .	85
C.12	<code>&amp;equil_input</code> variables for advancing an initial temperature profile . . . . .	85
C.13	<code>&amp;closure_input</code> variables for advancing an initial temperature profile . . . . .	86
C.14	<code>&amp;init_input</code> variables for resetting from a dump file . . . . .	86
C.15	<code>&amp;equil_input</code> variables for setting an initial density profile . . . . .	86
C.16	<code>&amp;closure_input</code> variables for setting an initial density profile . . . . .	86
C.17	Common pitfall variables . . . . .	87



## Chapter 1

### Motivation

This brief chapter will serve as a motivation and overview of the work contained in this document. See chapter 2 for a more in-depth introduction.

#### 1.1 Expansion of NIMROD stellarator modeling

The NIMROD (Non-Ideal Magnetohydrodynamics with Rotation, Open Discussion) code<sup>5</sup> is a three-dimensional magnetohydrodynamics (MHD) code used extensively for the study of plasmas. NIMROD is used to model plasmas ranging from space plasmas to fusion relevant plasmas.<sup>7,8,9,10</sup> Of particular interest are the fusions studies undertaken with NIMROD.

Modeling stellarators is difficult due to the high degree of non-axisymmetry inherent to the configuration. Equilibrium codes such as VMEC<sup>11</sup> simplify the problem by making assumptions such as the presence of closed flux surfaces. As experiments become more sophisticated, however, it is seen that effects such as magnetic islands and stochastic regions, which do not fit the assumption of closed flux surfaces, are important in fully explaining experimental observations.

Some initial work studying the Compact Toroidal Hybrid (CTH) with NIMROD was done by Schlutt et al.<sup>6</sup> By inducing a current in a zero- $\beta$  model, they saw a hollow current profile form. This current produced magnetic islands in the plasma which preserved the five-fold periodicity inherent to the CTH system. Depending on the strength of the current drive, these islands could coalesce into larger islands which broke the periodicity of the machine and, eventually, reduced the confinement properties of the plasma.

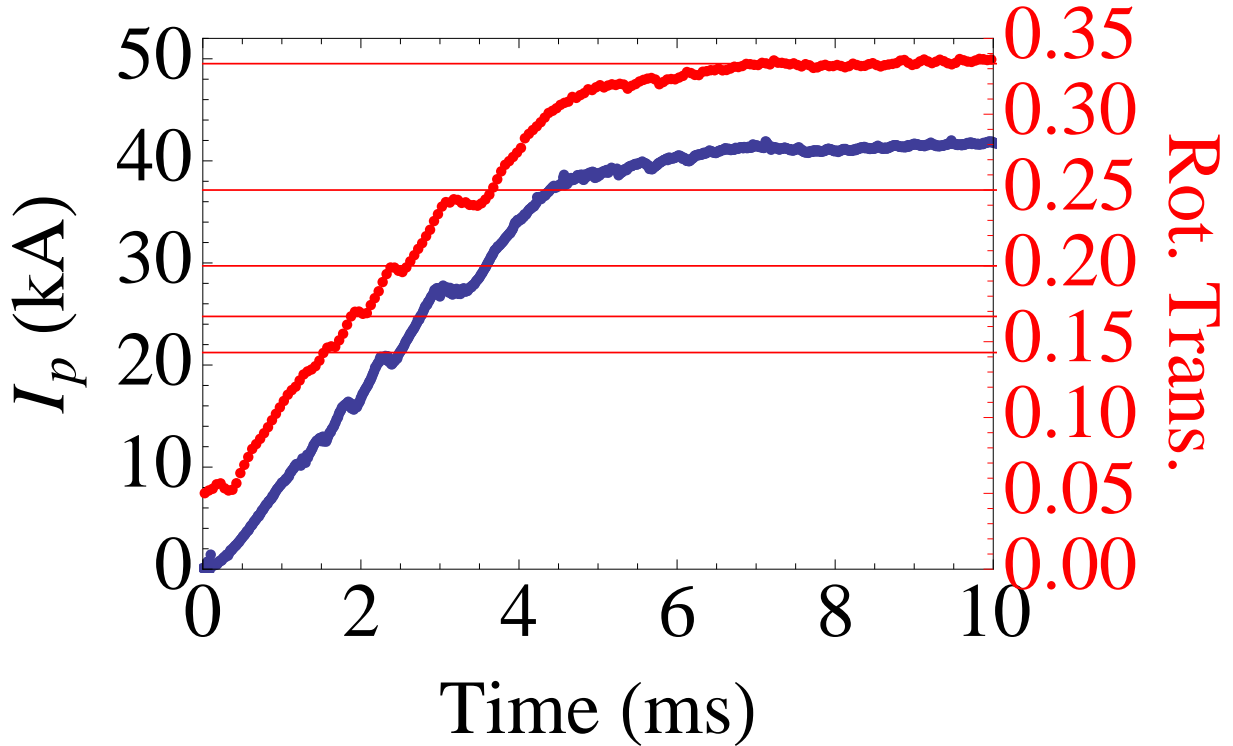


Figure 1.1: Measured plasma current (blue) and edge rotational transform (red, horizontal lines for  $\iota = 1/7, 1/6, 1/5, 1/4,$  and  $1/3$ ) as calculated by V3FIT in a CTH shot. Note the hesitations in current drive, and their coincidence with rational values of edge rotational transform.

This work aims to improve on that modeling. Where the original study used a simplified plasma model, this work brings the model closer to experimental reality through the inclusion of ohmic heating, temperature dependent thermal diffusivity, initial temperature and density profiles, temperature dependent resistivity, and a time dependent loop voltage.

## 1.2 Investigation of current ramp dynamics

In CTH, a typical ohmic shot proceeds as follows:

1. Magnetic field coils are energized, setting a stellarator field which persists throughout the shot

2. Microwaves are fired into the machine, serving the dual purpose of ionizing the neutral gas in the machine and heating the electrons through Electron Cyclotron Resonance Heating (ECRH)
3. A capacitor bank is discharged through a central solenoid in the machine, inducing toroidal current in the plasma

In the first few moments after the ohmic coil is discharged, hesitations are observed in the driven current. As can be seen in figure 1.1, these hesitations are believed to occur when the edge rotational transform is near a rational value, evidenced by V3FIT<sup>12</sup> reconstructions.

Hesitations such as these have been observed before in other current carrying plasma systems. It is generally accepted that these hesitations are the result of reconnection events in the interior of the plasma, relaxing a hollow current profile to a peaked profile<sup>13,14</sup>. Scarabosio et al.<sup>15</sup> studied this phenomenon in TCV and found that these hesitations coincide with low-order rational values of edge safety factor  $q_a$ . With the dominant mode numbers of the instabilities  $m/n = q_a$ , a connection with the external-kink mode was posited. Given the proper conditions, these non-disrupting modes have been observed to couple with the  $m = 2, n = 1$  mode, causing disruptions. It was found that plasma shaping (both elongation and triangularity) stabilized this disruptive mode. Bonfiglio et al.<sup>16</sup> studied the transitional regime between tokamaks and reversed-field pinches, seeing, in both experiment and modeling, hesitations in the current driven. Modeling showed that these hesitations occurred when the edge safety factor was a low order rational and could be suppressed by increasing the current drive before onset. In the modeling, a self-reorganization of the plasma flux was observed and the hesitations in driven current were attributed to this phenomenon.

Calculations modeling this phenomenon in the CTH geometry could shed some light on the effect of three-dimensional fields on these hesitations. In previous work, Scarabosio et al.<sup>15</sup> used the resistive stability code PEST-3<sup>17</sup> to study the effect of shaping on current rise instabilities and disruptions. In the modeling, they found that plasma shaping tended to destabilize the disruptive mode observed in experiment, attributing the disparity between

model and experiment to the lack of wall interaction and vacuum mode coupling in the model. While NIMROD does not fully address the lack of wall interaction, vacuum modes are allowed to couple to the plasma in NIMROD, and a time-dependent non-linear calculation may shed more light on the effect of shaping.

### **1.3 Dissertation organization**

The remainder of this document is organized as follows:

- Chapter 2 gives an overview of confinement schemes, focussing specifically on CTH and the role it plays in fusion research as well as giving a more in-depth discussion of NIMROD.
- Chapter 3 details the specifics of the physics model used in NIMROD to model CTH as well as highlighting features implemented to this end.
- Chapter 4 details the results of experiments in modeling the current rise phase of CTH shots.
- Chapter 5 gives a review and discussion of this work, as well as offering suggestions for future work.

## Chapter 2

### CTH and NIMROD

Fossil fuels have been providing the energy which has powered the world for the past century. New concerns over global climate change, as well as the finiteness of the resource and the political instability which often accompanies production, have renewed calls for an alternate source of clean, plentiful, abundant energy. Plasma fusion promises to provide this fuel for the future.

#### **2.1 Plasma fusion**

Nuclear fusion is the process by which two or more nuclei combine into a single, larger nucleus. This results in a release of energy if the resulting nucleus is lighter than the total mass of the original nuclei. Extreme conditions are required to overcome the electrostatic repulsion between nuclei. In the center of the Sun, where the process of nuclear fusion takes place many times every day, gravity provides the conditions necessary to overcome the electrostatic repulsion between nuclei and creates an environment conducive to fusion.

Plasma is often called the fourth state of matter, and can be described as an ionized gas which exhibits collective behavior. As plasmas are, by definition, ionized and the charge carriers are free to move about, plasmas are electrically conductive. Plasmas exist in many forms in nature; from lightning to the Earth's magnetosphere to interstellar nebulae.

Fusion requires extreme conditions due to the electrostatic repulsion between nuclei. In fusion research these conditions are typically obtained through high temperatures. These high temperatures increase the chance of fusion by giving particles in the high-energy tail of the thermal velocity distribution enough kinetic energy to overcome electrostatic repulsion. High temperatures, however, are not enough to create fusion. It is also necessary to keep

nuclei in close proximity to each other for long enough that random thermal collisions will result in fusion events. These two, often competing, considerations are brought together in a measure called the Lawson criterion<sup>18</sup> which determines the minimum temperature and confinement time needed to achieve sustained fusion. The Lawson criterion for the deuterium-tritium (D-T) reaction is given by

$$n\tau_E \geq \frac{12}{E_{ch}} \frac{k_B T}{\langle \sigma v \rangle}, \quad (2.1)$$

where  $n$  is the plasma density,  $T$  is the temperature,  $\tau_E$  is the energy confinement time-scale,  $k_B$  is the Boltzmann constant,  $E_{ch}$  is the energy of the electrically charged products of a fusion reaction, and  $\langle \sigma v \rangle$  denotes an average over a Maxwellian in velocity space of the fusion cross-section ( $\sigma$ ) and the relative velocity ( $v$ ).

Cold plasmas such as those found in fluorescent lights can be confined simply by materials such as glass. Material confinement is not possible, however, at the extreme conditions needed for fusion. In the sun, gravity confines the plasma. This combination of long confinement times and high temperatures easily satisfies the Lawson criterion. Since it is not possible to use gravity to bind such a system on Earth, other forms of confinement must be explored.

## 2.2 Confinement schemes

Research into plasma fusion is chiefly split into two areas: magnetic confinement and inertial confinement.

Magnetic confinement is achieved by using magnetic fields to confine the plasma in a configuration conducive to achieving fusion. As charged particles tend to travel along magnetic field lines, these devices are often formed into a torus to mitigate the loss of hot particles on open magnetic field lines, increasing the confinement time. This increase in confinement time allows magnetic confinement machines to run at relatively lower temperatures than

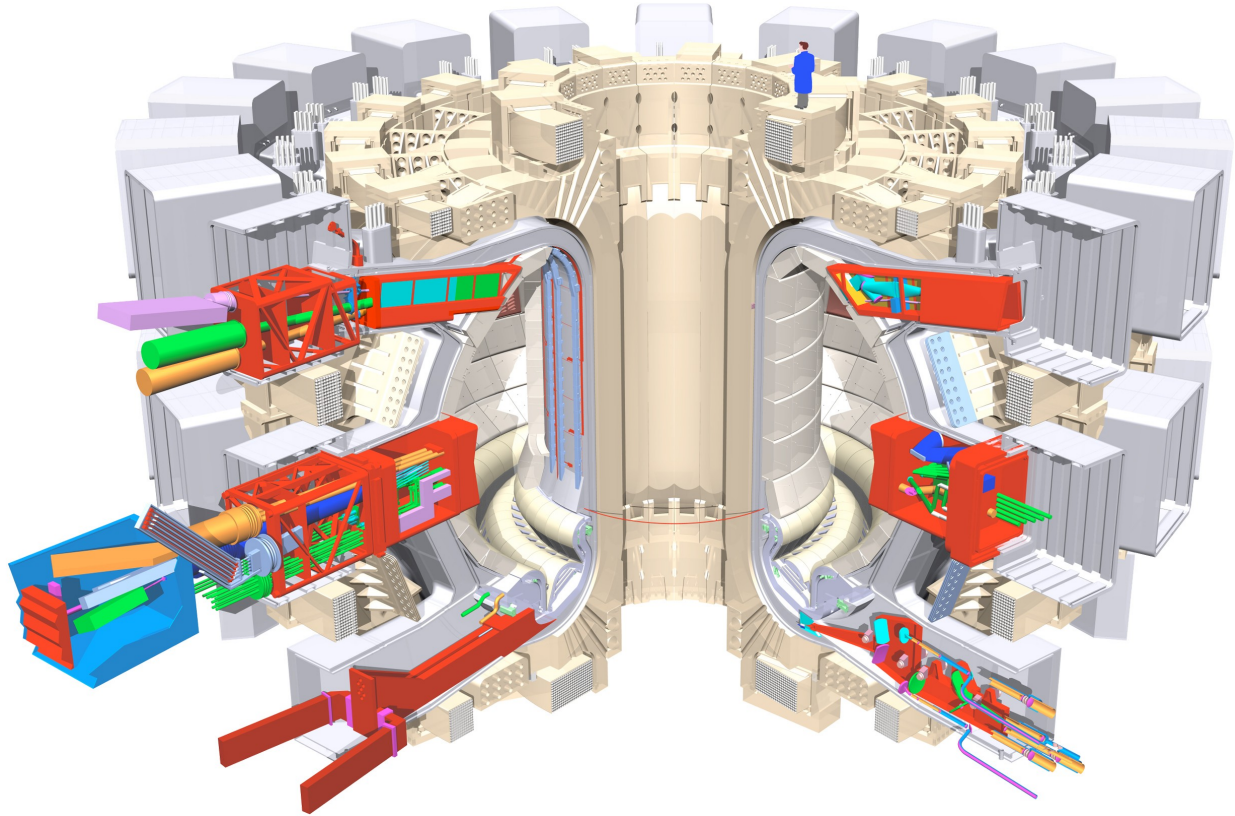


Figure 2.1: Conceptual drawing of the ITER tokamak, currently under construction. Note the toroidal uniformity of the vacuum vessel. (©ITER Organization, 2011)

inertial confinement machines. Inertial confinement involves simultaneously heating and compressing a source of light nuclei with lasers to achieve the required conditions. Though the confinement time is short, the Lawson criterion is satisfied through the extremely high temperatures and densities obtained in the compression. This work focuses on the former method, and, in particular, a combination of two toroidal confinement schemes: the stellarator and the tokamak.

### 2.2.1 Tokamak

Confining magnetic fields in a tokamak are provided by a combination of external coils and an internally driven current. This current also provides heat to the plasma through ohmic

heating. This scheme is the leading candidate for a fusion reactor, with the experimental reactor ITER currently under construction.<sup>19</sup>

That current must be driven in a tokamak is hugely advantageous. Firstly, poloidal fields, which are necessary for plasma confinement, are difficult to produce externally. Given a toroidal guide field, the current driven in the plasma provides the necessary poloidal field, thus greatly simplifying the engineering of the machine. Also, because of the electrical resistance of the plasma, the current heats the plasma through the process of ohmic heating. This heating, while not sufficient to heat the plasma to ignition, gives a jump start to the heating process, carrying some of the load that supplemental heating methods would need to provide. The tokamak is also inherently nearly axisymmetric, i.e. if one were to look at two different poloidal cross-sections, the plasma would be nominally the same. This fact greatly reduces the complexity involved in modeling tokamak plasmas.

Though favored by many for fusion power generation, the tokamak has inherent instabilities which can make it violently disrupt. While the driven current provides some benefits as described above, it also complicates things by its necessity by making the plasma unstable to current driven instabilities, such as the kink instability.<sup>20</sup> Another obstacle for a tokamak in terms of generating sustained power is the method by which current is driven in the machine. Current in tokamaks is usually provided by a central solenoid, often called an ohmic transformer. In this scheme, the plasma itself is used as the secondary leg of a transformer. The pulsed nature of this arrangement, though, is not conducive to steady-state operation. Further current drive is necessary, and the best source of this drive is an open question.<sup>21</sup>

### **2.2.2 Stellarator**

The initial design for the stellarator was laid out in 1958 by Lyman Spitzer<sup>22</sup> and is defined by generating the confining field completely by external coils. One of the chief reasons stellarators are desirable to plasma fusion efforts is the lack of a steady-state toroidal current. This fact bypasses many of the instabilities seen in tokamaks. Also, when a stellarator



encounters an instability, the ensuing disruption is relatively mild and does not typically lead to a loss of total confinement as is seen in the tokamak.

The stellarator design is not without drawbacks. Since only external fields are used to confine the plasma, the coils producing these fields must be irregularly shaped and the resulting magnetic fields are necessarily non-axisymmetric. The resulting coils must also be placed with great care and accuracy, resulting in much higher up-front expenses than in a typical tokamak. Due to a lack of plasma current, the stellarator also does not produce much heat natively. To bring the plasma to fusion relevant temperatures requires much more input power than in the tokamak design, again raising expenses.

### 2.2.3 Compact Toroidal Hybrid (CTH)

The Compact Toroidal Hybrid (CTH) is a stellarator-tokamak hybrid device located at Auburn university. The machine is configured so that it can run as a stellarator, with external coils providing the magnetic structure necessary for confinement of the plasma, or in more of a tokamak mode, with induced current in the plasma providing a substantial portion of the poloidal magnetic field. Designed to test the degree of external 3D magnetic field needed to mitigate current driven tokamak disruptions, CTH has shown promising results in confirming a vertical stability criterion<sup>23</sup> and exceeding the empirical Greenwald density limit.<sup>24</sup>

The vacuum vessel confining the plasma is a torus with major radius  $R \approx 0.75\text{m}$  and minor radius  $r \approx 0.3\text{m}$ . To begin a CTH shot, vacuum magnetic fields are activated. The plasma is then ionized and initially heated using ECRH, resulting in a plasma with  $T_e \approx 20\text{eV}$ . After this initialization, the ohmic transformer may be energized, inducing current in the plasma. Values of peak plasma parameters vary on a shot-to-shot basis, but typical values are  $T_{e\text{max}} \approx 200\text{eV}$ ,  $n_{e\text{max}} \approx 5 \times 10^{19}\text{m}^{-3}$ , and  $I_{p\text{max}} \approx 80\text{kA}$ .

CTH was designed to test the ability of externally supplied helical magnetic fields to suppress or mitigate current driven instabilities seen in tokamaks. To this end, the versatile

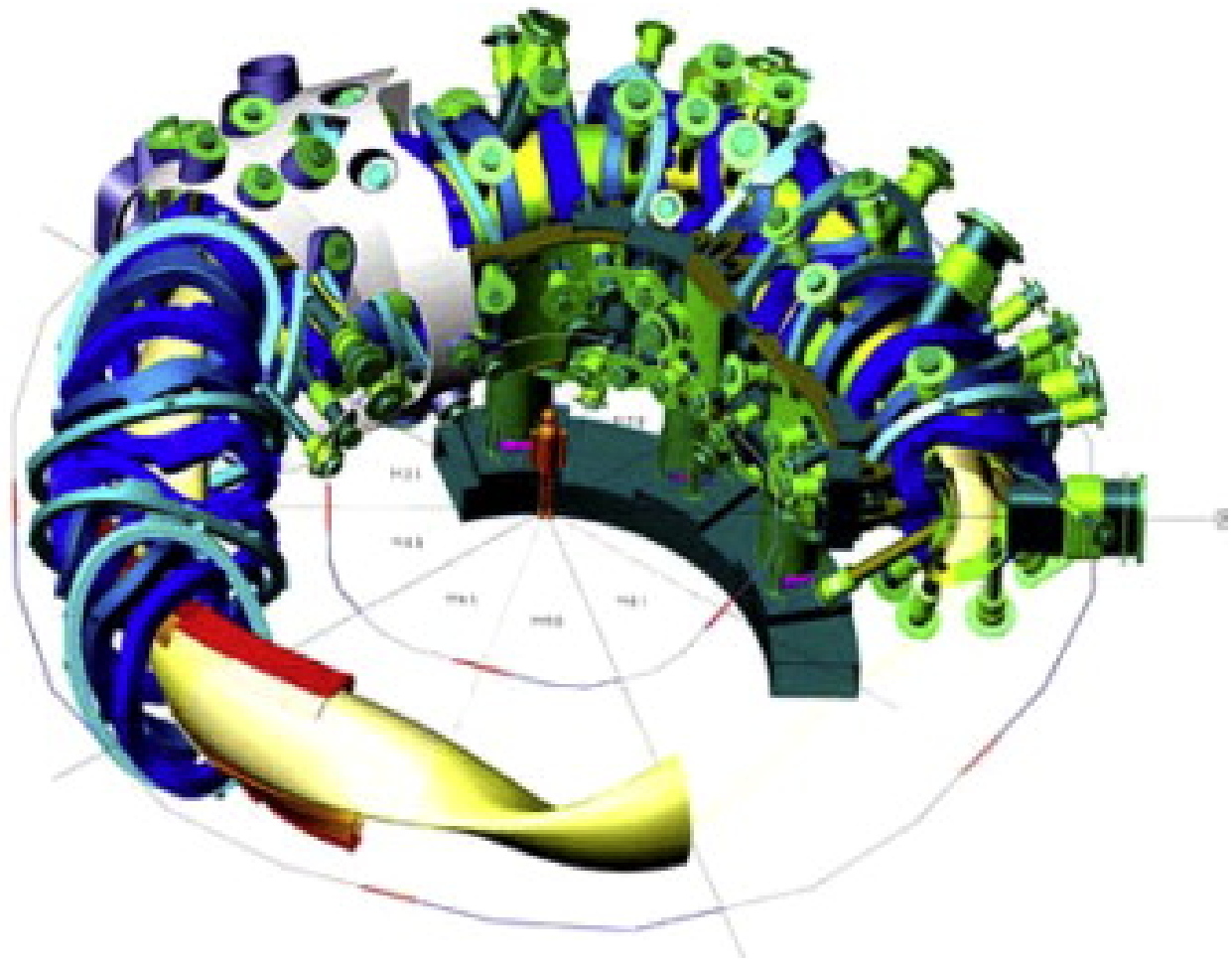


Figure 2.2: CAD model of the Wendelstein 7-X stellarator. Note the irregularity of the confining coils (dark blue) and the shaping of the resulting plasma (yellow). Reprinted from “Status of Wendelstein 7-X Construction,” by L. Wegener, 2009, *Fusion Engineering and Design*, Vol. 84, No 2-6, Pgs. 106-112. Copyright 2009 by Elsevier Limited. Reprinted with permission.

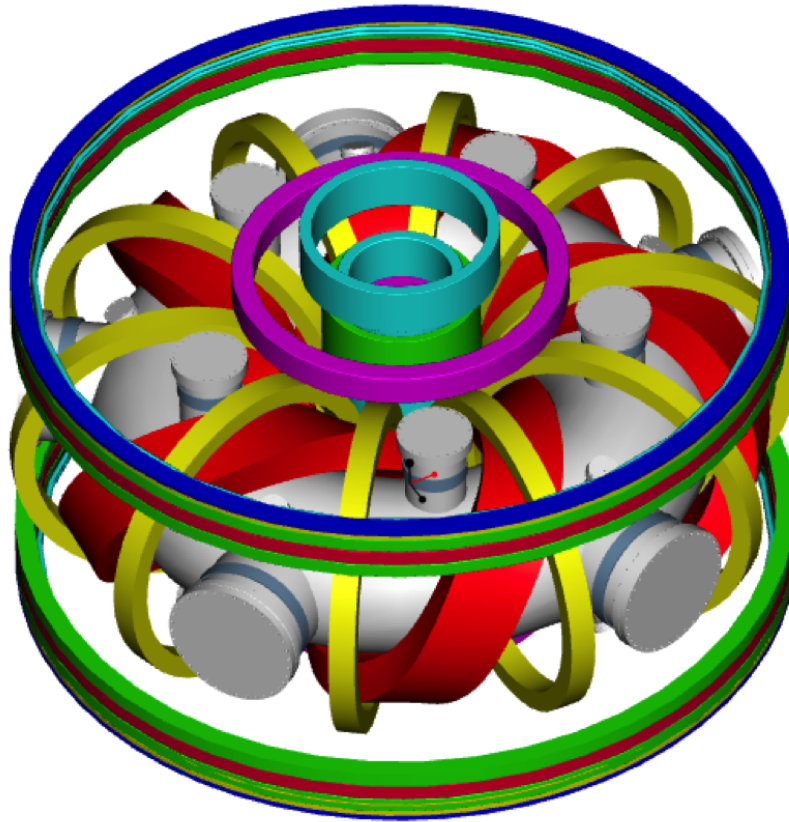


Figure 2.3: The Compact Toroidal Hybrid magnetic field coils. Red - Helical Field; Yellow - Toroidal Field; Green - Ohmic Transformer; Gray - Error Correction Coils; Blue - Vertical Field. The 3D shaping of the helical field coil results in a five-fold periodicity in CTH plasmas.

field shaping coils on the machine can achieve rotational transforms (the number times a field line rotates poloidally for every toroidal transit) in the range  $0.01 \leq \iota \leq 0.3$ . The confining fields in CTH possess a five-fold symmetry due to the geometry of the helical coil (red coil in figure 2.3).

The work in this paper is concerned with using NIMROD to model the start-up phase of a CTH plasma. In addition to these efforts, further computational work is also being done in regards to the CTH. V3FIT<sup>12</sup> is currently being used in concert with a suite of diagnostics to reconstruct evolving equilibrium states of the plasma during a discharge. Initial work has focussed on magnetic diagnostics, but a more varied collection of diagnostics are now being included in these reconstructions. In addition, equilibria calculated using V3FIT and VMEC<sup>11</sup> are now being imported into NIMROD with the purposes of exploring the effects of perturbations away from equilibrium and the formation of features not reproducible in VMEC, namely magnetic islands.

## 2.3 Modeling efforts

Computer modeling has been an important aspect of plasma research for many years. Much work has been done and many important steps have been made in plasma modeling in recent years, but a full review of the topic is beyond the scope of this dissertation. Since this work is concerned with using the fluid code NIMROD<sup>5</sup> to model the CTH, we will briefly discuss the NIMROD code (as well as offering a review of MHD as it applies to the code) and review previous steps in the modeling of the most similar device to the CTH, the stellarator, as well as provide context for this research.

### 2.3.1 The NIMROD code

The Non-Ideal Magnetohydrodynamic with Rotation, Open Discussion (NIMROD) code is, at its core, a 3D partial differential equation solver. This solver, and the auxiliary routines which surround it, have been specialized to solve MHD problems. NIMROD has a flexible

geometric representation of the computational domain, requiring two dimensions to be represented by a finite element mesh while the third is represented in Fourier space. The code is massively parallel and is being used to solve problems ranging from fundamental plasma physics to those applicable to fusion.<sup>7,8,9,10</sup>

## MHD Review

Magnetohydrodynamics is an important approximation in which single particle effects are ignored in favor of the collective effects of the plasma as a whole. This approximation is applicable to many magnetic confinement regimes and has been used to great effect in understanding phenomena in plasma discharges. There are many well written discourses on MHD<sup>20,21,25</sup>; this section will discuss only the representation of the MHD equations used in NIMROD.

NIMROD uses Maxwell's equations (without displacement current) and the single fluid form of velocity moments of the electron and ion distribution functions to calculate the dynamics of a discharge. Maxwell's equations, less Gauss's law and the displacement current, are given by

$$\nabla \times \vec{E} = -\frac{\partial \vec{B}}{\partial t}, \quad (2.2)$$

$$\nabla \times \vec{B} = \mu_0 \vec{J}, \quad (2.3)$$

$$\nabla \cdot \vec{B} = 0, \quad (2.4)$$

where  $\vec{E}$  is the electric field,  $\vec{B}$  is the magnetic field, and  $\vec{J}$  is the current density. If quasineutrality is assumed ( $Z_{\text{eff}} n_i \approx n_e$  where  $n_i$  is the ion density and  $n_e$  is the electron density), the continuity equation is given by

$$\frac{\partial n}{\partial t} + \vec{v} \cdot \nabla n = -n \nabla \cdot \vec{v}, \quad (2.5)$$

where  $\vec{v}$  is the center of mass velocity and  $n$  is the single fluid number density. The velocity evolution is given by

$$\rho \frac{\partial \vec{v}}{\partial t} + \rho \vec{v} \cdot \nabla \vec{v} = \vec{J} \times \vec{B} - \nabla p - \nabla \cdot \overset{\leftrightarrow}{\Pi}, \quad (2.6)$$

where  $\rho$  is the mass density,  $p = nT$  is the pressure, and  $\overset{\leftrightarrow}{\Pi}$  is the fluid stress tensor. Temperature evolution is given by

$$\frac{n}{\gamma - 1} \left( \frac{\partial}{\partial t} + \vec{v} \cdot \nabla \right) T = -p \nabla \cdot \vec{v} - \overset{\leftrightarrow}{\Pi} : \nabla \vec{v} - \nabla \cdot \vec{q} + Q, \quad (2.7)$$

where  $q$  is the thermal diffusion and  $Q$  is a catchall term for sources of heat. The equations are closed using a generalized Ohms law

$$\vec{E} = -\vec{v} \times \vec{B} + \eta \vec{J} + \frac{1}{ne} \vec{J} \times \vec{B} + \frac{m_e}{n_e^2} \left[ \frac{\partial \vec{J}}{\partial t} + \nabla \cdot (\vec{J} \vec{v} + \vec{v} \vec{J}) - \frac{e}{m_e} (\nabla p_e + \nabla \cdot \overset{\leftrightarrow}{\Pi}_e) \right], \quad (2.8)$$

where  $\eta$  is the resistivity. Note that this is the full set of equations that NIMROD solves. Each equation can be modified by omitting certain terms as defined by the user. For example, in all of this work, many of the terms in the generalized Ohm's law are dropped, leaving only

$$\vec{E} = -\vec{v} \times \vec{B} + \eta \vec{J}. \quad (2.9)$$

## 2.4 CTH/NIMROD model

For the purposes of modeling CTH, the NIMROD problem domain is represented by a 2D finite element mesh complemented by a Fourier spectrum in a third direction. The CTH vacuum vessel is approximated by a circular torus, which is used as the boundary for NIMROD simulations. A cross section of the torus is then divided by  $i_r$  and  $j_\theta$  radial and poloidal lines, respectively. These newly formed cells are the major mesh for the finite element analysis. Viewed in logical space, these cells form a rectangular mesh. This mesh

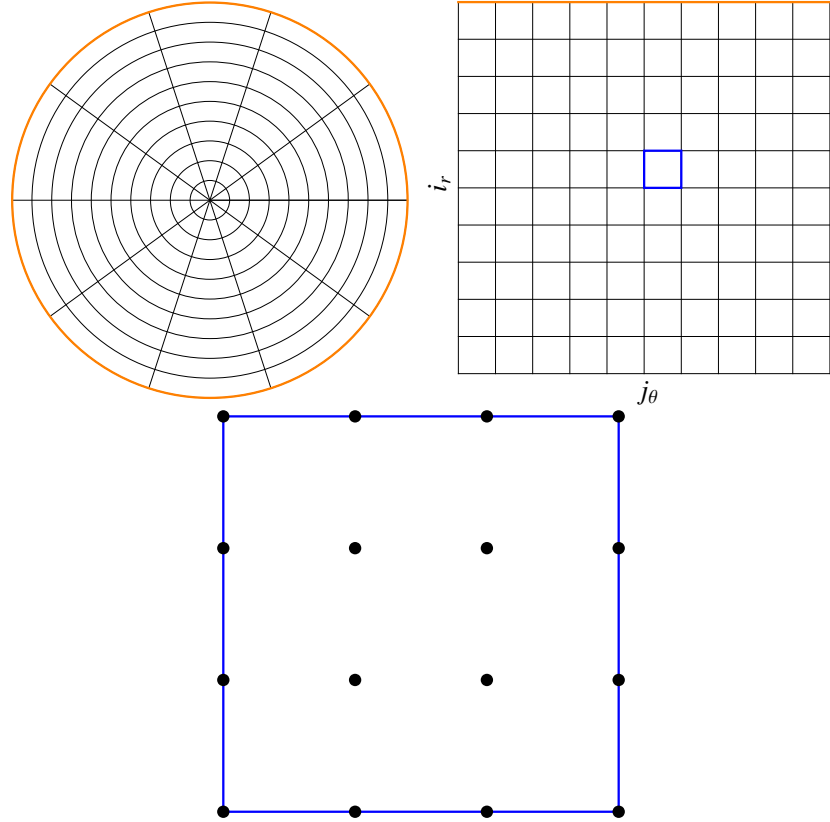


Figure 2.4: A circular cross section divided (upper left), transformed into logical space (upper right), and an individual cell with all quadrature points shown for  $N_p = 2$ .

is further refined with the addition of  $N_p$  data points on the vertical and horizontal legs of each cell, as well as  $2N_p$  points interior to the cell, where  $N_p + 1$  is the polynomial degree of the finite elements. For graphical representation, see figure 2.4. The toroidal nature of the problem is contained in the Fourier decomposition of the variables defined at each of the points described previously. Data between mesh points is calculated by interpolation. For more information on the specifics of the NIMROD mesh as applied to CTH, see appendix C.

## Chapter 3

### The Physics Model

The NIMROD code solves a very flexible system of equations geared toward the modeling of magnetohydrodynamic phenomena in plasmas. Aside from various geometric options, the verisimilitude of the physics involved in the model can be manipulated. Initial work done toward applying NIMROD to the CTH used a proof of principle model which included limited physics. The aim of this work is to enhance the physical fidelity of the model in order to perform single-fluid modeling of CTH in the most experimentally valid way possible. This chapter outlines the steps taken toward the goal of full physical fidelity in the model.

#### 3.1 Initial model

Work done by M. Schlutt et. al<sup>6</sup> laid out the foundation for this work. The CTH vacuum fields were modeled by manually loading the fields normal to the vacuum vessel into NIMROD and then using the magnetic field advance as a Laplace's equation solver for

$$\nabla \cdot \nabla \vec{B} = 0 \tag{3.1}$$

The resulting fields match well with a filamentary model of the physical coils on CTH as seen in figure 3.1. A constant loop voltage was then applied in vacuum. The resulting system of



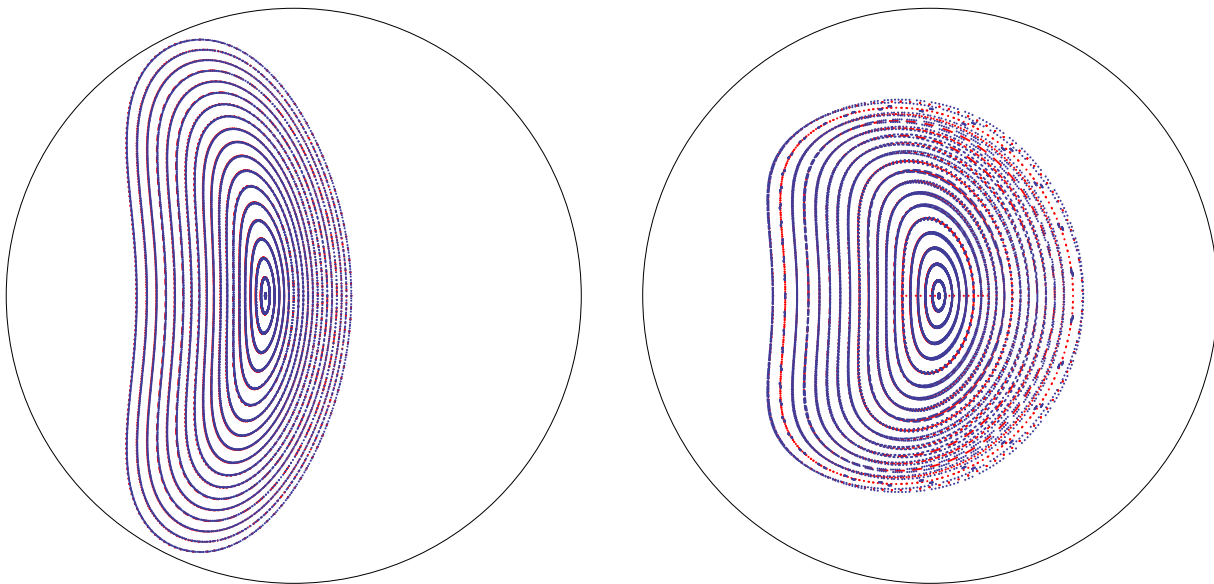


Figure 3.1: Comparison of NIMROD (blue) and CTH (red) vacuum flux surfaces at a full (left) and half (right) field period

equations governing the evolution of the plasma is

$$\rho \frac{\partial \vec{v}}{\partial t} + \rho(\vec{v} \cdot \nabla)\vec{v} = \vec{J} \times \vec{B} + \nabla \cdot \nu \rho \nabla \vec{v}, \quad (3.2)$$

$$\frac{\partial \vec{B}}{\partial t} = -\nabla \times \vec{E} + \kappa_{\text{div}B} \nabla \nabla \cdot \vec{B}, \quad (3.3)$$

$$\vec{E} = -\vec{v} \times \vec{B} + \eta \vec{J}, \quad (3.4)$$

$$\mu_0 \vec{J} = \nabla \times \vec{B}, \quad (3.5)$$

where the last term in equation 3.3 controls the  $\nabla \cdot \vec{B}$  cleaning in NIMROD's numerical scheme. Though there was no plasma present, a constant resistivity profile was set over most of the NIMROD domain to simulate a CTH plasma of  $T_e \sim 100\text{eV}$ . Near the edge of the domain a higher resistivity was set to suppress spurious current on open field lines. The applied loop voltage then drove a current in this vacuum "plasma", changing the structure of the background magnetic field. Depending on the strength of the driving loop voltage and the relative strength of magnetic diffusion (given through the dimensionless magnetic Prandtl

number  $P_{\text{rm}} = \nu/\eta$  where  $\nu$  is the kinematic viscosity and  $\eta$  is the magnetic diffusivity), magnetic islands were observed growing and, in some cases, breaking into regions of chaotic field lines.

### 3.2 Adding ohmic heating

Where initial experiments were done at  $\beta = 2\mu_0 p/B^2 = 0$ , recreating physical runs requires finite  $\beta$  and, thus, finite pressure. On CTH, the main source of heating during the discharge is ohmic heating, that is the heating of a resistive material when a current is passed through it. The power derived from ohmic heating is given by

$$Q = \eta J^2, \quad (3.6)$$

where  $J$  is the current density and  $\eta$  is the resistivity of the plasma. Including this heating term in the NIMROD model should generate heating wherever there is plasma current.

Recall that the initial model did not evolve the temperature. In order to use ohmic heating, then, it is necessary to add temperature evolution (in the form of equation 2.7) to the model. As a reminder,

$$\frac{n}{\gamma - 1} \left( \frac{\partial}{\partial t} + \vec{v} \cdot \nabla \right) T = -p \nabla \cdot \vec{v} - \overset{\leftrightarrow}{\Pi} : \nabla \vec{v} - \nabla \cdot \vec{q} + Q,$$

where  $n$  is the density,  $\gamma$  is the adiabatic index (taken to be 5/3),  $t$  is the time,  $\vec{v}$  is the velocity,  $T$  is the temperature,  $p = nT$  is the pressure,  $\overset{\leftrightarrow}{\Pi}$  is the viscous stress,  $\vec{q}$  is the heat diffusion, and  $Q$  is a catch-all term for the heating. In the limit of adiabatic heat conduction and  $\vec{v} = 0$ , the above becomes

$$\frac{n}{\gamma - 1} \frac{\partial T}{\partial t} = Q,$$

Using the form of ohmic heating defined in 3.6, the temperature evolution becomes

$$\frac{n}{\gamma - 1} \frac{\partial T}{\partial t} = \eta J^2,$$

On the simplest level, adding ohmic heating to the model should heat the plasma where there is current. Without complicating the initial model too much, it is possible to include ohmic heating with constant resistivity and adiabatic thermal transport. This should result in the deposition of heat where there is the most current, that is, on closed flux surfaces.

Figure 3.2 shows the results of adding ohmic heating to the basic model. Note that, as predicted, heat is deposited where current is flowing, and is deposited proportional to the amount of current. This is an important first step in bringing the model more in line with experiment, as now there is a mechanism for converting current to heat, evolving  $\beta$  and making it an important plasma parameter.

### 3.3 Adding temperature dependent thermal diffusivity

When a physical parameter can be calculated as a combination of NIMROD's basic plasma variables ( $T$ ,  $\vec{v}$ ,  $\vec{B}$ , and  $n$ ), the option exists to calculate said parameter at each time step. In the original model, all of these parameters were kept constant. With the addition of ohmic heating, it is possible to use the plasma temperature to alter them as they evolve in reality.

The first such parameter to be altered is the thermal diffusivity. Previously, for simplicity, the thermal diffusivity had been set to 0 (the previous adiabatic assumption). Physical plasmas, however, are not adiabatic, with the thermal diffusivity varying greatly parallel and perpendicular to the guide field in magnetized plasmas. From Goedbloed and Poedts,<sup>20</sup> following the formalism of Braginskii, the thermal conductivity (that is the thermal diffusivity

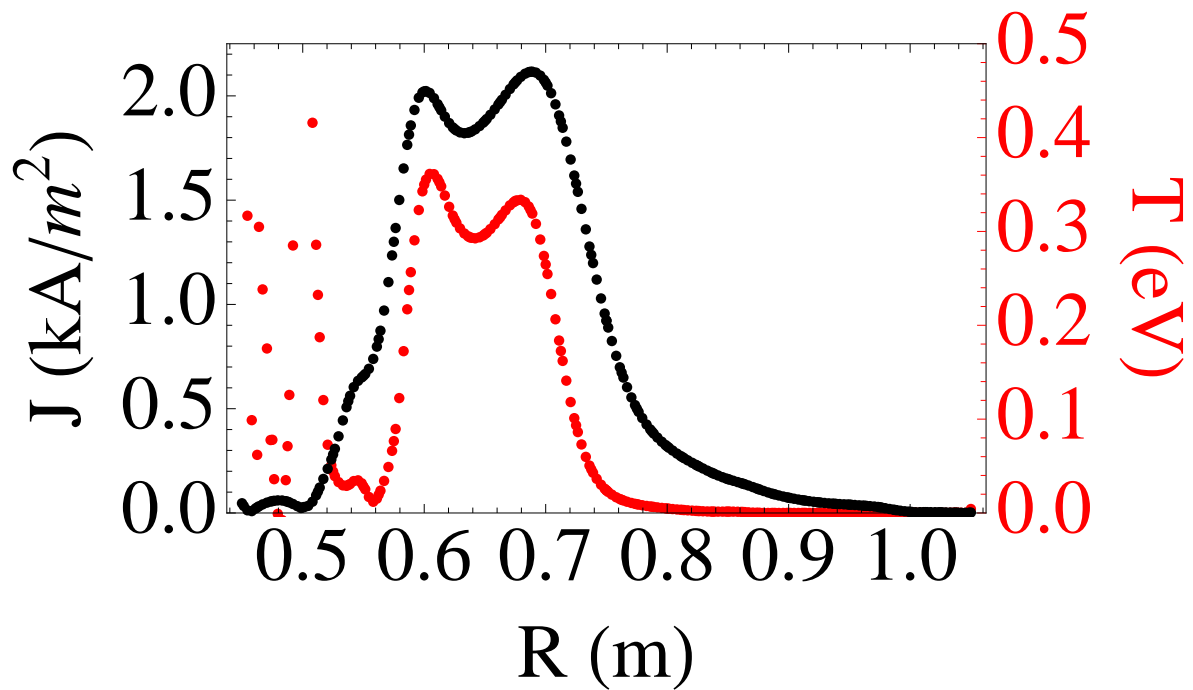


Figure 3.2: Current density (black) and temperature (red) at 1ms for a simulation with ohmic heating, a constant electrical diffusivity of  $630\text{m}^2/\text{s}$ , and a constant loop voltage of 1V. These values were chosen for illustrative purposes and do not reflect experimental conditions. Note the effect of ohmic heating: increasing temperature in regions where plasma current is driven. Also note the anomalous heating near  $r = 0.5\text{m}$ .

times the density) parallel and perpendicular to the magnetic field are given by

$$\kappa_{\parallel} = 4.4 \frac{nkT_e \tau_e}{m_e} \quad (3.7)$$

$$\kappa_{\perp} = 4.6 \frac{nkT_e}{m_e \omega_{ce}^2 \tau_e} \quad (3.8)$$

where  $\omega_{ce} = e|\vec{B}|/m_e$  is the electron cyclotron frequency and  $\tau_e$  is the electron relaxation time given as

$$\tau_e \equiv \frac{6\sqrt{2}\pi^{3/2}\epsilon_0^2\sqrt{m_e}(kT_e)^{3/2}}{\ln\Lambda e^4 n_e} \quad (3.9)$$

where  $\ln\Lambda$  is the Coulomb logarithm. Thus the thermal conductivities are given by

$$\kappa_{\parallel} = 26.4 \frac{\sqrt{2}\pi^{3/2}\epsilon_0^2(kT_e)^{5/2}}{\ln\Lambda e^4 \sqrt{m_e}} \quad (3.10)$$

$$\kappa_{\perp} = 0.77 \frac{e^3 \ln\lambda n^2}{\pi^{3/2}\epsilon^2 \sqrt{2}|B| \sqrt{m_e} (kT_e)^{3/2}} \quad (3.11)$$

Note that the electron thermal diffusivities are cited here as, though the calculations in this work are single fluid, the electron thermal diffusivities dominate.

In NIMROD, the thermal diffusivity is not directly calculated using the constants and equations cited above. Instead, in the mode used in this work, the parallel thermal diffusivity is scaled based on its temperature dependence. Thus, the model used in NIMROD is given by:

$$\kappa_{\parallel} = \text{Max} \left( \text{Min} \left( \kappa_0 \left( \frac{T_0}{T} \right)^{5/2}, \kappa_{\text{max}} \right), \kappa_{\text{min}} \right) \quad (3.12)$$

where  $\kappa_{\parallel}$  is the parallel thermal diffusivity,  $\kappa_0$  is the parallel thermal diffusivity calculated for a reference temperature  $T_0$ , and  $\kappa_{\text{max}}$  and  $\kappa_{\text{min}}$  are the maximum and minimum values  $\kappa_{\parallel}$  is allowed to take. The user provides  $\kappa_0$ ,  $T_0$ ,  $\kappa_{\text{max}}$ , and  $\kappa_{\text{min}}$ .

For the perpendicular thermal diffusivity, a constant value is used. This is due to the fact that, from equations 3.10 and 3.11,  $\kappa_{||} \sim T_e^{5/2}$  and  $\kappa_{\perp} \sim T_e^{-1/2}$ . Thus, considering only the temperature, the variation in  $\kappa_{\perp}$  is deemed to be small over the temperatures of interest. It is true that the perpendicular thermal diffusivity does have a density dependence as  $\kappa_{\perp} \sim n^2$ , and the ramifications of ignoring this dependence are discussed later.

Adding self consistent thermal diffusivity should allow the heat generated by ohmic heating to leave the generation site and propagate to colder portions of the plasma. Furthermore, if the boundary is held cold, the anisotropic nature of the model used for thermal diffusivity should facilitate a sharper delineation of plasma and vacuum regions in the model. In the plasma region, heat will tend to follow the closed field lines, staying in the closed flux region and only leaking into the open field line region on the much slower time scale determined by  $\kappa_{\perp}$ . Conversely, on the open field lines in the vacuum region, heat should freely flow to the boundary, leaving behind a cold region of open field lines.

As expected, and seen in figure 3.3, the inclusion of temperature dependent parallel thermal diffusivity makes clear in the temperature contours the extent of the plasma volume. The inclusion of this term greatly enhances the verisimilitude of the model and paves the way for future additions to the model by causing the temperature to behave more like it does experimentally, leading to a clear boundary between plasma and vacuum.

### 3.4 Adding initial temperature and density profiles

Before current is driven in a CTH experimental shot, klystrons are engaged, with the dual purpose of ionizing the background neutral gas and heating the resulting plasma through ECRH. Due to the localized nature of the heating, this process is difficult to model in NIMROD. The klystrons remain energized during the ohmic portion of a discharge, but the majority of heating at that point comes from ohmic heating. Though unable to directly reproduce the effects of the ECRH, by setting an initial temperature and density profile the state of the plasma at the onset of current drive can be modeled.

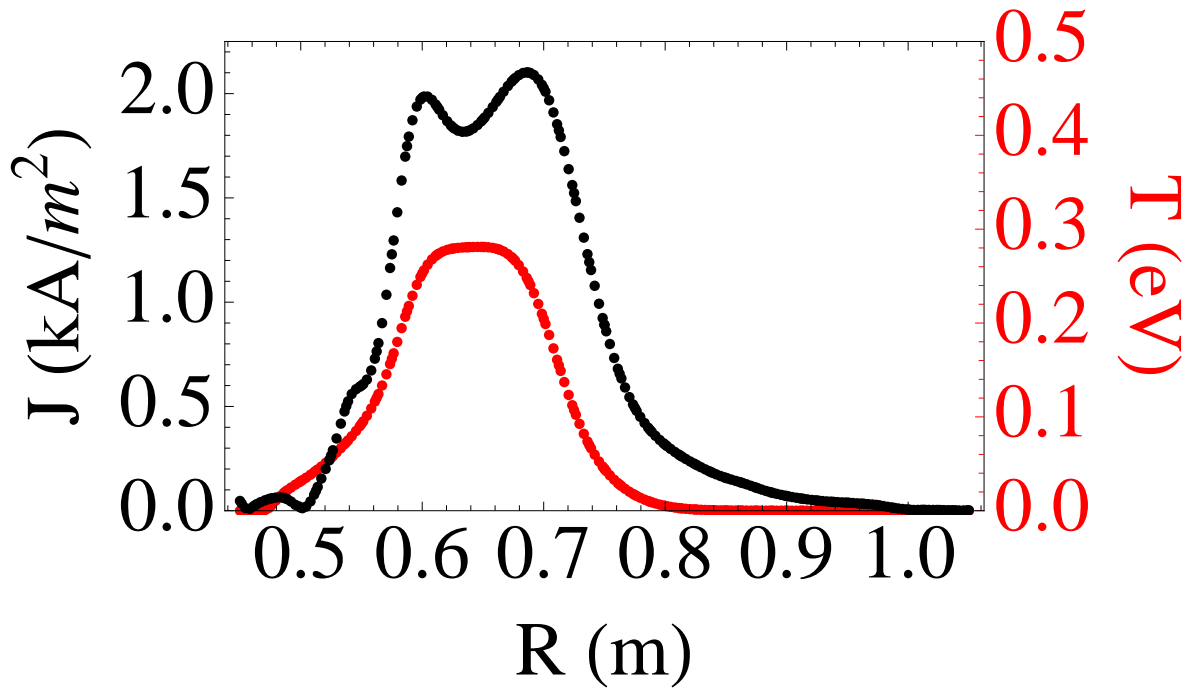


Figure 3.3: Current density (black) and temperature (red) at 1ms for a simulation with ohmic heating, a constant electrical diffusivity of  $630\text{m}^2/\text{s}$ , a constant loop voltage of 1V, and anisotropic heat conduction, with  $\kappa_{\parallel}/\kappa_{\perp} = 10^5$ . These values were chosen for illustrative purposes and do not reflect experimental conditions. The anomalous heating from figure 3.2 has been remedied by the parallel heat conduction. Note also the effect of the perpendicular heat conduction, smoothing the temperature to a peaked profile.

NIMROD does not differentiate between closed flux surfaces (where the plasma is) and open field lines (where there should be little plasma). Thus, there is no straightforward way to set profiles such that there is a clear plasma region and a clear “vacuum” region. Recall the temperature evolution equation (equation 2.7):

$$\frac{n_\alpha}{\gamma - 1} \left( \frac{\partial}{\partial t} + \vec{v}_\alpha \cdot \nabla \right) T_\alpha = -p_\alpha \nabla \cdot \vec{v}_\alpha - \overleftrightarrow{\Pi}_\alpha : \nabla \vec{v}_\alpha + n_\alpha \nabla \cdot \left( \overleftrightarrow{\chi}_\alpha \cdot \nabla T_\alpha \right) + Q_\alpha \quad (3.13)$$

In the case of  $\vec{v}_\alpha = 0, Q_\alpha = 0$ , the temperature evolution becomes:

$$\frac{n_\alpha}{\gamma - 1} \frac{\partial T_\alpha}{\partial t} = +n_\alpha \nabla \cdot \left( \overleftrightarrow{\chi}_\alpha \cdot \nabla T_\alpha \right) \quad (3.14)$$

Recall, also, that  $\overleftrightarrow{\chi}_\alpha$  contains the thermal conductivities parallel and perpendicular to the magnetic field. As seen before, these thermal conductivities are also parameters that can be manipulated in NIMROD. Therein lies the path to setting initial temperature profiles for CTH modeling in NIMROD. First, the magnetic field is prescribed as before. Then, the entire simulation domain is set to the desired maximum temperature except at the boundary, which is set near 0. Setting constant values for  $\kappa_{||}$  and  $\kappa_{\perp}$  such that  $\kappa_{||} \gg \kappa_{\perp}$ , the temperature evolution equation is advanced. This results in heat on open field lines flowing out to the perpetually cold boundary while heat on the closed field lines remains in that region. The density profile is then set as a multiple of the resultant temperature profile.

Note that this process constitutes a further pre-processing step for a “full” NIMROD run. The workflow is now:

1. Load magnetic field as prescribed by Schlutt et al.<sup>6</sup>
2. Load initial temperature and density profiles as described above
3. Apply loop voltage

The ability to model the initial temperature and density profiles is essential to our modeling and understanding of the system as a whole. As previously described, the experiment



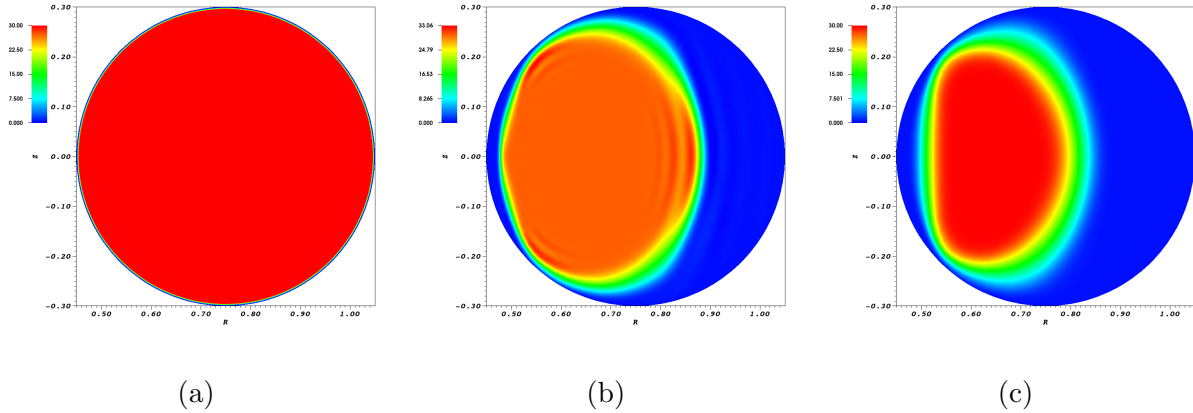


Figure 3.4: Evolution of temperature when setting an initial temperature profile. This simulation only evolves the temperature, with no plasma current being driven. (a) The desired maximum temperature is set over the domain except the wall, which is kept cold. (b) The temperature evolves with anisotropic thermal diffusivity. Heat on open field lines flows to the cold boundary, heat on closed field lines stays in plasma volume. (c) Final state used as initial conditions in model.

begins with an initial plasma with a finite density and temperature. Without the ability to set an initial temperature and density profile in the model, simulations would begin in a state dissimilar from the experiment. Furthermore, as will be discussed in the next chapter, an initial temperature and density are essential for setting plasma parameters such as resistivity to realistic values.

### 3.5 Adding temperature dependent resistivity

As was done with the perpendicular thermal diffusivity, other derived plasma parameters can be self-consistently calculated. An especially important physical parameter for the evolution of the plasma is the resistivity. From Spitzer,<sup>26</sup> we have the following approximation for the resistivity:

$$\eta_{\parallel} \approx \frac{m_e}{2e^2 n_e \tau_e} \quad (3.15)$$

Where  $m_e$  is the mass of the electron,  $e$  is the charge of the electron,  $n_e$  is the electron density, and  $\tau_e$  is the collisional relaxation time for the plasma. Using the definition of  $\tau_e$  from equation 3.9 in equation 3.15, the temperature dependence of the plasma resistivity can be seen:

$$\eta_{\parallel} \approx \frac{e^2 \ln \Lambda \sqrt{m_e}}{12 \sqrt{2} \pi^{3/2} \epsilon_0^2 (k T_e)^{3/2}} \quad (3.16)$$

Since the parallel and perpendicular resistivities in the Spitzer model only differ by a factor of 2, NIMROD uses one overall value of the resistivity. Since resistivity is inversely proportional to the temperature, adding this term to the model should result in lowered resistivity in the heated region. This, in turn, should drive more current in these regions.

In the NIMROD model, the temperature dependent nature of the resistivity is represented as

$$\eta = \text{Max} \left( \text{Min} \left( \eta_0 \left( \frac{T}{T_0} \right)^{-3/2}, \eta_{\text{max}} \right), \eta_{\text{min}} \right), \quad (3.17)$$

where  $\eta_0$  is a reference resistivity calculated for a temperature of  $T_0$  and  $\eta_{\text{max}}$  and  $\eta_{\text{min}}$  are the maximum and minimum values, respectively,  $\eta$  is allowed to take.  $\eta_0$ ,  $T_0$ ,  $\eta_{\text{max}}$  and  $\eta_{\text{min}}$  are all set at runtime in the code, and can thus be easily manipulated during a run.

The inclusion of temperature dependent resistivity is important to the model in that it allows for realistic resistivity profiles. In the original model, resistivity was set as constant across the domain except near the edges, where it was artificially raised. That artificial raising of the resistivity is no longer needed as, in conjunction with the temperature dependent thermal conductivity, temperature dependent resistivity enforces a resistive layer in the vacuum region. The temperature dependent thermal conductivity ensures that the vacuum region remains cold, while the temperature dependent resistivity preferentially drives current in the hotter portions of the plasma.

### 3.6 Adding time dependent loop voltage

The ohmic transformer in CTH is pulsed during the course of an experimental shot to drive current in the plasma. This rapid change in the current driven in the solenoid produces a similarly rapid change in the magnetic flux through the center of CTH. The central solenoid can be considered the primary winding of a transformer, with the changing magnetic flux ( $\Phi$ ) through the primary winding inducing an electric field according to Faraday's law

$$-\frac{d\Phi}{dt} = \oint \vec{E} \cdot d\vec{l}, \quad (3.18)$$

in the secondary winding. In the case of CTH, the secondary winding is the plasma. This electric field drives current in the plasma.

Previously, a constant loop voltage had been used. To more accurately model CTH plasmas, a time dependent model was adopted in which the experimental loop voltages were averaged (there are four separate measurements) and the result imported into NIMROD. These measurements by their nature include the plasma response to the applied electric field when a plasma is present. To obtain the unperturbed loop voltage for a plasma shot, an identical shot was taken in the absence of a plasma. For a comparison of the perturbed and unperturbed loop voltage, see figure 3.5. These unperturbed loop voltages are used in this work.

As the loop voltage is the major drive of current in the model, having a model for the time behavior of the loop voltage is important to modeling the current rise in the plasma. While linear loop voltages are sufficient later in the shot and for proof of principle runs, to fully model the dynamics of the current rise requires a non-linear model of the loop voltage to match the rapidly changing conditions in that portion of the discharge.

For more information on the initialization of the NIMROD model for CTH using the items mentioned in this chapter, see appendix C.

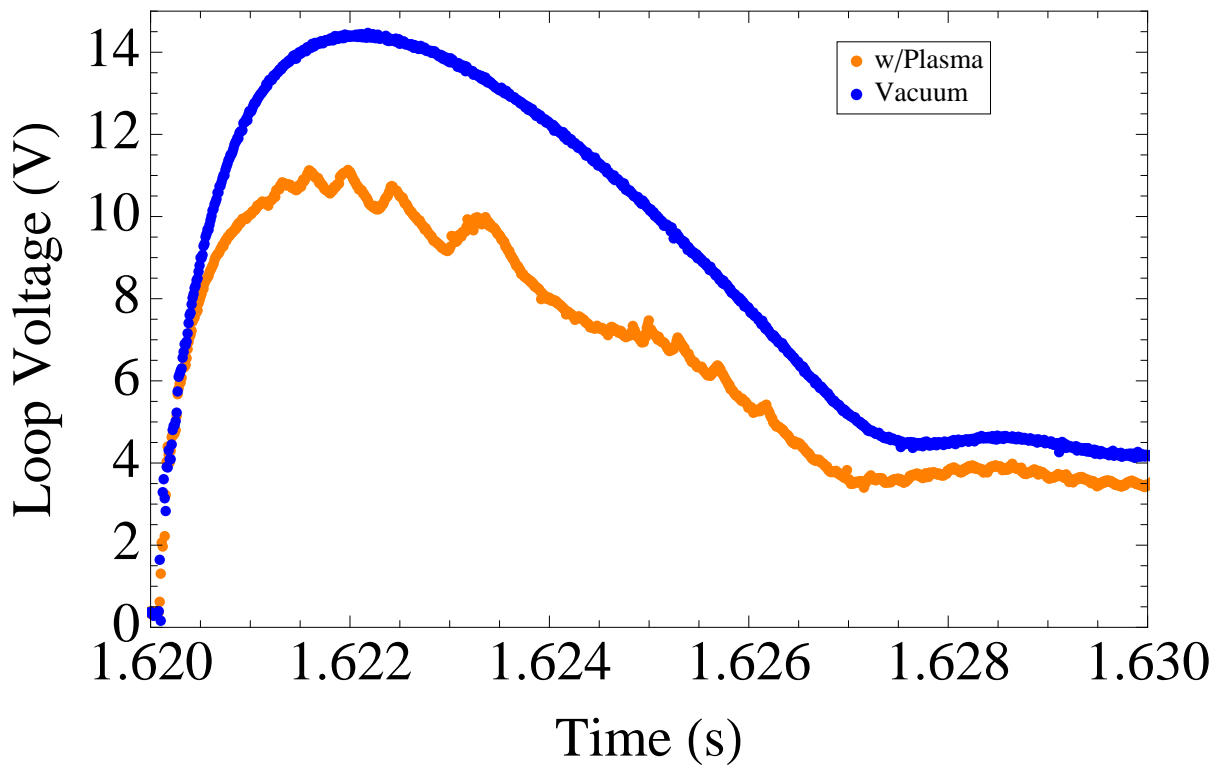


Figure 3.5: Comparison of perturbed (orange) and unperturbed (blue) loop voltage. Note the lower amplitude of and wiggles in the perturbed loop voltage. The diagnostic which measures the loop voltage also captures the response of the plasma to the ohmic drive.

## Chapter 4

### Comparison of Full Model To Experiment

#### 4.1 Model of shot 13030823

##### 4.1.1 Introduction and shot overview

Discharges in the CTH begin with a background magnetic field provided by coils external to the vacuum vessel. The plasma is then both initially ionized and heated with the input of microwaves from a klystron used for ECRH. If a driven plasma current is desired, charged capacitor banks are discharged through the central solenoid, inducing current in the plasma. Diagnostics on the machine are then able to measure various aspects of the discharge, such as Rogowski coils which measure the total current driven in the plasma and a three-chord interferometer which measures the line-averaged density across three chords in a vertically symmetric cross-section.

The evolution of the CTH plasma varies based on a number of variables such as the rotational transform of the background magnetic fields, the strength of the current drive, and the duration and magnitude of neutral gas fueling from the edge of the plasma. A feature seen during the initial current rise in many shots is a momentary hesitation in the current. Using V3FIT to reconstruct the plasma equilibrium when these hesitations occur, the rotational transform is seen to be near a low order rational value near the edge of the plasma. Also, the signal from an array of magnetic pickup coils sensitive to changes in the poloidal magnetic field fluctuates during these times, indicating an increase of magnetic activity. Both of these pieces of evidence suggest that some MHD process is inhibiting current flow in the plasma.

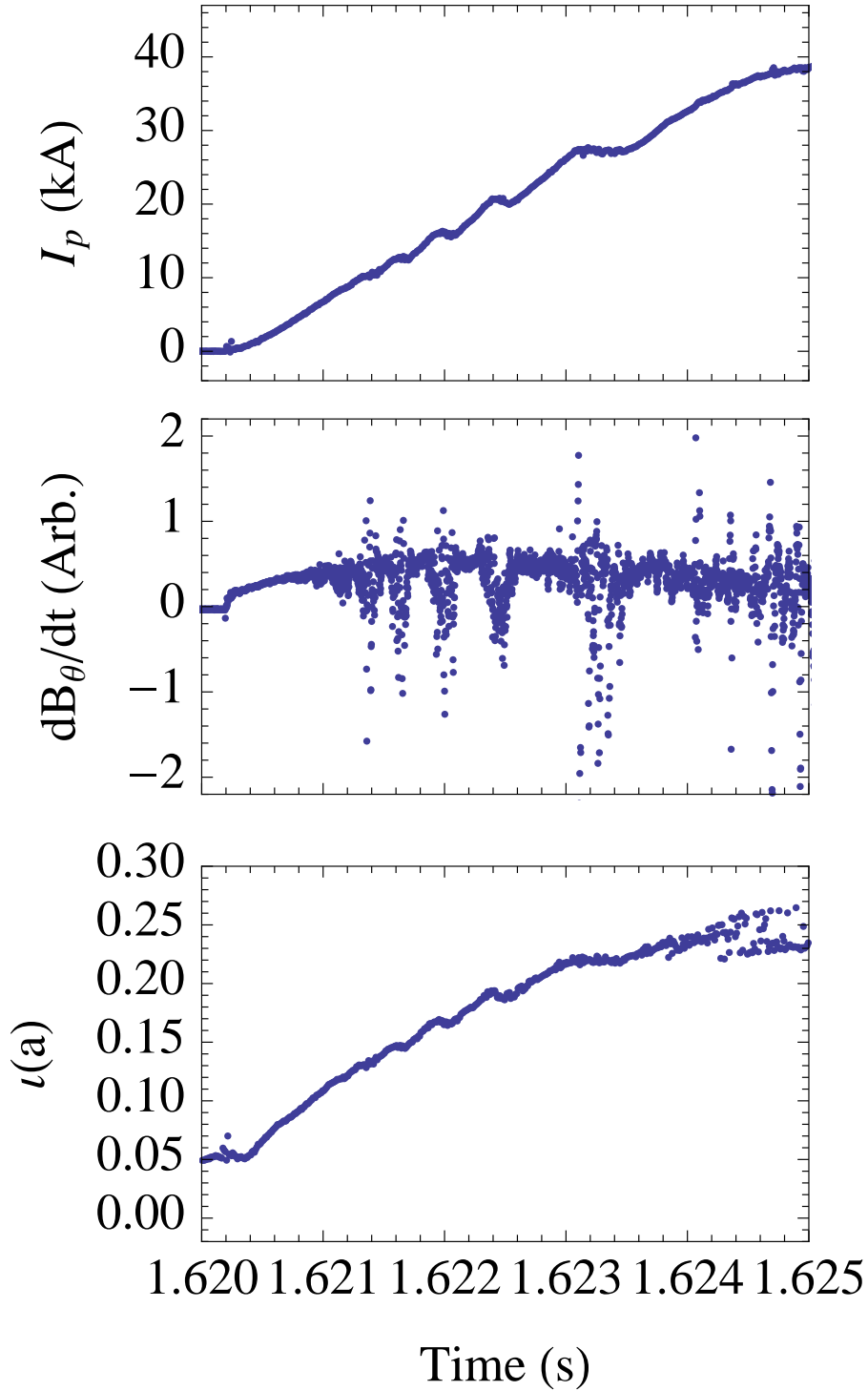


Figure 4.1: Overview of CTH shot 13030823 showing measured plasma current (top), measured  $dB_\theta/dt$  (middle), and V3FIT calculated edge rotational transform (bottom). The hesitations in plasma current are reflected in the  $dB_\theta/dt$  signal as fluctuations. During current hesitations, V3FIT calculates the rotational transform at the edge of the plasma to be near a low-order rational value.

### 4.1.2 Goals of run

Shot 13030823 was chosen for its pronounced current hesitations early in the current rise as is seen in figure 4.1. If the activity in the plasma which is causing the hesitations in the current is MHD-based, NIMROD should be able to accurately model it. While islands were observed in the initial modeling of Schlutt, no hesitations in current were observed. With an improved, self consistent model, however, we can further investigate the dynamics of this critical phase of the plasma. Thus, the goals of this run are:

1. Calibrate improved NIMROD model for investigations of CTH shots
2. Use NIMROD to look for current hesitations in the current rise phase
3. Identify possible causes for current hesitations

### 4.1.3 Model specifics

#### Equations solved

As referenced in Chapter 3, the model used in this work is greatly enhanced from the model used by Schlutt. The full set of equations solved in this model run is given by:

$$\mu_0 \vec{J} = \nabla \times \vec{B}, \quad (4.1)$$

$$\frac{\partial \vec{B}}{\partial t} = -\nabla \times \vec{E} + \kappa_{\text{div B}} \nabla \nabla \cdot \vec{B}, \quad (4.2)$$

$$\rho \frac{\partial \vec{v}}{\partial t} + \rho \vec{v} \cdot \nabla \vec{v} = \vec{J} \times \vec{B} - \nabla p + \nu \rho \nabla^2 \vec{v}, \quad (4.3)$$

$$\frac{\partial n}{\partial t} + \vec{v} \cdot \nabla n = -n \nabla \cdot \vec{v}, \quad (4.4)$$

$$\frac{n}{\gamma - 1} \left( \frac{\partial}{\partial t} + \vec{v} \cdot \nabla \right) T = -p \nabla \cdot \vec{v} - \overset{\leftrightarrow}{\Pi} : \nabla \vec{v} - \nabla \cdot \vec{q} + \eta J^2, \quad (4.5)$$

$$\vec{E} = -\vec{v} \times \vec{B} + \eta \vec{J}. \quad (4.6)$$

## Initial conditions

In NIMROD, since the resistivity is calculated based on plasma parameters, the density and the temperature work in concert to affect the rate at which current is driven in the plasma. As the goal of this work is to investigate hesitations in the current rise thought to be caused by magnetic islands, it is important to accurately represent this current rise in the model. Thus, the choice of initial density and temperature profiles is crucial to accurately modeling this initial phase of the plasma.

In attempting to model the onset of ohmic current in NIMROD, a logical choice for the peak initial density is that density which returns a synthetic diagnostic signal closest to experiment. The line-averaged electron density for shot 13030823 measured by the interferometer is shown in figure 4.2. For a line-averaged density of  $8 \times 10^{17} \text{m}^{-3}$ , this yields a maximum density of  $\sim 10^{18} \text{m}^{-3}$ . It is found that no matter the initial temperature used for this density the resistivity is low enough that the ohmic current drive is faster in the model than in experiment. Moderately raising the density does not bring the modeled ohmic current drive in line with that which is seen in experiment, see figure 4.3. This disparity between experiment and model suggests that there is some mechanism by which the resistivity of the plasma is being increased that is not captured in the model. To match the rate of current rise early in time, a peak density of  $n_e \approx 10^{19} \text{m}^{-3}$  was used, with the shape of the density profile set as a multiple of the temperature profile used.

On CTH, there are no diagnostics which measure the temperature profile during an ohmic shot. In the absence of this knowledge, the profile shown in figure 3.4c is used. Once an initial density was chosen, the initial maximum temperature was altered until the initial current rise in the plasma closely matched that seen in experiment (see figure 4.4). An initial maximum temperature of 30eV was chosen through this process. Though a maximum temperature of 25eV produced a closer match in plasma current over the window shown, a maximum temperature of 30eV was a better match for longer.



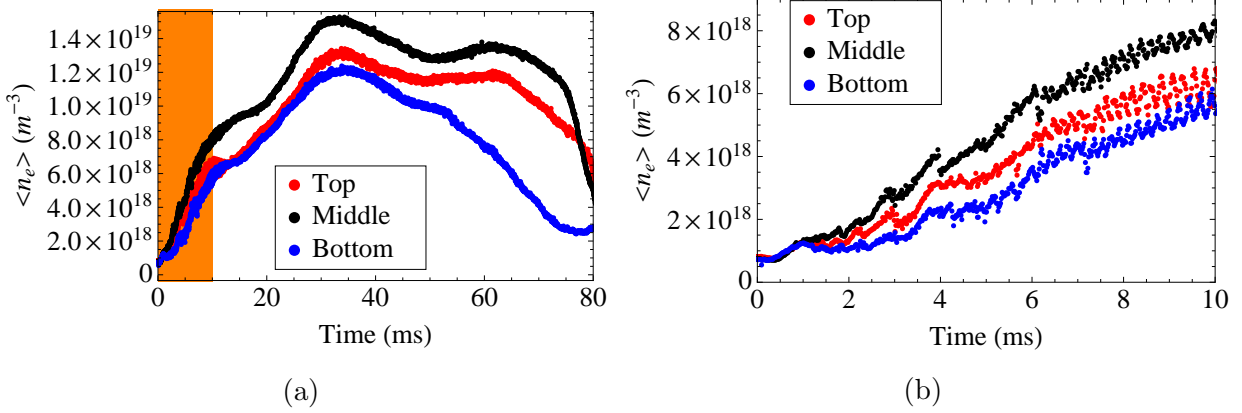


Figure 4.2: Measured line-averaged electron density from an interferometer for a chord at the mid-plane (black) and equidistant above (red) and below (blue) the mid-plane for the full shot (a) and the current ramp phase (b).

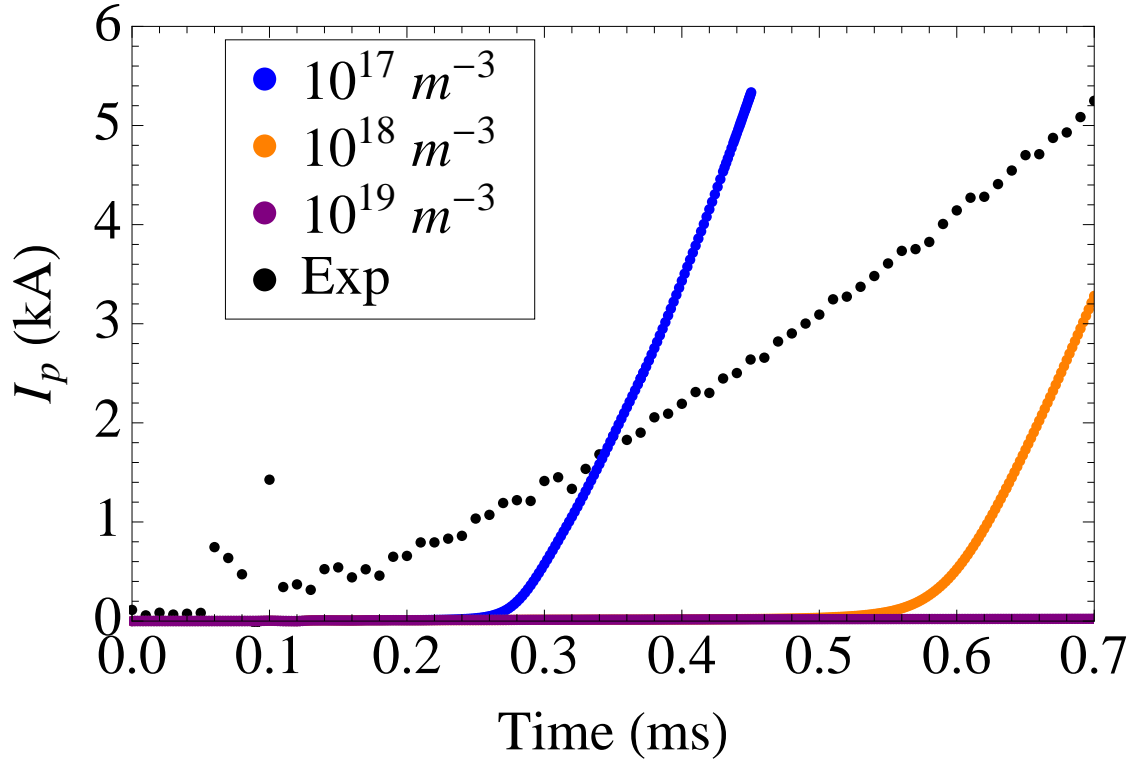


Figure 4.3: Effect of varying background densities on the rate of ohmic current drive at  $T = 0$  eV to drive as little plasma current as possible. At  $n = 10^{17} m^{-3}$  (blue) and  $n = 10^{18} m^{-3}$  (orange) the modeled plasma current overtakes experiment (black) while for  $n = 10^{19} m^{-3}$  (purple) it does not.

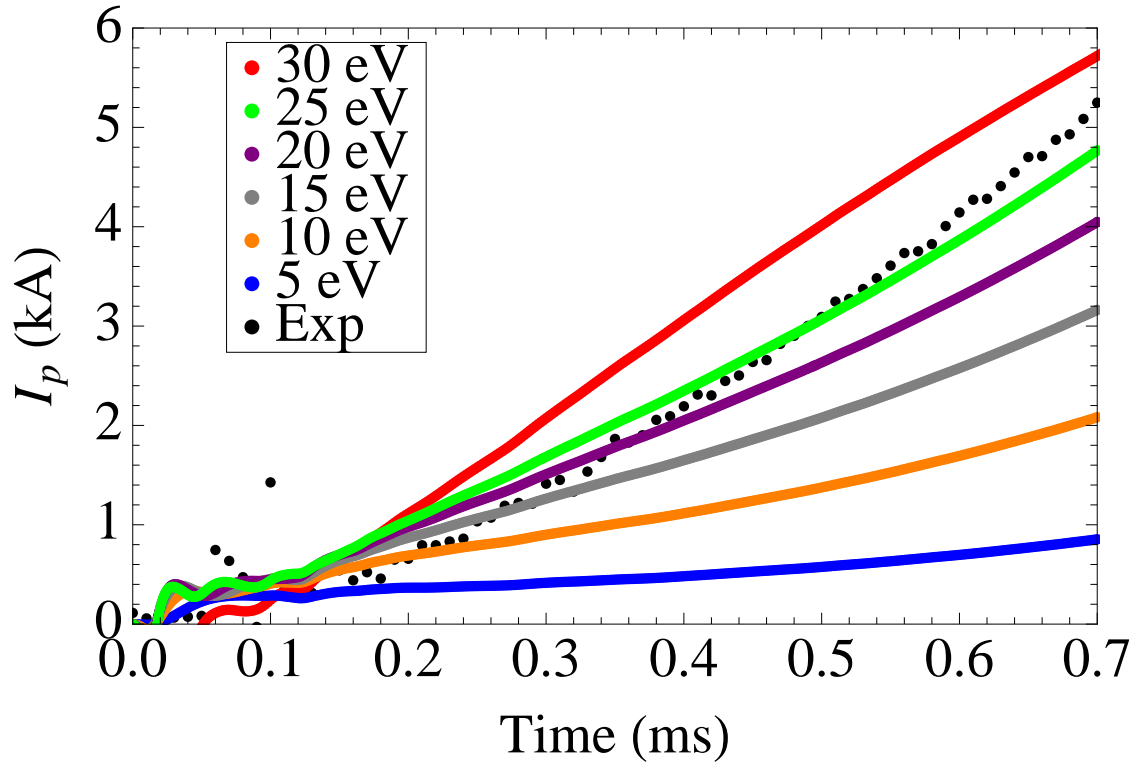


Figure 4.4: Plasma current comparison between experiment (black) and NIMROD with initial peak temperature of 30 eV (red), 25 eV (green), 20 eV (purple), 15 eV (gray), 10 eV (orange) and 5 eV (blue). 30 eV was chosen over 25 eV as the initial temperature for the modeling in section 4.1.4 due to the favorable comparison with experimental values later in time.

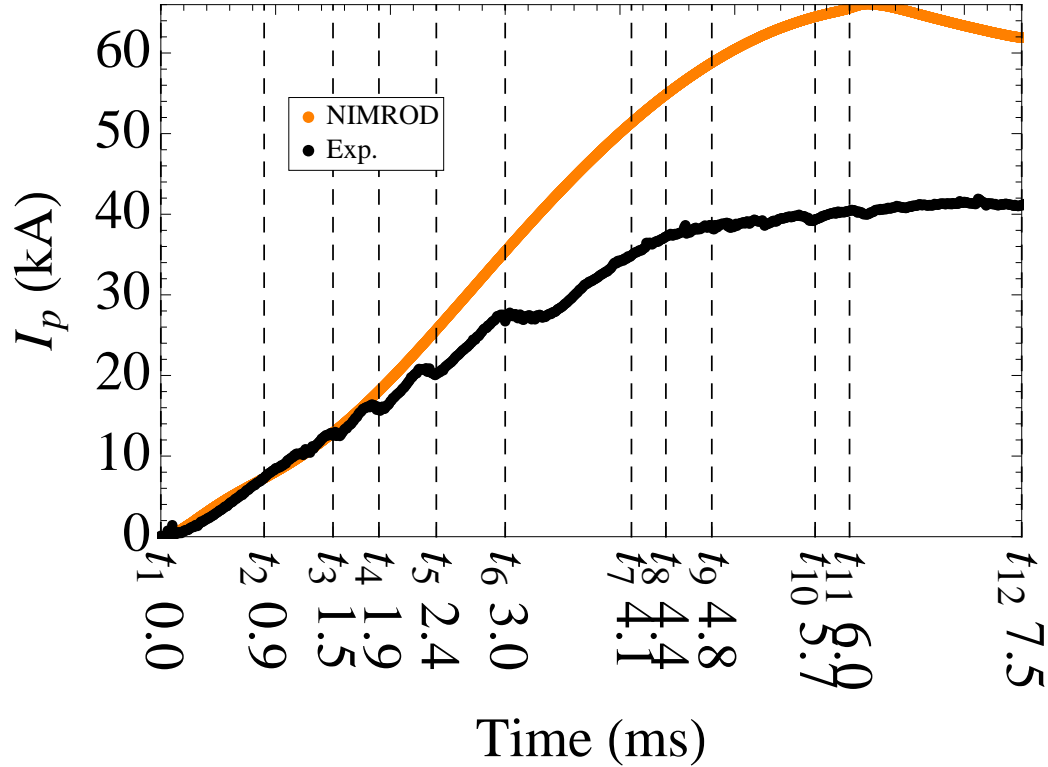


Figure 4.5: Comparison of plasma current from experiment (black) with NIMROD model (orange). The plasma current matches well early in time, but as hesitations are missed in the model, the currents begin to diverge. Vertical lines represent times shown in later time sequence figures.

As mentioned in Chapter 3, NIMROD can self consistently calculate the resistivity and parallel thermal diffusivity of the plasma. Values for these coefficients were calculated for  $T = 30\text{eV}$ .

#### 4.1.4 Presentation of results

Figure 4.5 shows the evolution of the total plasma current as modeled with NIMROD compared to the plasma current as measured in experiment. The first thing to note is the good agreement between experiment and model early in time. At the first few moments of current drive this is expected, as the temperature and density were chosen so that the initial current rise in the model would match experiment. It is promising to note that the agreement extends until the beginning of the current hesitations seen in experiment

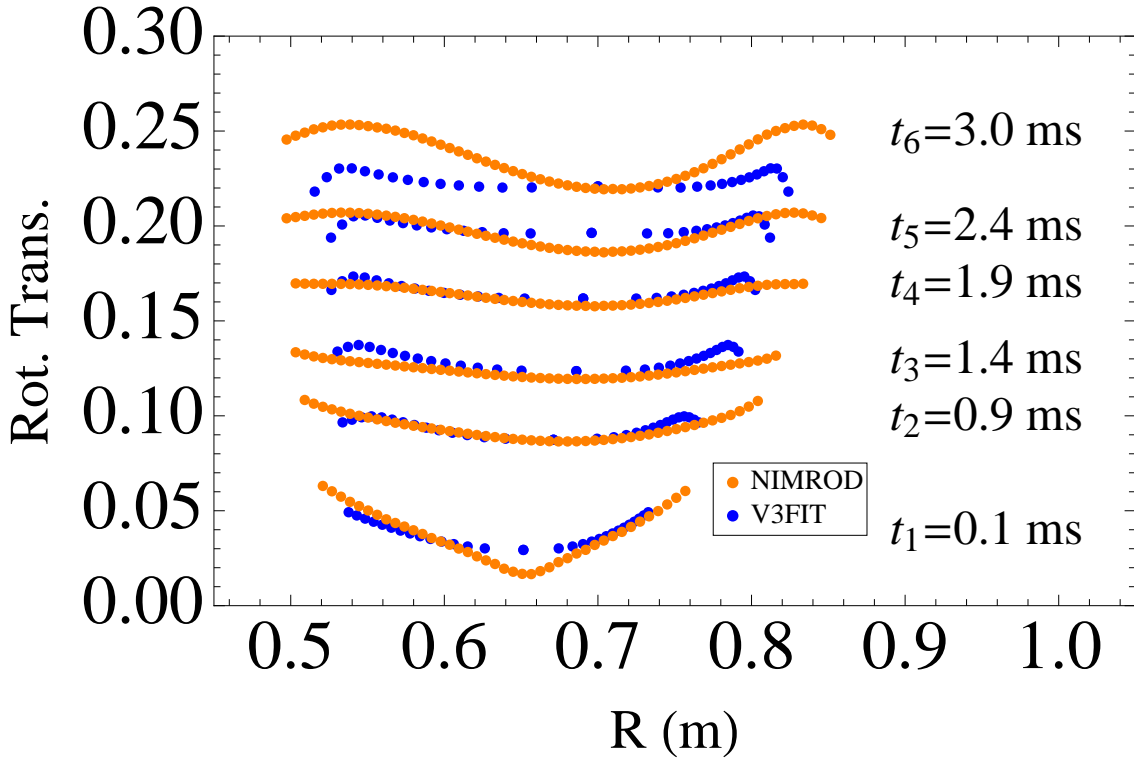


Figure 4.6: Comparison of rotational transform as calculated by V3FIT (blue) and NIMROD (orange) early in the current ramp. Though the NIMROD model misses the current hesitations seen in experiment and reflected in V3FIT, the rotational transform matches well between NIMROD and V3FIT. Note the greater extent of the NIMROD profiles as well as the downward turn near the edge of the V3FIT profiles. These are thought to be caused by the absence of physical limiters in the NIMROD model.

Using V3FIT, it is possible to obtain profiles of the rotational transform for this shot. Similarly, NIMROD has functionality which allows for the calculation of rotational transform (see appendix B). These two measurements are compared in figure 4.6, and show good agreement early in time when the plasma current in the model and experiment match well.

The current hesitations observed in the experimental current drive are not reproduced in the model. It is expected that these hesitations are due to large islands growing at rational surfaces near the edge of the plasma. In the model, however, no island growth is seen during the early stage of the ohmic current drive. Figure 4.7 illustrates this point, showing surface of section plots at times corresponding to current hesitations in experiment. The data in the figure is generated by first choosing a point in space and following the magnetic field from that point. When the field returns to the toroidal plane in which the initial point was chosen, the location of the crossing is recorded. This process is repeated hundreds of times and for various starting locations to produce a surface of section plot.

Furthermore, as is illustrated in figure 4.6, the rotational transform near the center of the plasma calculated by V3FIT continues to match well with the rotational transform calculated from NIMROD, despite the lack of current hesitations in the model. Both V3FIT and NIMROD show the  $\iota = 1/6$  and  $\iota = 1/5$  surfaces at nearly the same location in the plasma at  $t_4 = 1.9\text{ms}$  and  $t_5 = 2.4\text{ms}$ , respectively. Though the presence of these surfaces in the plasma does not cause hesitations in the model, the good agreement of the rotational transform profiles near the center of the plasma further suggests that the initial conditions chosen for the model are acceptable for this shot.

The V3FIT calculated rotational transform has a dip near the edge of the plasma. This sharp feature is not reproduced in the NIMROD model. It is thought that this discrepancy is caused by differences in boundary conditions in the two models. While the NIMROD domain is limited by the vacuum vessel, blocks are installed in CTH which physically limit the extent of the plasma. These physical limiters are included in the V3FIT model, leading

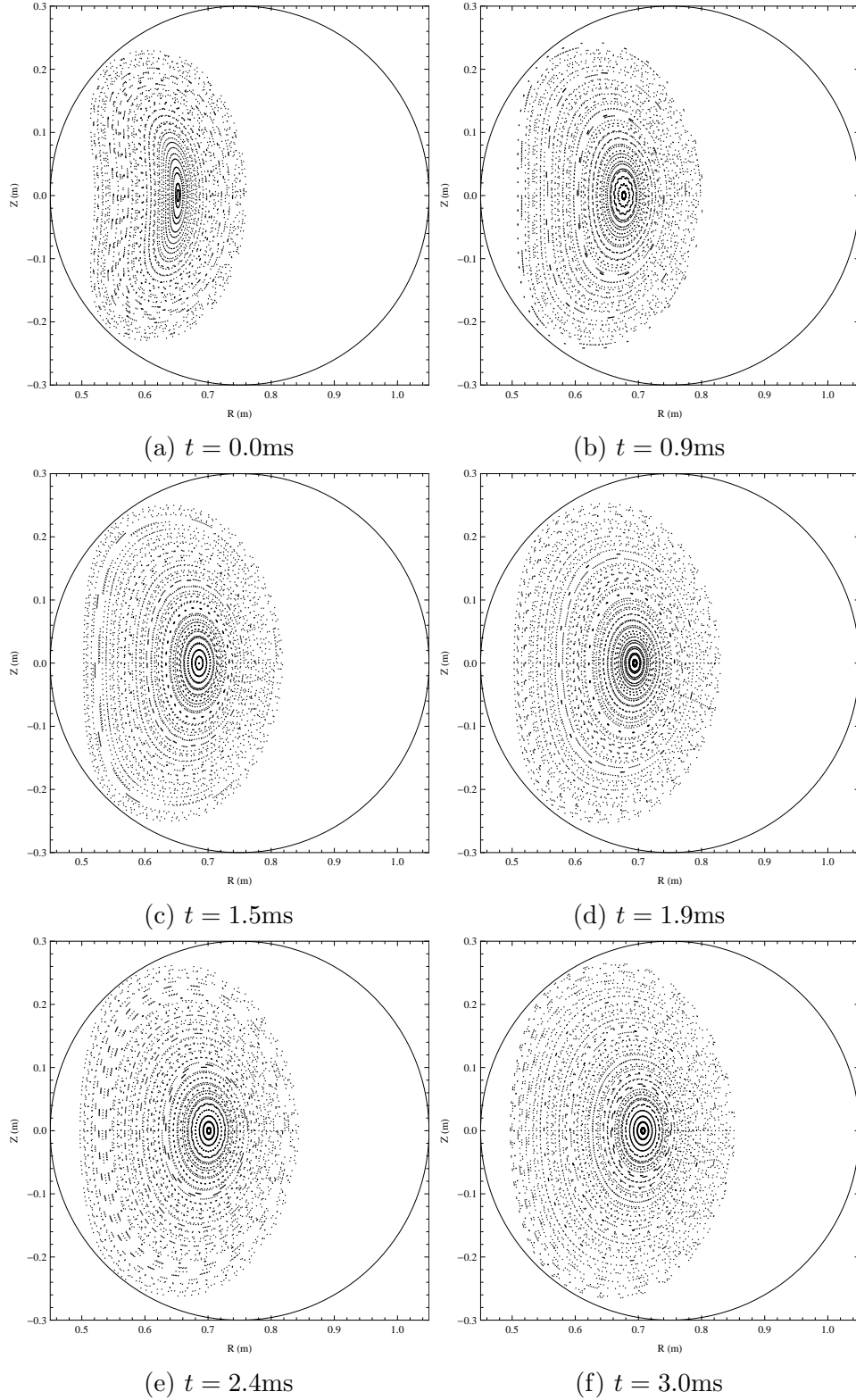


Figure 4.7: Time sequence of surface of section plots early in the current ramp at  $\phi = 0$ . Though many rational values of  $\iota$  are being traversed, so magnetic islands grow in the plasma volume.

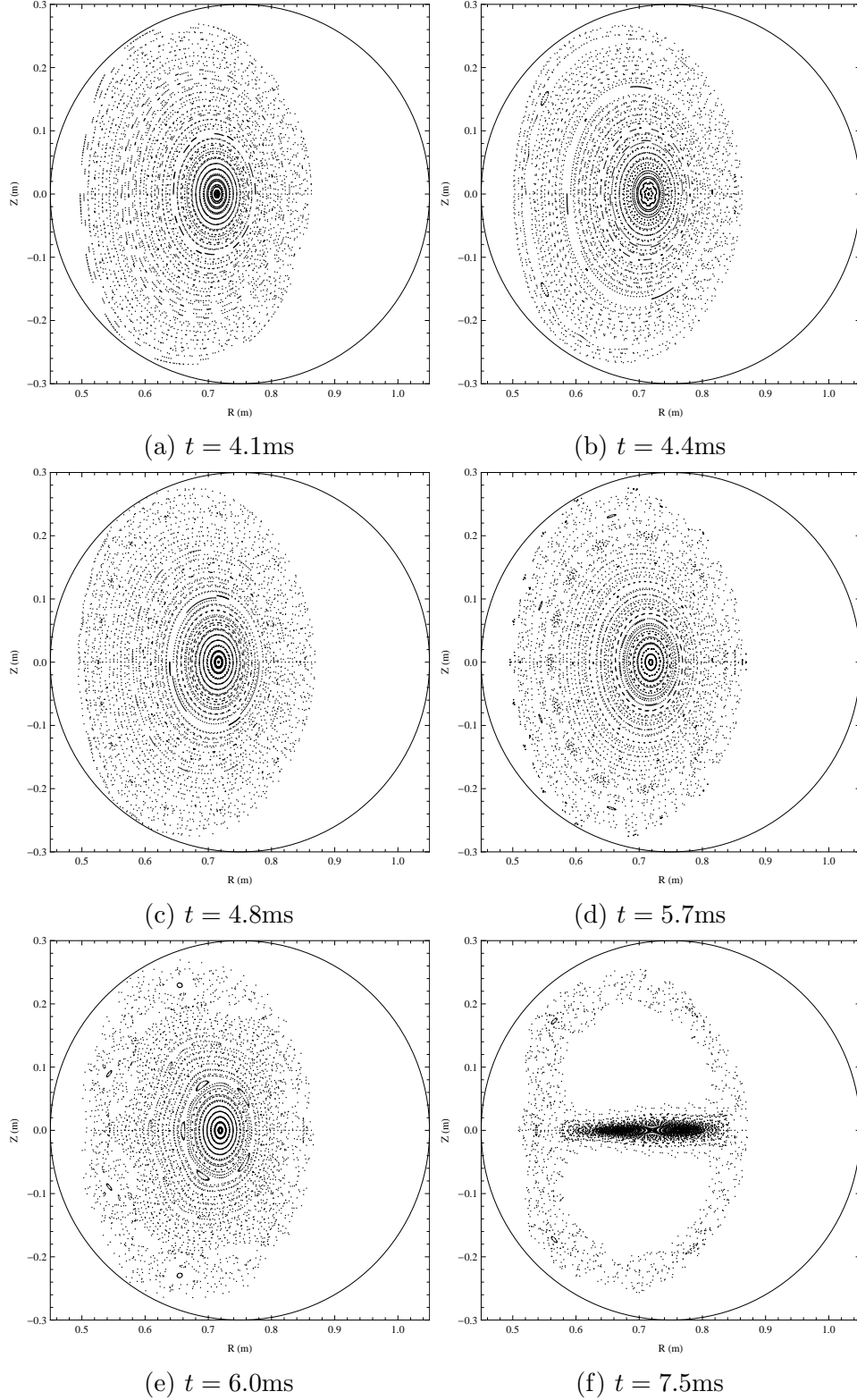


Figure 4.8: Time sequence of surface of section plots late in the current ramp at  $\phi = 0$ . A symmetry-preserving  $m = 15, n = 5$  island chain grows in the plasma, as seen in (b). The growth of this chain begins more island growth, with an  $m = 5, n = 2$  and an  $m = 12, n = 5$  chain growing in (d) and (e). An  $m = 2, n = 1$  island grows near the magnetic axis in (f).

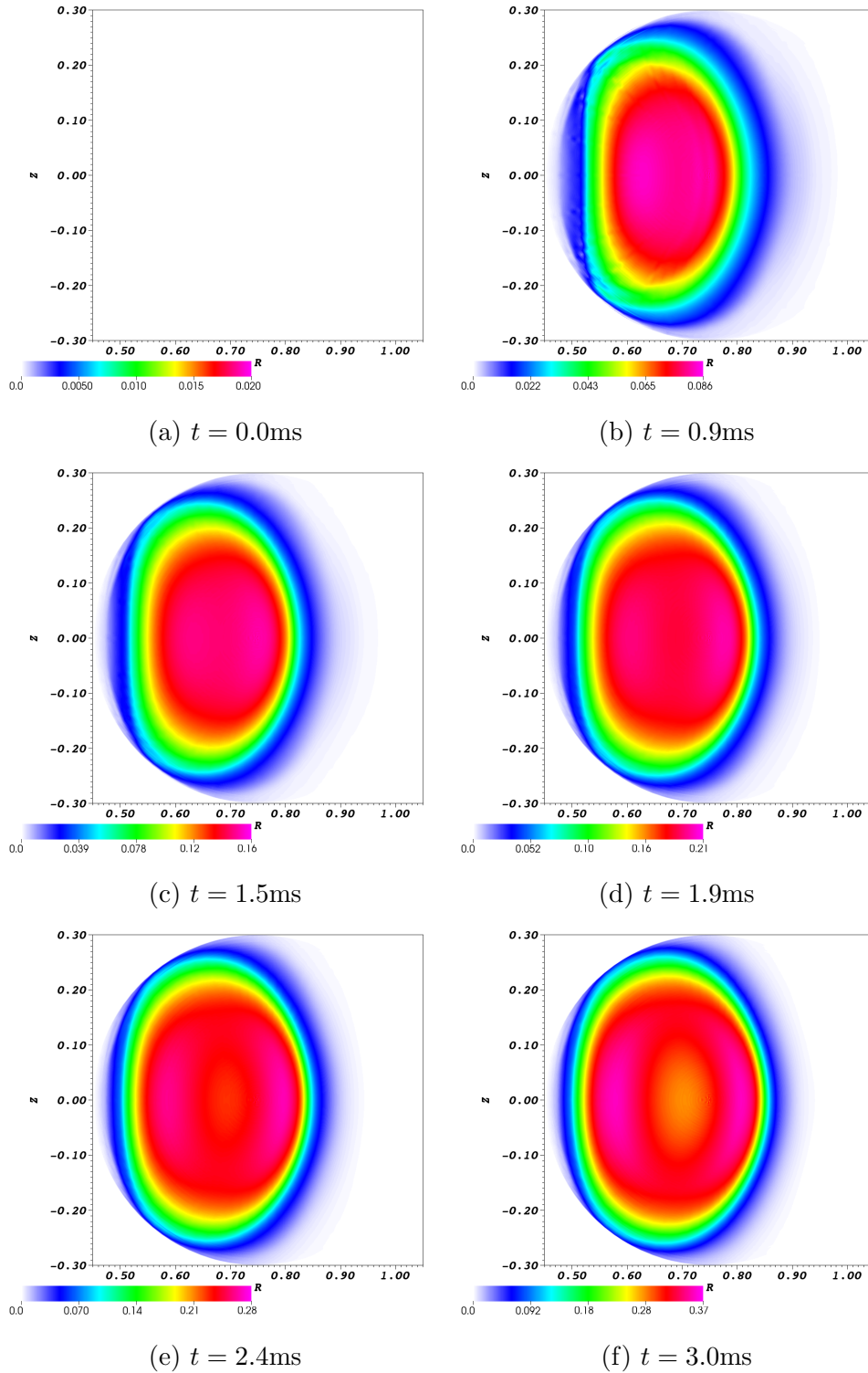


Figure 4.9: Time sequence of parallel plasma current density ( $\lambda = \mu_0 \mathbf{J} \cdot \mathbf{B} / B^2$ ) early in the current ramp at  $\phi = 0$ . The current forms a hollow profile.



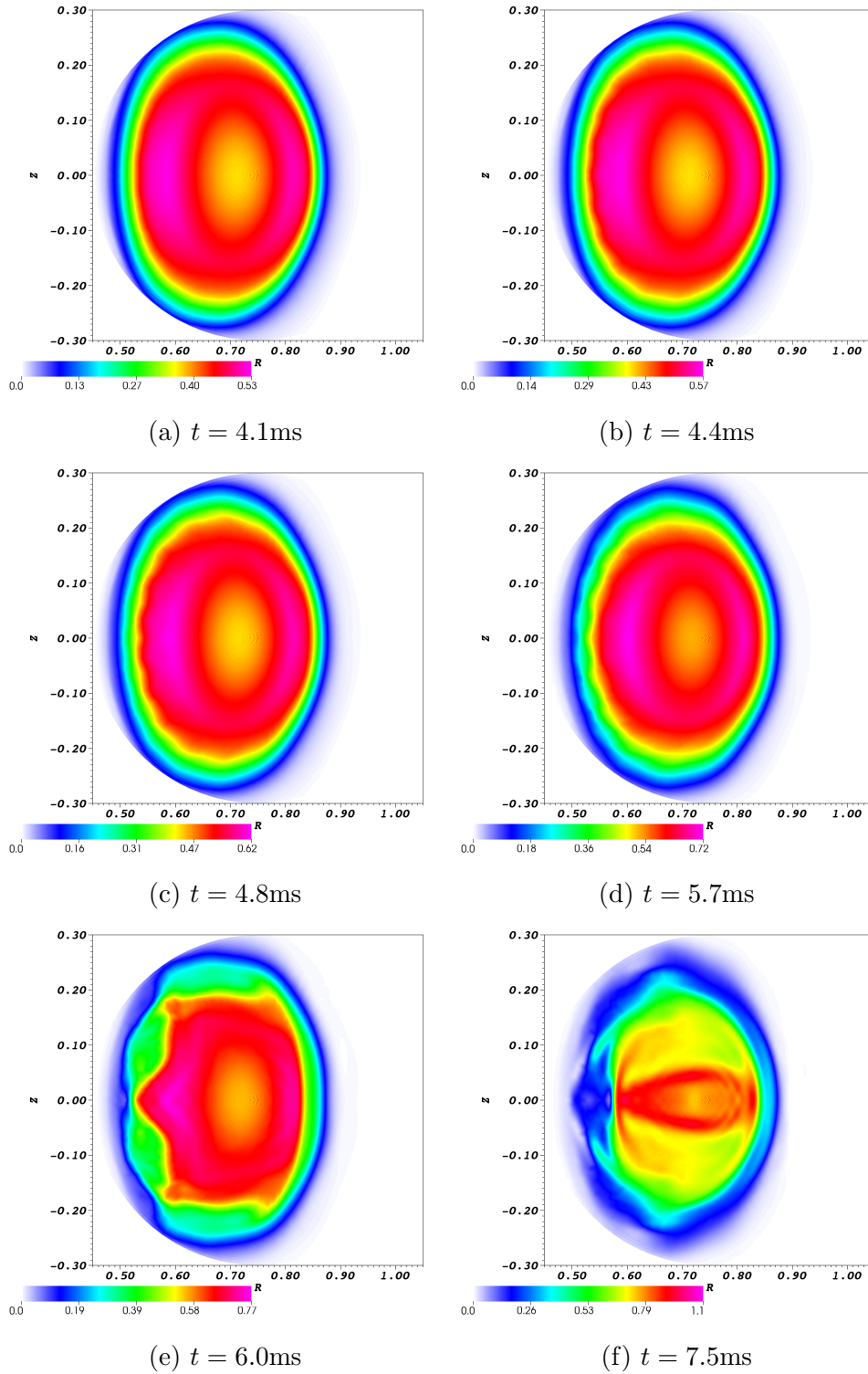


Figure 4.10: Time sequence of parallel plasma current density ( $\lambda = \mu_0 \mathbf{J} \cdot \mathbf{B} / B^2$ ) late in the current ramp at  $\phi = 0$ . As islands grow in the plasma, they have a noticeable effect on the plasma current density profiles. When islands are small and symmetry-preserving, the edge of the current density profile becomes wavy, as is seen in (a)-(d). As the islands, grow, so does their effect on the plasma current, as seen in (e) and (f).

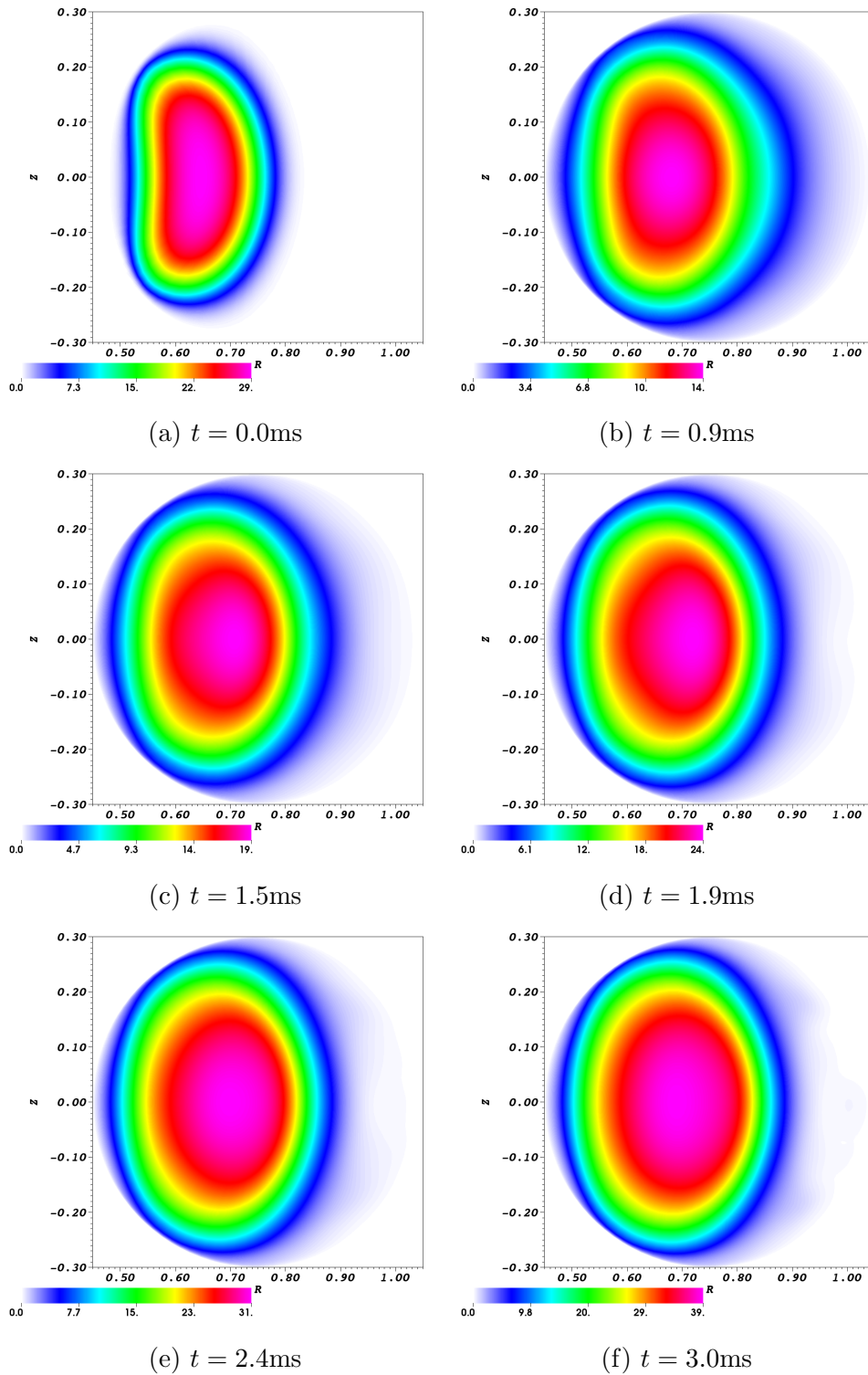


Figure 4.11: Time sequence of temperature early in the current ramp at  $\phi = 0$ . The perpendicular thermal diffusivity and initial temperature profile create a peaked temperature profile from the hollow current density profiles of figure 4.9.

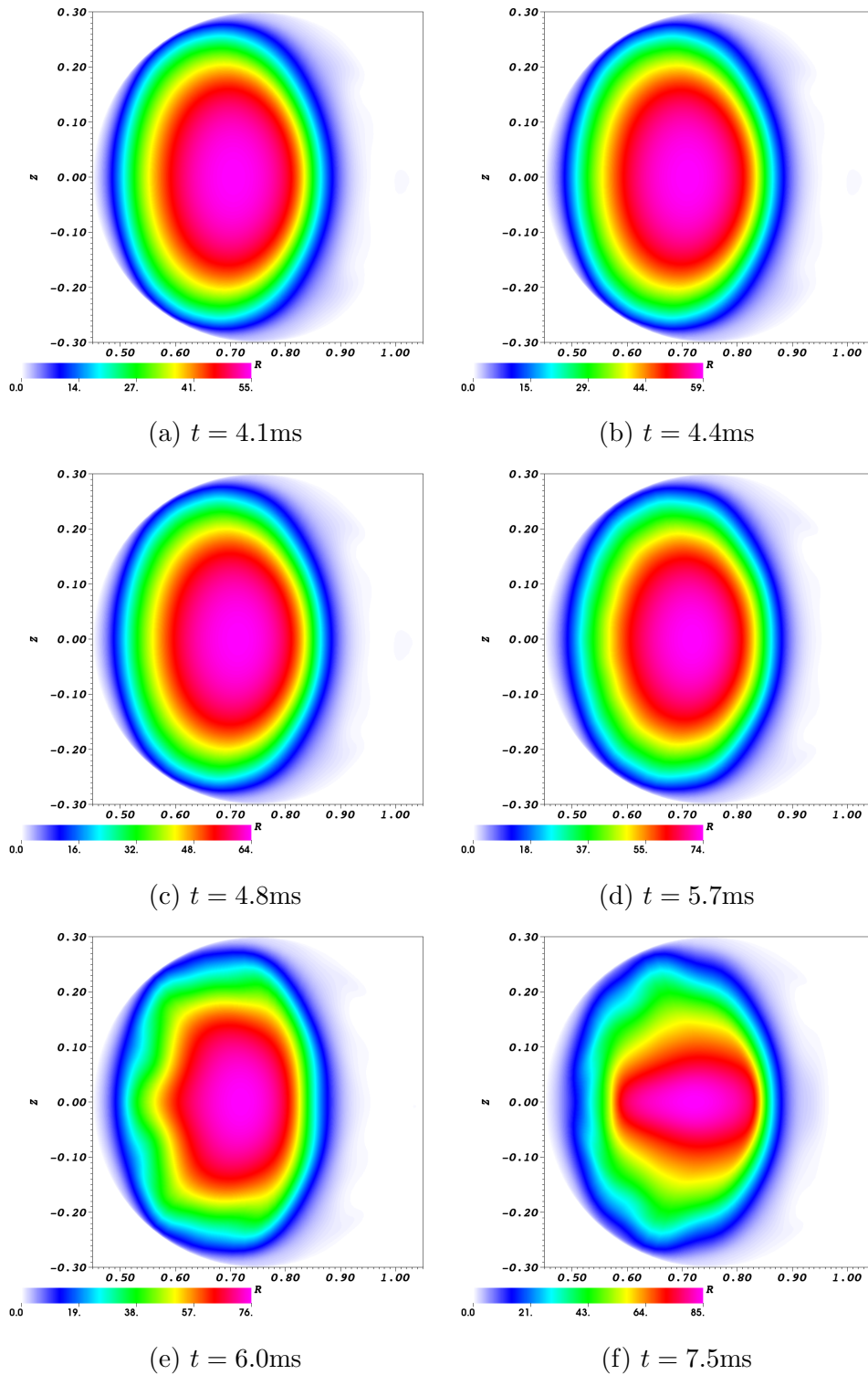


Figure 4.12: Time sequence of temperature late in the current ramp at  $\phi = 0$ . As islands grow in the plasma, they have a noticeable effect on the temperature profiles. These effects are not as marked as in the current density profiles of figure 4.10, however.

also to the decreased radius of the plasma as seen in figure 4.6. Adding physical limiters similar to those installed on CTH to the NIMROD model is further discussed in Chapter 5.

Continuing to evolve the model, island growth is observed, beginning with an  $\iota = 1/3$  chain of islands forming near the edge of the plasma, seen in figure 4.8b. These islands are symmetry-preserving, meaning that they reflect the five-fold periodicity of the machine. Since they are symmetry preserving, these islands are small and do not appreciably affect the current density or temperature profiles, as shown in figure 4.10b and 4.12b. Once island growth begins in the model, many more islands are observed. Though the islands are initially symmetry-preserving, as seen in figure 4.8b, a symmetry-breaking  $\iota = 1/2$  island follows, as seen in figure 4.8f.

The emergence of islands in the model is accompanied by a growth in the magnetic energy. Illustrated in figure 4.13, the growth of the magnetic energy evolves in two “modes”: one involving the  $n = 5 \pm 1$  toroidal modes and one involving the  $n = 5 \pm 2$  toroidal modes.

Recall from equation 3.17 that the resistivity in NIMROD is modeled as

$$\eta = \text{Max} \left( \text{Min} \left( \eta_0 \left( \frac{T}{T_0} \right)^{-3/2}, \eta_{\text{max}} \right), \eta_{\text{min}} \right). \quad (4.7)$$

By changing the value of  $\eta_0$  just before the magnetic modes begin to grow, it is possible to investigate the resistivity dependence of the mode in an attempt to determine its nature.

Figure 4.16 shows the effect of varying the resistivity on the growth rate of the mode. It is seen that the growth rate varies as  $\gamma \sim \eta^{1/3}$ . This dependence is the same as the resistivity scaling of the growth rate of the resistive interchange mode.<sup>27</sup> Though this scaling dependence suggests that the mode is a resistive interchange mode, it is not conclusive. Magnetic islands are typically associated with the tearing mode, though the growth rate for resistive tearing modes varies as  $\gamma \sim \eta^{3/5}$ .<sup>27</sup> Some tearing modes do not follow this scaling, though, including the double-tearing mode<sup>28</sup> which was seen in the work of Schlutt, et al.<sup>6</sup> A more careful study of the dynamics of the mode, including a detailed investigation of

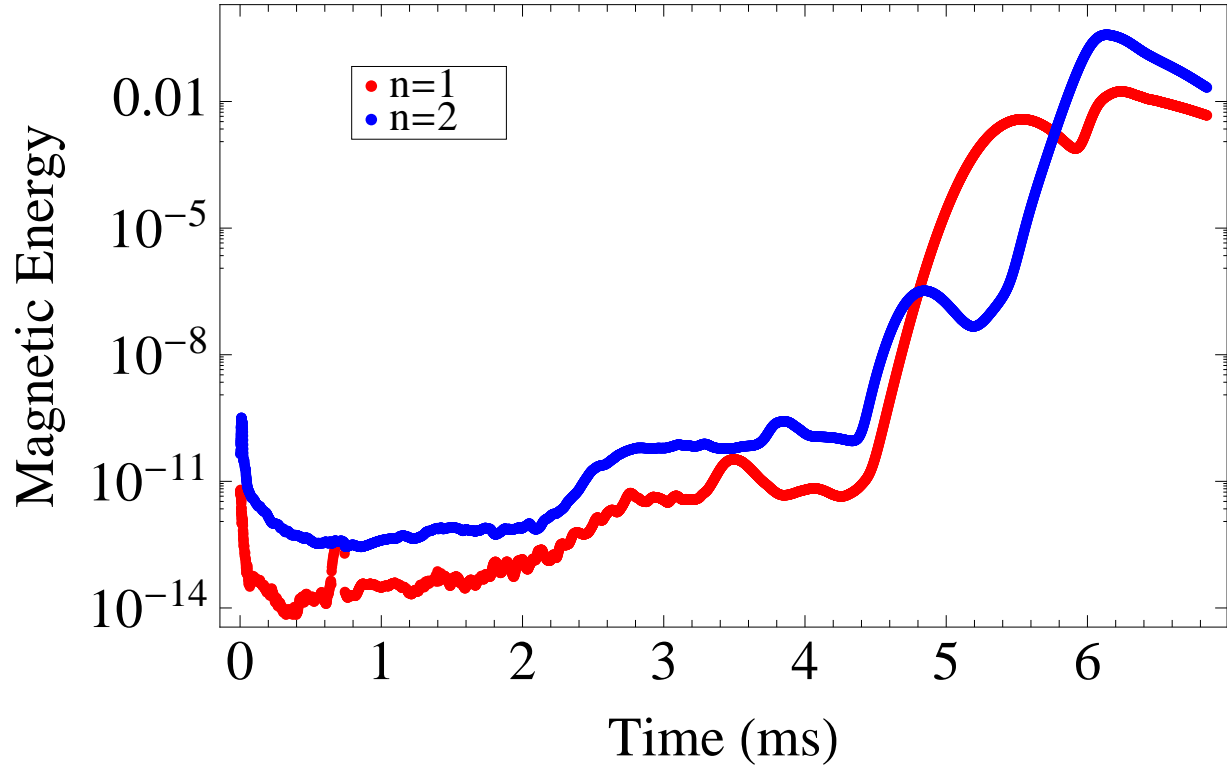


Figure 4.13: Growth of magnetic energy for  $n = 1$  (red) and  $n = 2$  (blue) as a function of time. The magnetic energy growth in these two modes is representative for all modes  $n = 5j \pm 1$  and  $n = 5j \pm 2$  (see figures 4.14 and 4.15). A symmetry-preserving  $m = 15, n = 5$  island is seen beginning at  $t = 4.4$  ms.

the mode onset timing and any physical flows associated with mode growth, is necessary to ascertain the nature of the mode.

Evolving the model further still, a stochastic region emerges near the edge of the plasma when an  $m = 5, n = 2$  island chain appears, as is seen in figure 4.8e. A large,  $t = 1/2$  island chain then grows near the center of the plasma, eventually swamping out the original magnetic axis. This stochastic region and large island chain substantially modify the current density and temperature profiles, as shown in figures 4.10e-f and 4.12e-f.

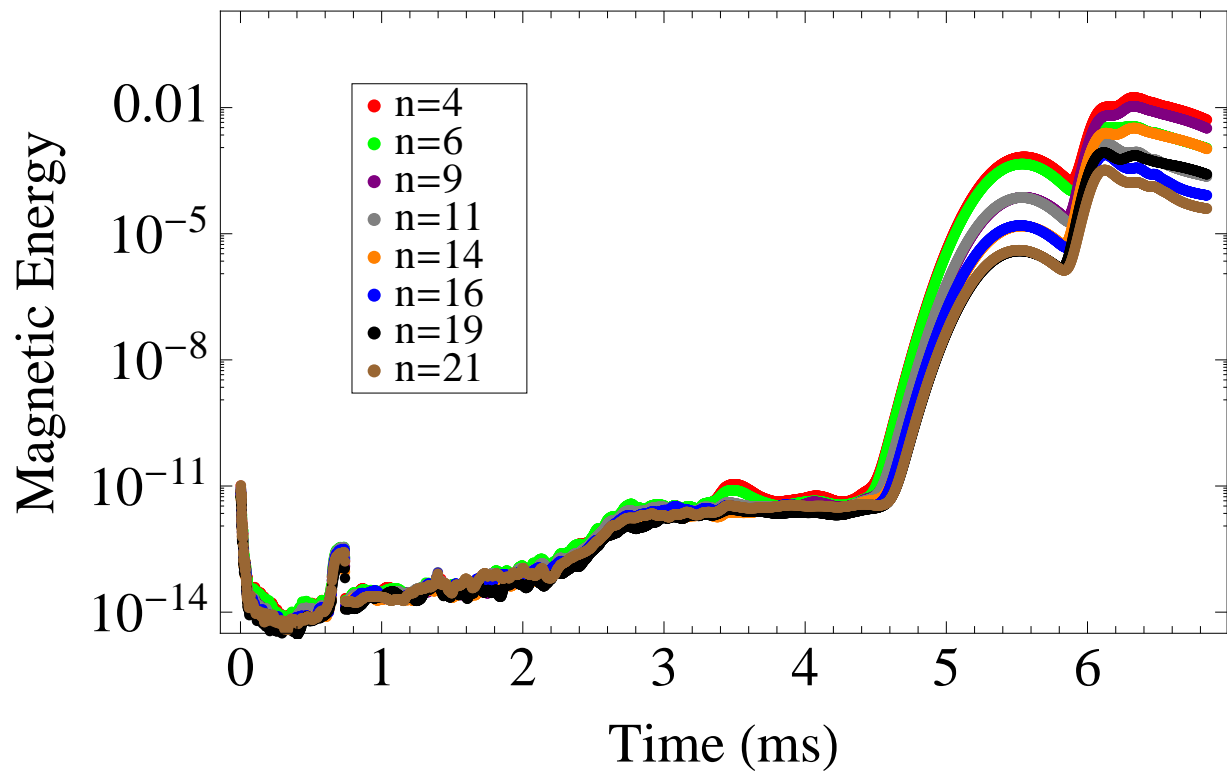


Figure 4.14: Growth of magnetic energy for  $n = 5j \pm 1$  with  $j = 1, 2, 3, 4$ . All of the modes follow behavior similar to the  $n = 1$  toroidal mode, seen in figure 4.13.

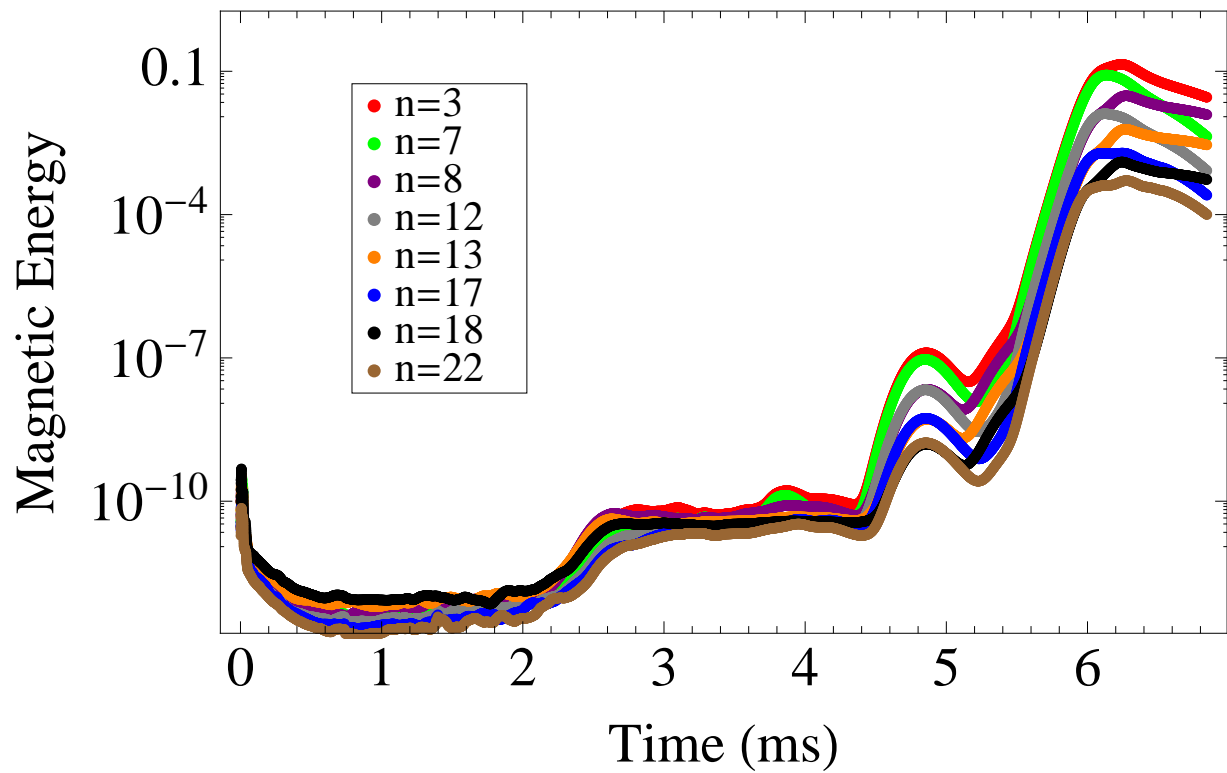


Figure 4.15: Growth of magnetic energy for  $n = 5j \pm 2$  with  $j = 1, 2, 3, 4$ . All of the modes follow behavior similar to the  $n = 2$  toroidal mode, seen in figure 4.13.

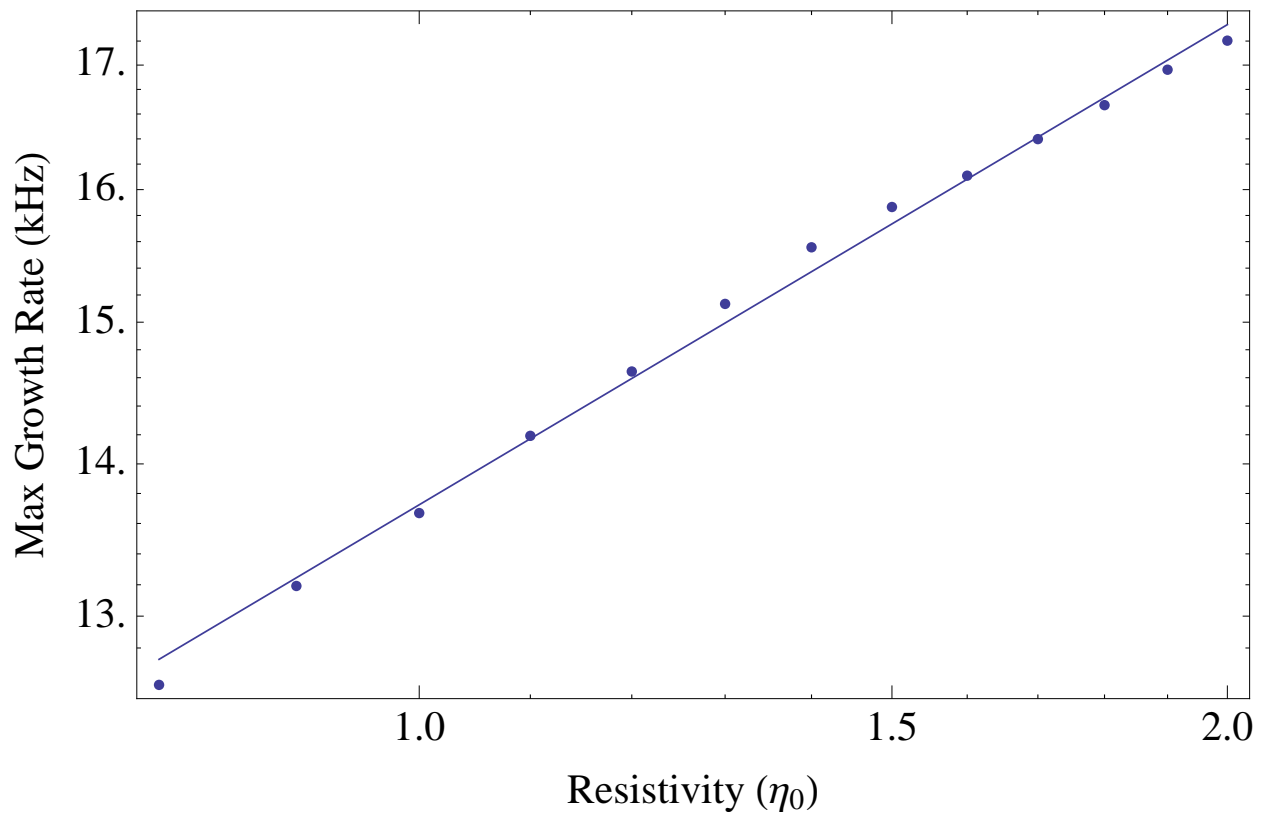


Figure 4.16: Dependence of growth rate of  $n = 5j \pm 1$  magnetic mode on resistivity. The fit line has a slope of  $\gamma = 0.337$ . The growth rate of the observed magnetic mode varies similarly to that of the resistive interchange mode ( $\gamma = \eta^{1/3}$ ).



## 4.2 Constant current investigation of island growth

### 4.2.1 Introduction and motivation

As was seen in the previous section, large island growth is not seen until the rotational transform in the plasma reaches  $\iota = 1/2$ . It is expected, however, that large islands are causing the current hesitations observed in experiment early in time. To investigate whether or not the conditions in the model allow for the growth of large, symmetry breaking islands for rotational transforms  $\iota < 1/2$ , the total plasma current is held constant.

### 4.2.2 Model specifics

In the previous section, the plasma current was calculated self-consistently in the model, with the largest driver being the experimental loop voltage. The most effective way to hold the plasma current constant is to establish a feedback loop in which the loop voltage is altered to give the desired result. Instead of the experimental trace, the loop voltage at any time would then be given by

$$V = V_{\text{old}} + \alpha(\delta t)(I_0 - I) \quad (4.8)$$

where  $V_{\text{old}}$  is the loop voltage at the previous time step,  $\alpha$  is a constant which governs the rate at which the loop voltage can be changed (user defined),  $\delta t$  is the time step, and  $I_0$  is the desired plasma current.

The model will be restarted at a point in time just before the  $\iota = 1/3$  surface has entered the plasma. The  $1/3$  surface is chosen as it is the next lowest order rational surface below  $1/2$  for which symmetry-breaking islands are not observed. Also, if successful, symmetry-breaking  $\iota = 1/3$  surfaces should be quite large. It is necessary to restart the simulation just before the  $\iota = 1/3$  surface enters the plasma due to the fact that, while constant in total, the current density in the plasma will redistribute, increasing the rotational transform.

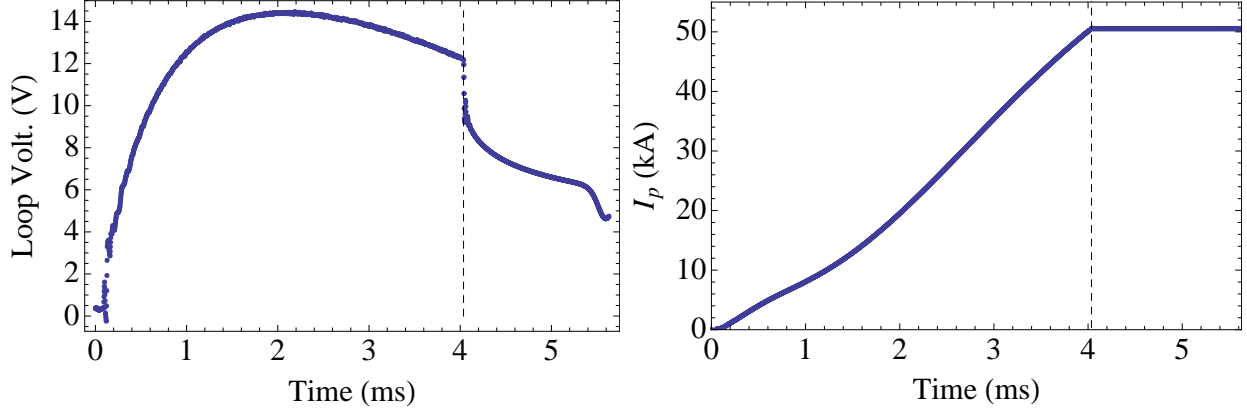


Figure 4.17: Loop voltage (left) and plasma current (right) for simulation holding  $I_p$  constant. The loop voltage control given in equation 4.8 is activated at the dashed line.

### 4.2.3 Presentation of results

To fix the plasma current, the loop voltage drops considerably as can be seen in figure 4.17. Though different in magnitude, this is qualitatively similar to the dips in loop voltage observed during current hesitations in experiment seen in figure 3.5. The fact that the loop voltage drops during these times of constant plasma current makes sense. For a run such as this where the plasma current is held constant, the reduction in loop voltage is caused by the fact that the imposed loop voltage is more than is necessary to drive the desired current. Only a fraction is necessary to maintain the driven current. For the case of current hesitations in experiment, the drop in loop voltage is most likely a result of the changing magnetic structure of the plasma.

A chain of symmetry preserving islands grow at the  $\iota = 1/3$  surface as seen in figure 4.18b. These islands are, initially, similar in size and location to those seen in the previous run. As the current density continues to redistribute, this island chain is pushed toward the edge of the plasma. After further redistribution, this symmetry preserving chain merges in to a large, symmetry breaking chain. This process is illustrated in figure 4.19.

Analogous to figure 4.13, the magnetic energy as a function of time is plotted in figure 4.20. Comparing the times in figure 4.18 with the magnetic energy in figure 4.20, two

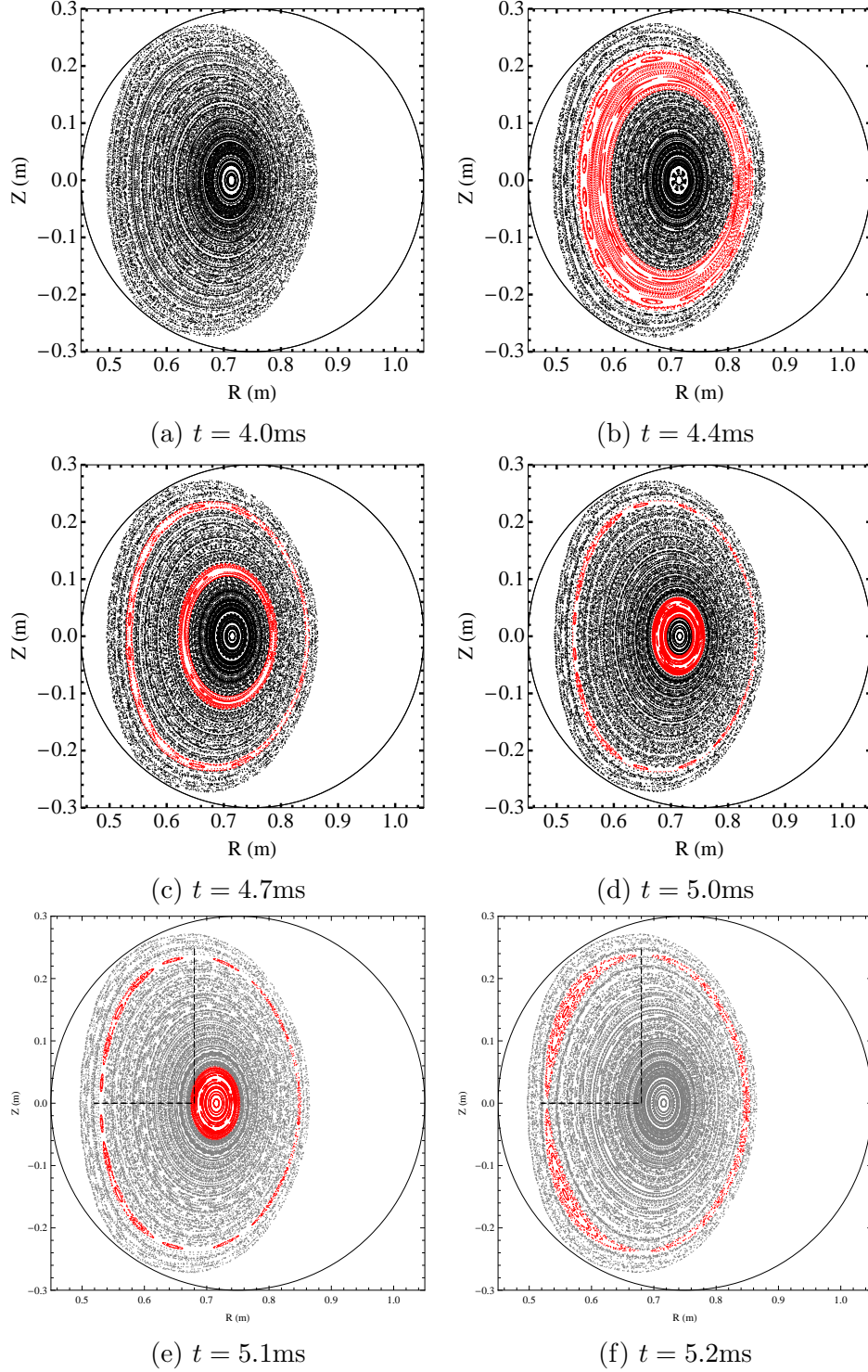


Figure 4.18: Time sequence of surface of section plots at  $\phi = 0$  for constant  $I_p$  simulation showing the growth and merging of  $\iota = 1/3$  islands. Red surfaces have rotational transform  $\iota = 1/3 \pm 0.005$ . (b) The  $\iota = 1/3$  surface enters in a wide band in the middle of the plasma with an  $m = 15, n = 5$  island formed near the edge of that region. (c)-(d) Increasing rotational transform splits the  $\iota = 1/3$  surface in two. (e) The  $m = 15, n = 5$  island begins to merge. (f) The fully merged  $m = 3, n = 1$  island.

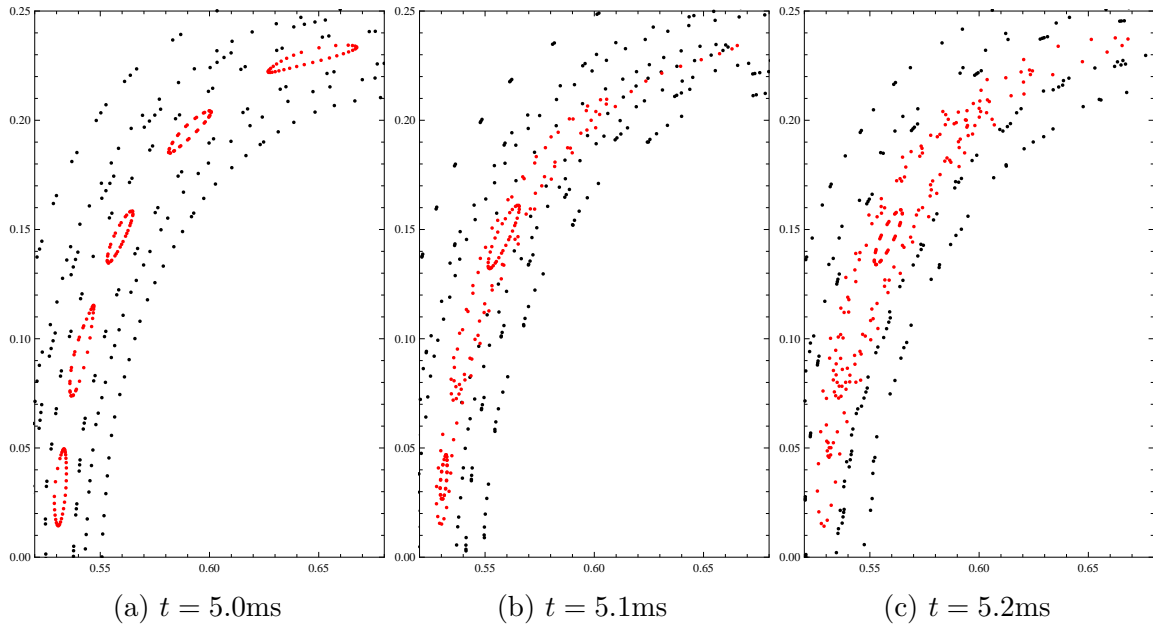


Figure 4.19: Closeup at  $\phi = 0$  of one set of islands merging showing only selected surfaces. Red surfaces have rotational transform  $\iota = 1/3 \pm 0.005$ . (a) The  $\iota = 1/3$  surface forms an  $m = 15, n = 5$  island chain. (b) The chain begins merging, with the middle three islands combining first. (c) The outer islands combine with the inner islands and the  $\iota = 1/3$  surface now forms an  $m = 3, n = 1$  chain.

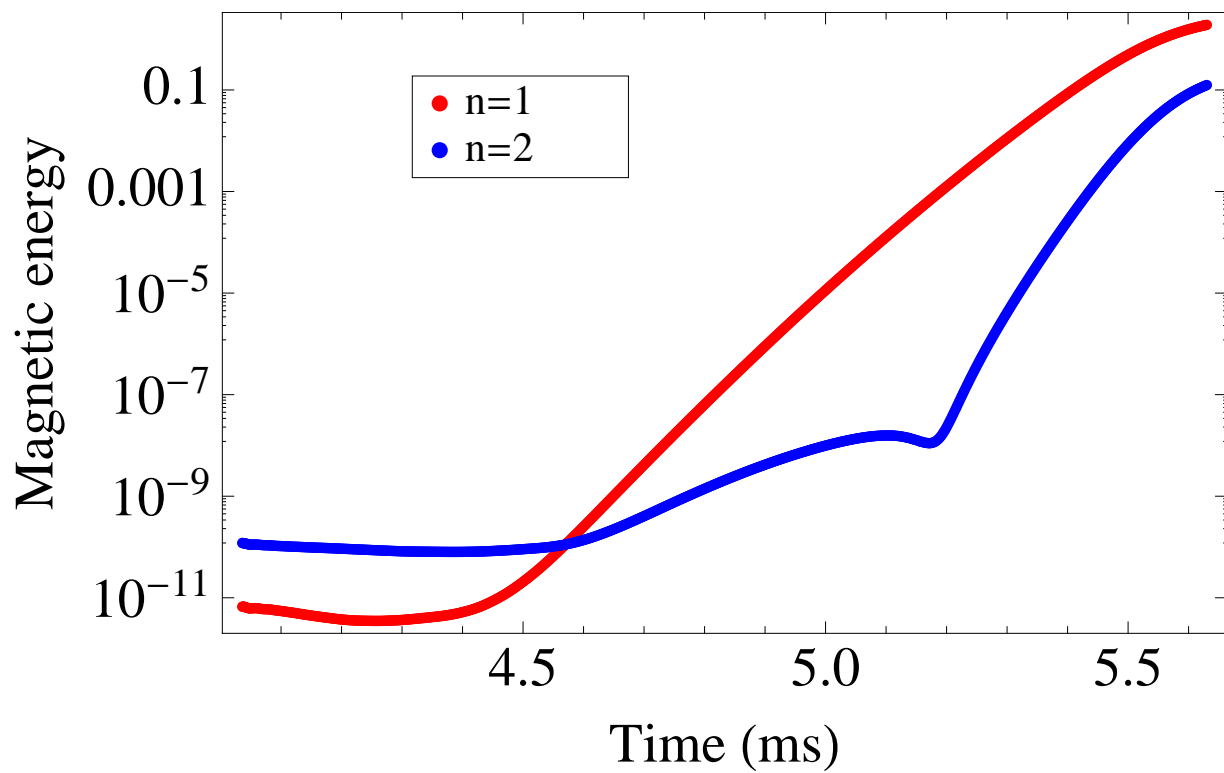


Figure 4.20: Growth of magnetic energy for  $n = 1$  (red) and  $n = 2$  (blue) as a function of time. As in figure 4.13, the magnetic energy growth in these two modes is representative for all modes  $n = 5j \pm 1$  and  $n = 5j \pm 2$ .

observations arise: the presence of symmetry-preserving islands in the plasma volume slightly precedes the increase in magnetic energy in the  $n = 5j \pm 1$  modes, and the growth in the  $n = 5j \pm 2$  mode roughly corresponds to the complete merger of the  $\iota = 1/3$  island chain.

It has been shown through this run that large, symmetry-breaking islands can be formed for  $\iota < 1/2$ . One issue with this run, however, is the time scale over which these islands are formed. In experiment, current hesitations occur over tenths of milliseconds. The process of merging the symmetry-preserving  $m = 15, n = 5$  island chain into the symmetry breaking  $m = 3, n = 1$  chain takes place over the course of milliseconds in the model. This difference in time scales suggests that the current physical model may not be sufficient for modeling the current hesitations. If the hesitations are caused by the merging of symmetry-preserving islands, additional terms may be needed in Ohm's law to speed up the merging time scale. This is discussed further in chapter 5.

### 4.3 Decreasing perpendicular thermal transport

#### 4.3.1 Introduction and motivation

It is expected that the current hesitations in experiment are caused by islands growing near the edge of the plasma. The previous section illustrates that the growth of large, symmetry breaking islands is possible for rotational transforms below  $1/2$ , where symmetry breaking islands were first observed in the initial model. To reproduce current hesitations, then, it may be necessary to have these larger islands in the plasma earlier in time.

One variable which could have a large effect on the formation of islands in the early part of the current ramp is the perpendicular thermal diffusion. Compare, for example, the shape of the current density profiles shown in figure 4.10e and 4.10f to the temperature profiles in figure 4.12e and 4.12f, and note that the temperature profiles are more diffuse than the current density profiles. Since the temperature feeds directly into the current density by way of the temperature dependent resistivity, it is possible that the thermal diffusivity is too high, wiping out any edge perturbations in the temperature and current density early

in the shot which could lead to the development of islands. Since the perpendicular thermal diffusivity is set as a constant, one way to test this is to lower it.

### 4.3.2 Model specifics

Recall that the perpendicular thermal diffusivity was set for temperatures and densities not expected near the edge of the plasma. From equations 3.11 and 3.9, the perpendicular thermal diffusivity varies as  $\kappa_{\perp} \sim n^2$ , making this mismatch in thermal diffusivity a very possible culprit for the lack of hesitations in the model. A perpendicular thermal diffusivity that is set too high would result in a smearing of the temperature over any features on the edge which may lead to island growth early in the shot.

For this simulation, the perpendicular thermal diffusivity is decreased by a factor of 10, which translates to a decrease in the ‘local density’ of  $\sqrt{10} \sim 3$ . Changing only the perpendicular thermal diffusivity causes a sharper rise in the plasma current early in time, as is seen in figure 4.21. To more closely conform to the rate of ohmic current drive in experiment, the maximum temperature was lowered to a value of  $T = 15\text{eV}$ . No other changes were made between this model and the model of section 4.1.

### 4.3.3 Presentation of results

Figure 4.22 shows a comparison of the experimentally observed plasma current and that calculated with NIMROD. As before, the initial rate of ohmic current drive in the model matches well with experiment, even past the point used for comparison when setting the initial temperature. This is further evidence that the manner in which initial density and temperature are set is appropriate for the modeling of this system.

Early in the shot, as is seen in figure 4.24, large symmetry-breaking island chains grow in the plasma. These islands appear first as symmetry-breaking chains, as opposed to merging from symmetry-preserving chains into symmetry-breaking chains as was seen in the previous section. As current is driven and the rotational transform increases, island chains are

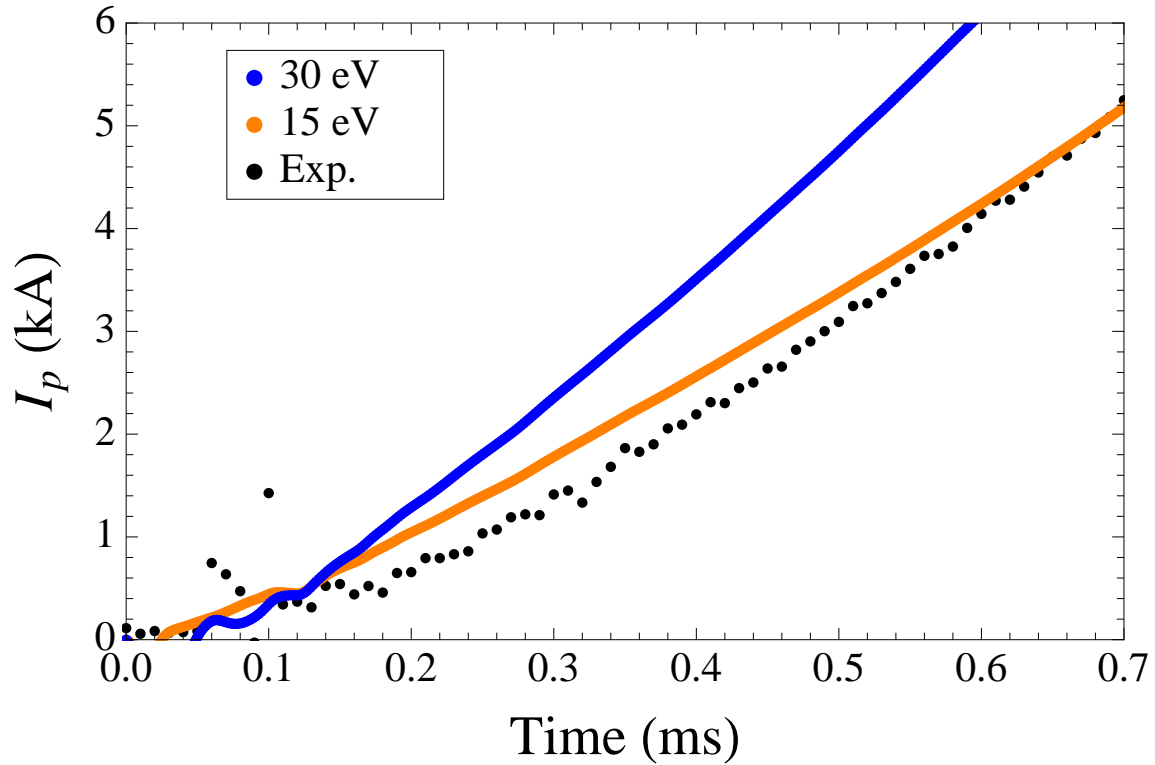


Figure 4.21: Comparison of plasma current from experiment (black) and from NIMROD model with lowered value of perpendicular thermal diffusivity for initial peak temperatures of  $T = 30\text{eV}$  (blue) and  $T = 15\text{eV}$  (orange). The lower  $\kappa_{\perp}$  drives current in the model faster than before. To agree with the rate of plasma current drive in experiment, the peak of the initial temperature profile must be lowered to 15 eV.



observed for all rotational transforms of the form  $1/m$  for  $m = 10$  to  $m = 4$ , when the simulation is halted. These islands have a marked effect on the temperature and current density profiles, as can be seen in figures 4.25 and 4.26.

The growth of these islands is accompanied by a growth in the magnetic energy as was seen in section 4.1. Like that original mode growth, the growth in this case is split chiefly into two modes: one in which the modes with  $n = 5j \pm 1$  grow and one in which the modes with  $n = 5j \pm 2$  grow, as can be seen in figure 4.27.

Using the same method as section 4.1.4, the resistivity is changed just before the onset of the mode growth to determine the dependence of the growth rate on the resistivity. As is seen in figure 4.28, the growth rate of the magnetic energy scales as  $\gamma \sim \eta^{1/3}$ . Again, this suggests that the mode is a resistive interchange mode, but is not conclusive.

Looking closer at the times when these islands occur, it is seen that these times coincide with current hesitations in experiment. Figure 4.23 illustrates this for the first three island chains which are observed in the model, showing times during which the  $\iota = 1/9$ ,  $\iota = 1/8$ , and  $\iota = 1/7$  surfaces are at the edge of the plasma. For the purposes of the figure, the edge of the plasma is defined as the island chain causing a noticeable difference to the plasma shape without having a closed flux surface which surrounds it. Note that, while the currents have diverged by the time the  $\iota = 1/7$  mode has entered the plasma, the time frame observed still matches well with the current hesitation observed in experiment.

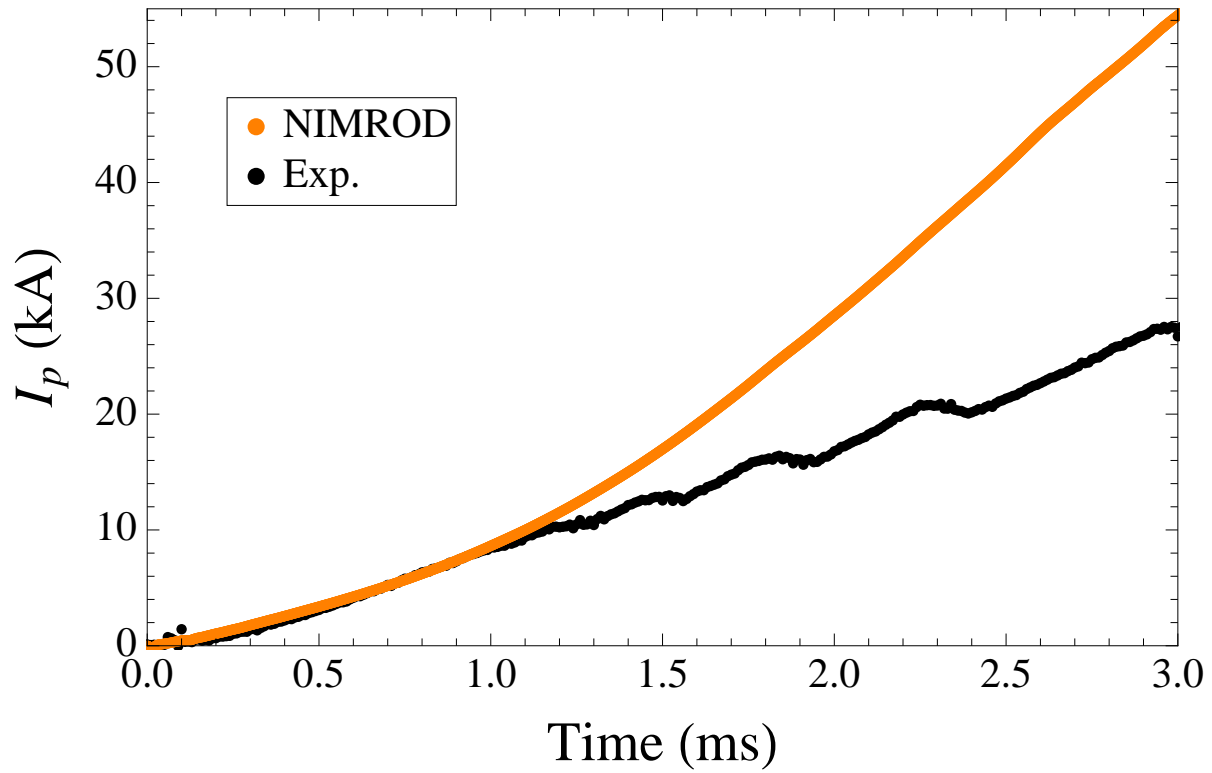


Figure 4.22: Plasma current comparison between experiment (black) and NIMROD model with a lowered value of perpendicular thermal transport (orange). As in 4.5, the NIMROD plasma current matches well early in time with the experimental plasma current. As hesitations are missed in the model, however, the currents diverge.

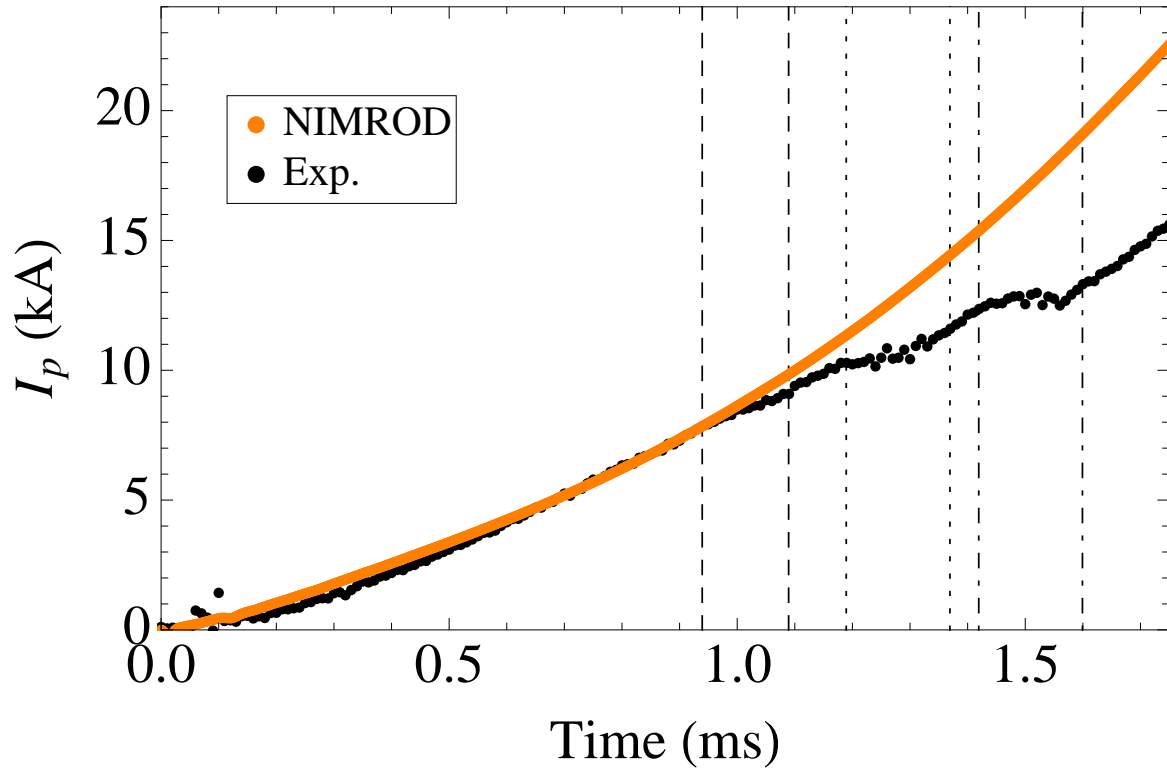


Figure 4.23: Current comparison highlighting times in which the  $\iota = 1/9$  (between dashed lines),  $\iota = 1/8$  (between dotted lines), and  $\iota = 1/7$  (between dot-dashed lines) island chains are at the edge of the plasma. The times when these symmetry breaking islands appear near the edge of the plasma correspond well to the times of early hesitations in experiment.

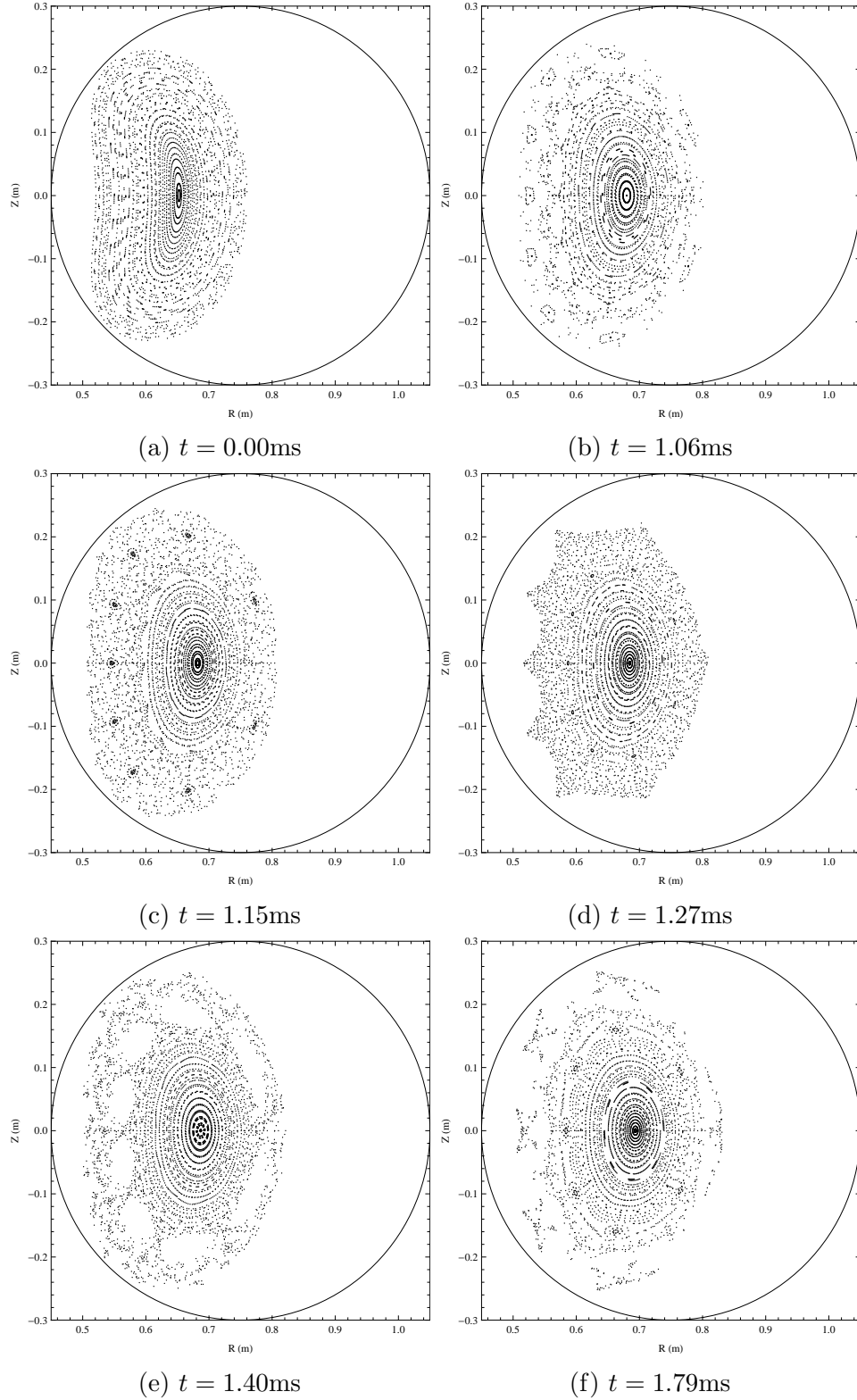


Figure 4.24: Surface of section plots at  $\phi = 0$  for a lower value of perpendicular thermal diffusivity. Symmetry-breaking magnetic islands appear early in the model, with  $\iota = 1/9$  shown in (b)-(c),  $\iota = 1/8$  shown in (d)-(e), and  $\iota = 1/7$  and  $\iota = 1/6$  shown in (f).

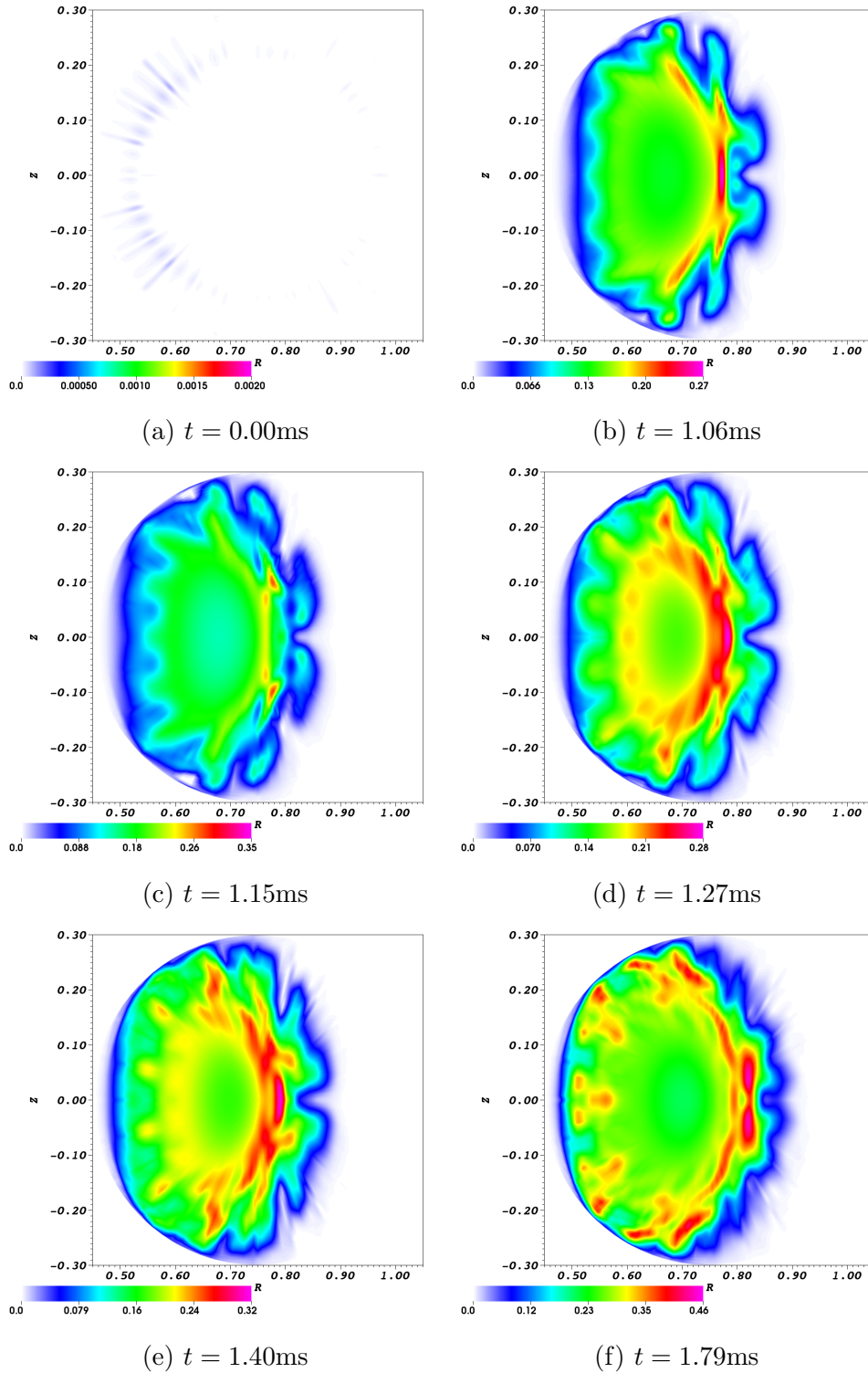


Figure 4.25: Time sequence of current density ( $\lambda = \mu_0 \mathbf{J} \cdot \mathbf{B}/B^2$ ) contours at  $\phi = 0$  for a lower value of perpendicular thermal transport. The current is driven in a hollow profile, similar to figure 4.9, but the profiles are heavily affected by the presence of magnetic islands.

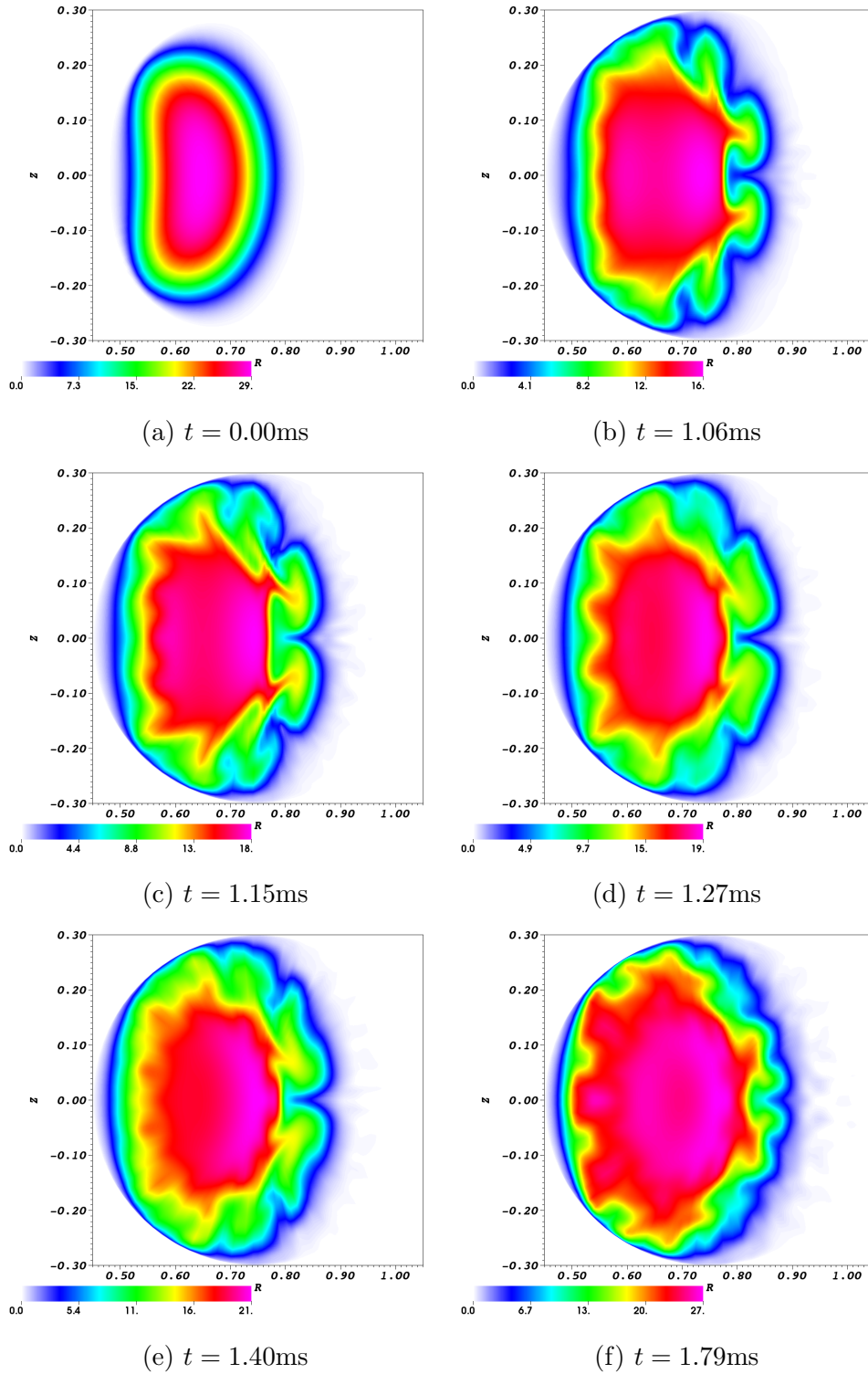


Figure 4.26: Time sequence of temperature contours at  $\phi = 0$  for a lower value of perpendicular thermal transport. The temperature profiles are heavily affected by the presence of magnetic islands. The lower value of  $\kappa_{\perp}$  keeps heat closer to where it is generated, resulting in changing the initially peak profile in (a) to the hollow profile in (f).

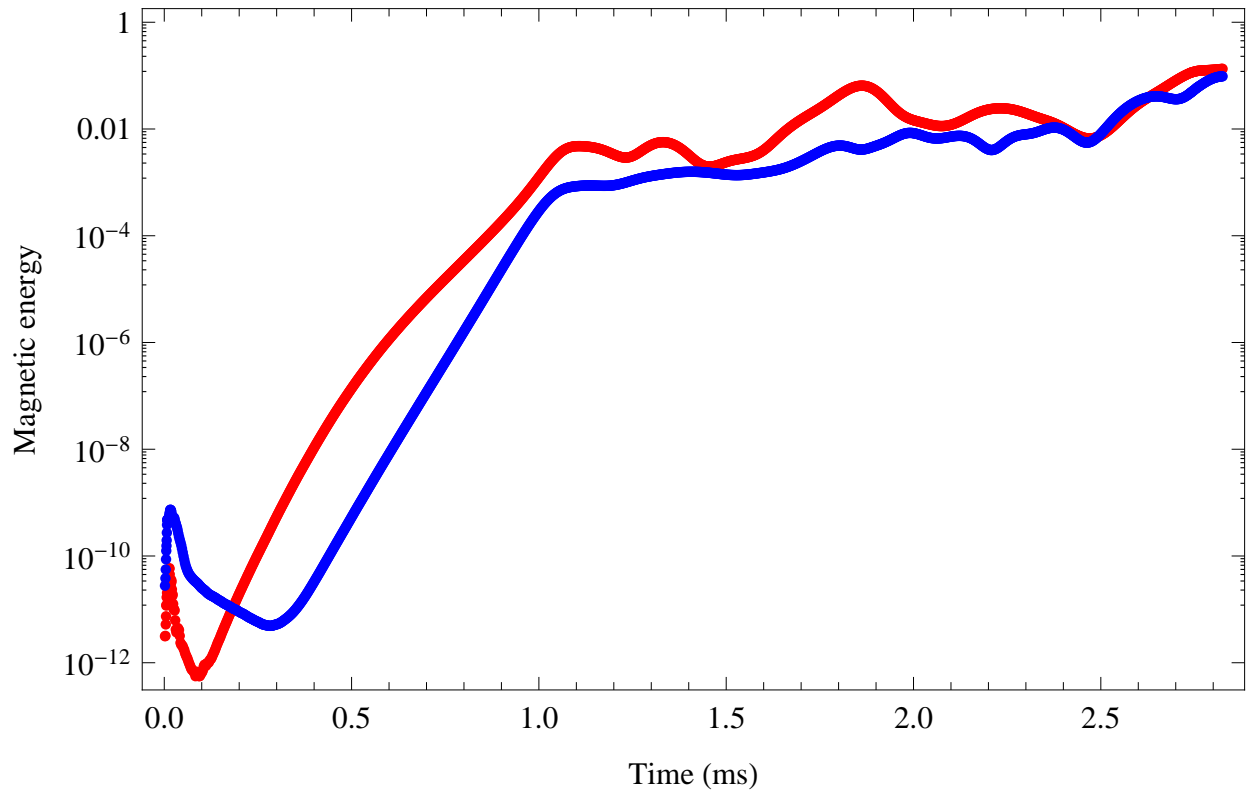


Figure 4.27: Growth of magnetic energy for  $n = 1$  (red) and  $n = 2$  (blue) as a function of time for model with lower value of perpendicular thermal diffusivity. As in figure 4.13, the magnetic energy growth in these two modes is representative for all modes  $n = 5j \pm 1$  and  $n = 5j \pm 2$ .

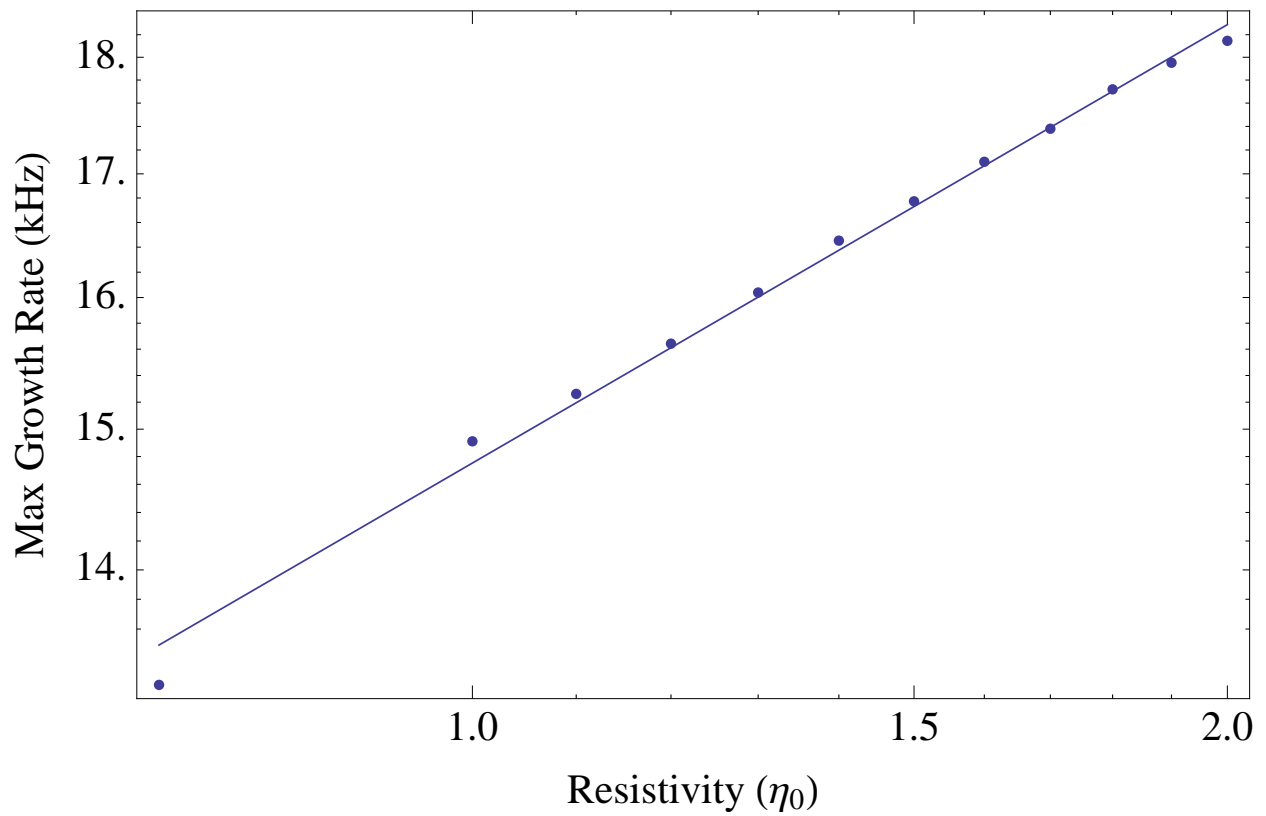


Figure 4.28: Dependence of growth rate of  $n = 5j \pm 1$  magnetic mode on resistivity. The fit line has a slope of  $\gamma = 0.330$ . The growth rate of the observed magnetic mode varies similarly to that of the resistive interchange mode ( $\gamma = \eta^{1/3}$ ).



## Chapter 5

### Results, conclusions, and discussion

#### 5.1 Model changes

For this work, many changes were made to the computational model first implemented by Schlutt et al.<sup>6</sup> The model first used was a simplified “proof of principle” model. In order to bring the model more in line with the physical reality, changes were necessary. The elements added in this work fall into two categories: additional physics and plasma initialization.

##### 5.1.1 Additional physics

Ohmic heating was added as a source of energy in the model. This process occurs in all systems in which current is carried in a resistive medium. The inclusion of this term in the NIMROD model produces heat where current is driven in the model, as is seen in figure 3.2. This constitutes an important first step in realistic modeling in that it steps away from the zero- $\beta$  model used in previous work and provides a path to changing the temperature which, in turn, controls many plasma variables.

As the thermal diffusivity is a function of the plasma temperature, accurate modeling of the current rise phase requires a reflection of this dependence. Thus, a model of the diffusivity reflecting the temperature dependence calculated in the Braginskii model is included. This is implemented in NIMROD as

$$\chi_{\parallel} = \text{Max} \left( \text{Min} \left( \chi_0 \left( \frac{T_0}{T} \right)^{5/2}, \chi_{\text{max}} \right), \chi_{\text{min}} \right) \quad (5.1)$$

where  $\chi_{\parallel}$  is the parallel thermal diffusivity,  $\chi_0$  is the parallel thermal diffusivity calculated for a reference temperature  $T_0$ , and  $\chi_{\max}$  and  $\chi_{\min}$  are the maximum and minimum values of  $\chi_{\parallel}$ .

Like the thermal diffusivity, the resistivity also varies as a function of temperature. Using the Spitzer model, this dependence is represented in the code as

$$\eta = \text{Max} \left( \text{Min} \left( \eta_0 \left( \frac{T}{T_0} \right)^{-3/2}, \eta_{\max} \right), \eta_{\min} \right), \quad (5.2)$$

where  $\eta_0$  is a reference resistivity calculated for a temperature of  $T_0$  and  $\eta_{\max}$  and  $\eta_{\min}$  are the maximum and minimum values, respectively,  $\eta$  is allowed to take. This is a crucial aspect of the model in regards to physical fidelity, as the resistivity is an important control on the rate at which the current is driven.

To accurately model the current rise in the plasma, a time dependent loop voltage was introduced to the model. This loop voltage mimics the driving force of the ohmic transformer installed on CTH, inducing current in the plasma. The loop voltage is measured on the machine, but, if measured during a plasma shot, the resulting trace includes the plasma response. To remove the plasma response and drive current with a loop voltage as seen by the plasma, a separate shot can be taken using the same properties for the ohmic transformer, but with no plasma present. This loop voltage is used in the model.

### 5.1.2 Plasma initialization

CTH plasmas are initially stellarator plasmas heated by ECRH. As such, before the onset of current drive, there is some initial temperature and density profile present. To model this, a uniform temperature is set over the entire domain except for the boundary, which is kept near zero. The temperature equation is advanced in time with  $\chi_{\parallel}/\chi_{\perp} \sim 10^5$  to force heat on open field lines to the perpetually cold boundary while heat on closed field lines remains there. In this way, a nearly uniform temperature is set over the plasma volume,

while the “vacuum” region is set to be cold. The plasma density is then set as a multiple of the temperature.

## 5.2 Computational results

### 5.2.1 CTH model with improvements

Initial modeling of the CTH was carried out using the code changes mentioned previously with physical parameters calculated for  $T = 30\text{eV}$  and  $n = 10^{19}\text{m}^{-3}$  and initial maxima of the temperature and density profiles set accordingly. The temperature used is similar to the temperature previously measured in the stellarator phase of CTH plasmas, but the density is set somewhat higher than the density during that phase to allow for current rise times which are similar to what is seen in experiment.

With these parameters set, the rate of current rise matches quite favorably with experiment early in the shot. This similarity persists beyond the first few current hesitations in the experiment, which are not reproduced in the model. Similarly, the rotational transform profiles match well at these early times, despite the lack of current hesitations in the model. Both the V3FIT reconstructions and the NIMROD model agree that the hesitation seen in experiment occur when the rotational transform at the edge of the plasma is near a low-order rational number.

Early in time, very little distortion in the shape of flux surfaces is observed. As time progresses, however, small islands begin to develop in the plasma column, starting with an  $\iota = 1/3$  chain. While these small island chains have little effect on the temperature and current density profiles, large islands follow shortly after which show a much greater distortion of these profiles. Eventually, a merged  $\iota = 1/2$  island chain emerges, encompassing the original magnetic axis.

As magnetic islands begin to form in the plasma, the magnetic energy begins to spike for off symmetry toroidal modes (that is, modes with  $n \neq 0, 5, 10, \dots$ ). This growth is seen to vary with resistivity as  $\gamma \sim \eta^{1/3}$ , similar to the resistive interchange mode.

### 5.2.2 Constant current run

The hesitations in current drive seen in experiment are expected to be caused by magnetic islands. Initial modeling of the current rise showed a lack of islands in the plasma volume during the hesitations, though large islands were observed much later in time. In order to test that the conditions in the model were appropriate for modeling larger islands for  $\epsilon < 1/2$ , the total plasma current was held constant just before the  $\epsilon = 1/3$  surface entered the plasma by manipulation of the driving loop voltage. This arrangement allowed for the  $\epsilon = 1/3$  surface to remain in the plasma volume for much longer than in the original experiment.

As the  $\epsilon = 1/3$  surface entered the plasma, a small chain of  $m = 15, n = 15$  islands formed. This island chain eventually merged, forming a larger  $m = 3, n = 1$  chain. Though this showed that driving large islands for  $\epsilon < 1/2$  is possible in the model, the time-scale for the formation of the islands was much longer than that seen in experiment.

### 5.2.3 Lower perpendicular thermal conductivity

As the islands which are expected to cause the hesitations in the current rise are thought to be near the edge, the perpendicular thermal conductivity was lowered in an attempt to model that region of the plasma better. The lower thermal conductivity was expected to sharpen the edge gradients by keeping more heat in the plasma volume.

Lowering the perpendicular thermal conductivity proved to have a profound impact on the model. Large, symmetry breaking islands are seen in the plasma volume starting at  $\epsilon = 1/10$ . For the lower values of  $\epsilon$ , the islands are situated near the edge of the plasma at the same time that hesitations are observed in experiment. These islands, in turn, have a large effect on the profile of the current density, distorting the current and providing a possible pathway for the hesitations.

Though large islands were observed early in the current rise, current hesitations were not reproduced in the model. The reason the hesitations were not reproduced is an open

question, but a few possibilities exist which may explain their absence. For example, it is possible that differences in limiter geometry between experiment and model could lead to artificially longer energy confinement times in the model. Also, this work was carried out using a single-fluid model. The effects which cause the hesitations may be due to two-fluid effects, such as an increased growth rate in the islands or the disparity in the temperature of the two fluids. Further, energy loss mechanisms such as ionization of and radiation from background neutrals and impurities were not considered in this work but may play a role in the evolution of the current hesitations.

### 5.3 Further work

As current hesitations were not reproduced in this work, more improvements to the model are necessary to that end. First, recall equations 2.8 and 2.9

$$\vec{E} = -\vec{v} \times \vec{B} + \eta \vec{J} + \frac{1}{ne} \vec{J} \times \vec{B} + \frac{m_e}{n_e^2} \left[ \frac{\partial \vec{J}}{\partial t} + \nabla \cdot (\vec{J} \vec{v} + \vec{v} \vec{J}) - \frac{e}{m_e} (\nabla p_e + \nabla \cdot \overset{\leftrightarrow}{\Pi}_e) \right], \quad (5.3)$$

$$\vec{E} = -\vec{v} \times \vec{B} + \eta \vec{J}. \quad (5.4)$$

By limiting the model to a single-fluid model, there are many terms that are being disregarded. The Hall term ( $\frac{1}{ne} \vec{J} \times \vec{B}$ ), for example has been shown to increase the growth rate of some instabilities.<sup>29</sup> The inclusion of this term may result in the speeding up of time-scales in the model and allow the islands to grow more, and thus disturb the plasma more profoundly, before they propagate away from the edge.

In this work, the plasma size was constrained by the vacuum vessel. The experiment, however, contains carbon, molybdenum, and stainless steel blocks which serve to limit the extent of the plasma before it reaches the vacuum vessel. This reduced plasma radius may have a dramatic effect on the behavior of the plasma. As is seen in figure 4.25, the current density is heavily modified by the presence of magnetic islands in the model. Figure 5.1 shows the location of the physical limiter in the experiment overlaid on the current density of figure

4.25d at the appropriate poloidal angle. Notice that the current at the edge which is being modified by the magnetic islands is now limited much sooner than the model assumption of being limited on the vacuum vessel.

During an ohmic shot, currents are driven in the CTH vacuum vessel and the frame which holds the helical coil due to the pulsing of the ohmic transformer. These currents produce an error field in the experiment which is not present in the NIMROD model. The structure of this field is complicated by the fact that the CTH vacuum vessel is not a perfect torus, but has large ports protruding from it. Though accurate modeling of this error field is difficult it may be necessary, as error fields can seed magnetic islands in the plasma.

Finally, since much of the physics of interest to fusion research happens much later in the discharge, it may be preferential to initialize the model at that later point and evolve from there. This method would avoid many of the difficulties encountered in this work and would make for a more robust use of the model, as effects present in the experiment during the initial stages of a discharge which are not conducive to being modeled by an MHD code (such as ionization of background neutrals) would not negatively effect the physical fidelity of the model. Work is currently being undertaken at Auburn University to this end.

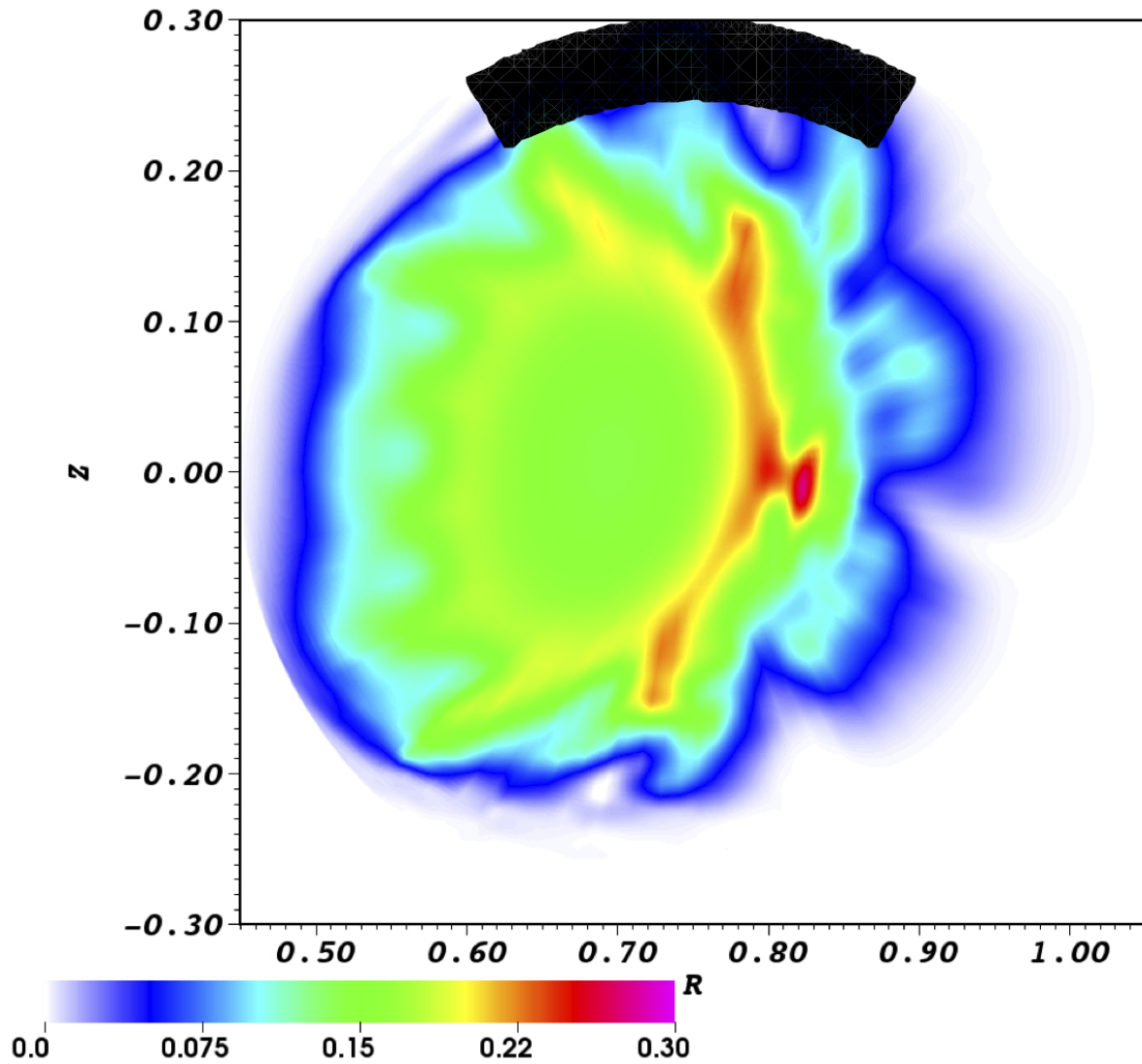


Figure 5.1: Location and extent of molybdenum limiter at  $\phi = 348^\circ$  overlaid on current density ( $\lambda = \mu_0 \mathbf{J} \cdot \mathbf{B} / B^2$ ) contours at the same angle. Note the overlap of the limiter and the plasma current. This shorter path to the boundary could reduce the driven plasma current, possibly producing hesitations.

## Appendices



## Appendix A

### Synthetic Diagnostics - NIMNOSTICS

#### A.1 Introduction

A major hurdle in comparing the results of experiment and model has been the differences in the data that each produces. Modeling results are usually profiles of basic plasma physics variables ( $\vec{J}$ ,  $\vec{B}$ , etc.). Data from experiment is typically a localized measure of plasma properties indirectly related to those basic variables. The goal of a synthetic diagnostic is to produce the signal the experimental diagnostic would produce, given a plasma state defined by the model. In this way, experiment and model can compare like quantities.

Using synthetic diagnostics to compare experiment and model is not a new idea. Currently, synthetic diagnostics are being developed for use with many codes and experiments.<sup>30</sup> Equilibrium reconstruction codes, such as V3FIT,<sup>12</sup> routinely use synthetic diagnostics in their calculations.

This appendix outlines a standardized system of synthetic diagnostics developed independently of code base. This approach allows for a more robust and expedient development of synthetic diagnostic signals while broadening their application and giving independent code bases access to these tools.

#### A.2 Code structure

NIMNOSTICS is a group of scripts written in Python geared to facilitating the use of synthetic diagnostics through a unified format. There are two parts to a synthetic diagnostic signal: the representation of the diagnostic, which includes all of the conversions needed to calculate the expected signal from the model output, and the output of the plasma model.

In NIMNOSTICS these two essential parts are divorced completely, making it easy to use diagnostics which have already been modeled on output from different models.

Model representations in NIMNOSTICS are self contained Python classes which extend the base class `model`. These classes can be structured however is most convenient, with the only caveat being that there is a method named `get_data` which takes as arguments the plasma variable to calculate and the Cartesian point at which to calculate it. `get_data` should return the plasma variable requested (with vector quantities in cartesian representation) and should be the only method which needs to be called after initialization to obtain data. The base class has a place-holder method built in which returns an error if not replaced in the model definition. All input (passing file names, opening files, pre-calculations, etc.) should be done in the inherent `__init__` method. All output from the model class should be in Cartesian coordinates.

Similarly, diagnostics in NIMNOSTICS are self contained Python classes which extend the base class `diagnostic`. The only requirements for these classes are that there is a method `get_signal` which takes as an argument the model from which to calculate a signal. The base class has a place-holder method build in which returns an error if not replaced in the diagnostic definition.

### A.3 Example

While the specifics of diagnostics change from machine to machine, the underlying mathematics which governs the behavior of the diagnostics should not change. Since this is the case, it is useful to define first basic diagnostic classes and then later specify the diagnostic for a particular use. As an example, take the three-chord interferometer installed on CTH and used in chapter 4. At the core of the diagnostic is a line-integrated density measurement. This measurement can be modeled as

$$n_{\text{experiment}} = \frac{\int_{\vec{r}_i}^{\vec{r}_f} n_{\text{model}}(\vec{r}) d\vec{r}}{|\vec{r}_f - \vec{r}_i|} \quad (\text{A.1})$$

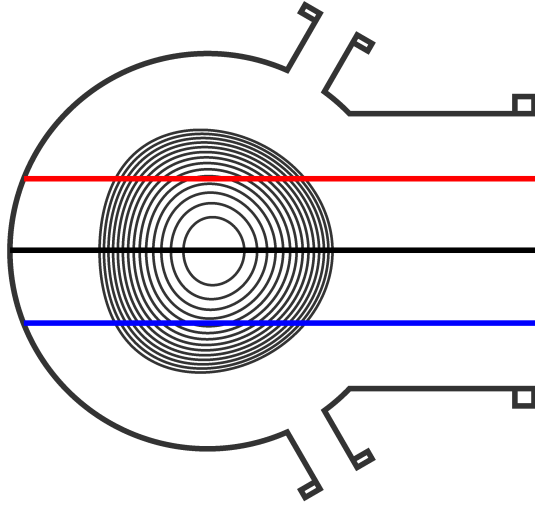


Figure A.1: Chords of the three-channel interferometer on CTH.

where  $n_{\text{experiment}}$  is the line-integrated density measurement as would be seen in experiment and  $n_{\text{model}}(\vec{r})$  is the density from the model. Note that this model is completely independent of the fact that this is a measurement on CTH; this model is simply for a line-integrated density.

To localize this measurement to CTH requires knowledge of the exact location of the diagnostic on the machine. With that knowledge, it is easy to set up the three chords as they are on CTH. This has been done for the simulations presented here. Namely, when setting the initial density, an ad hoc density source was considered to imitate the increasing density seen in figure 4.2b. Though the density source did not prove useful, the application of NIMNOSTICS to the problem was valuable, reproducing line averaged density traces used to set the density ramp rate.

## Appendix B

### NIMROD Calculation of Rotational Transform

The calculation of the rotational transform is a very important step in understanding the structure of a plasma. A method for calculating the rotational transform had been implemented in NIMROD, but would fail to accurately calculate the rotational transform near the magnetic axis. In the course of this work, an improved method for calculating the rotational transform was included in the NIMROD suite, described here.

The process described here proceeds in the following steps:

1. Field lines are separated into two groups: those which remain in the boundary for the duration of the integration (i.e. closed field lines) and those which exit the boundary (i.e. open field lines); open field lines are discarded
2. The centroid of each field line is calculated
3. The maximum distance between a field line's centroid and a point on that field line is calculated; the centroid of field line with the shortest maximum distance is chosen to represent the magnetic axis
4. A "poloidal" angle is calculated around the magnetic axis for each point in a field line, accumulating factors of  $2\pi$  along the way
5. The resulting data is fit to a truncated Fourier series plus a linear term; the magnitude of the linear term is the rotational transform

The Fourier series was truncated at third order in this work as the higher order terms did not appreciably improve the calculation.

## B.1 Separation of field lines

In the normal course of field line tracing in NIMROD, lines are advanced until one of three stopping criteria is achieved: 1) the field line exits the computational domain, 2) the field line reaches a set terminal length, 3) the field line crosses the initial plane a terminal number of times. Field lines which exit the computational domain are both uninteresting and may result in the calculation of the magnetic axis to be thrown off. To avoid that complication, these field lines are removed from the calculation. These field lines are identified by the fact that the field lines are stored in array with a fixed length. When this array is initialized, a large, positive value is set as the data at each point, larger than would be calculated in the normal course of field line tracing. Immediately after the field line exits the domain, integration is halted along that field line and the remainder of the array is unchanged. Thus, comparing the maximum value in the field line arrays to the initialized value, it is possible to discover field lines which left the computational domain.

## B.2 Centroid calculation

After the field lines which cross the boundary are separated from those which stay inside the boundary, the centroid of each retained orbit is calculated. This is done by means of a simple average in  $r$  and  $z$

$$r_{\text{cent}} = \frac{1}{N} \sum_{i=1}^N r_i, \quad (\text{B.1})$$

$$z_{\text{cent}} = \frac{1}{N} \sum_{i=1}^N z_i \quad (\text{B.2})$$

where  $N$  is the number of points in an orbit,  $r_i$  is the  $r$  coordinate of the  $i$ -th point in the orbit and  $z_i$  is the  $z$  coordinate.

### B.3 Magnetic axis choice

For each orbit, the distance between each point on that orbit and the centroid previously calculated for that orbit is calculated. The maximum distance for each orbit is then compared to that of each other orbit and the orbit with the smallest maximum difference is assumed to be closest to the magnetic axis. The centroid calculated for this orbit is chosen as the magnetic axis.

### B.4 Calculation of “poloidal” angle

After the magnetic axis is determined, the orbits are moved to be centered around it. Then, setting the positive x-axis as  $\theta = 0$ , a pseudo-poloidal angle is calculated for each point on the orbit. In this calculation, factors of  $2\pi$  are preserved each time the orbit passes the positive x-axis.

### B.5 Calculation of rotational transform

With the “poloidal” angle tabulated, the rotational transform can be calculated. Figure B.1 shows the poloidal angle as a function of puncture number for an example orbit on a CTH surface of section plot. In a cylindrical system with circular flux surfaces, this plot would be a straight line, and the slope divided by  $2\pi$  would be the rotational transform. As CTH is a toroidal machine with decidedly non-circular flux surfaces, the poloidal angle calculated varies non-linearly. While the rotational transform is still just the underlying slope of the plot divided by  $2\pi$ , to obtain a better estimate of the rotational transform it is useful to fit the trace to a higher order function in order to minimize the effects of the wiggles. Thus, the poloidal angle is fit to the function

$$\theta = c + \iota x + \sum_{n=1}^3 a_n \cos(nx) + \sum_{n=1}^3 b_n \sin(nx) \quad (\text{B.3})$$

where  $x$  is the puncture number and the rotational transform is given as  $\iota = \iota/2\pi$ .

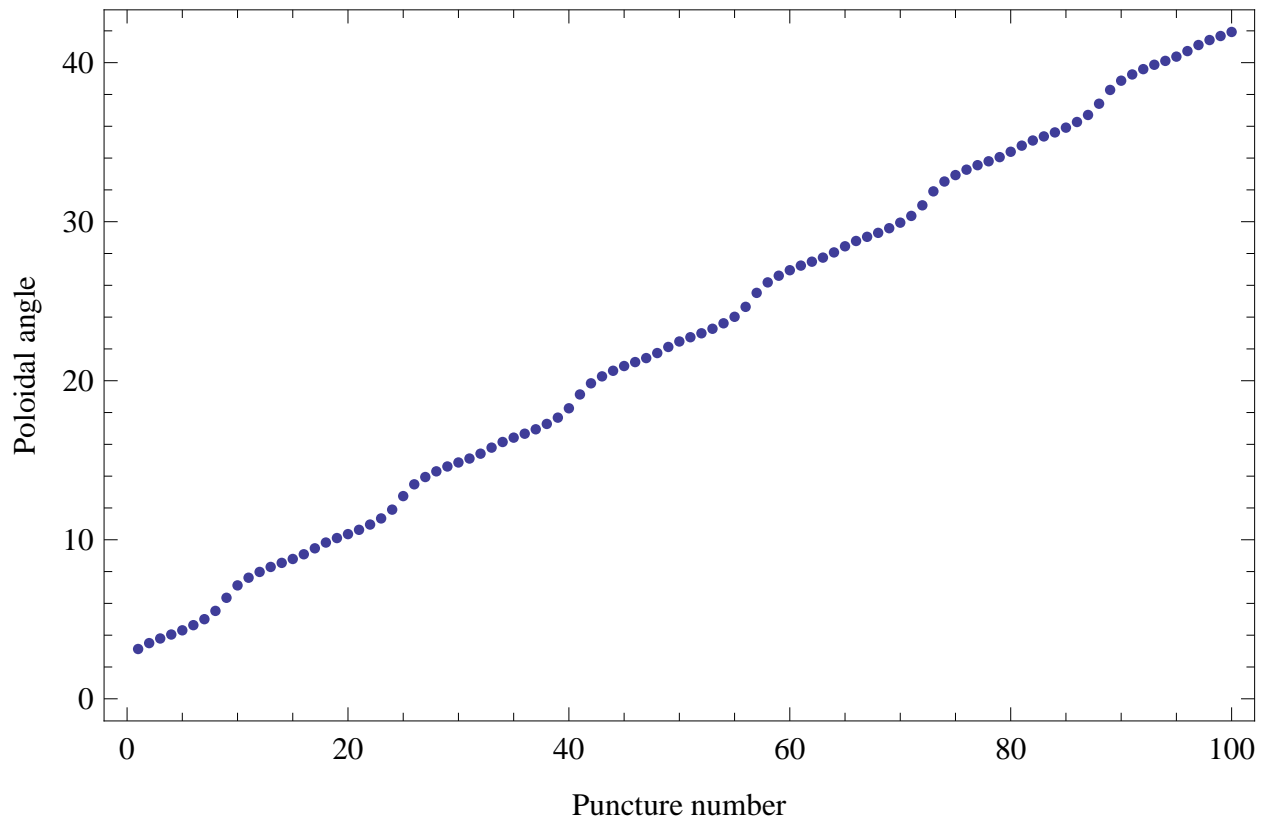


Figure B.1: “Poloidal” angle as a function of puncture number

## Appendix C

### Using NIMROD to model CTH

This appendix serves as a guide for using NIMROD to model CTH as was done in this work. It assumes a small amount of knowledge of the NIMROD suite of codes.

#### C.1 Initial magnetic field

##### C.1.1 mgrid

Creating the file which contains the magnetic field normal to the vacuum vessel at the boundary requires access to the mgrid code. This code will calculate the field using a filamentary model of the CTH coils, given in a “cth-dot” file. The current in the coils is then given as input to mgrid through a name-list input file of the following form:

```
&MGRID_NLI  
TASK='CIRC_TOR_MGRID'  
MGRID_EXT='cth.18b.mo.f5sa'  
RMAJOR=0.75  
AMINOR=0.30  
NPFI=100  
NTHETA=32  
EXTCUR_MGRID(1)=3145.45  
EXTCUR_MGRID(2)=724.67  
EXTCUR_MGRID(3)=96.56  
EXTCUR_MGRID(4)=-250.73  
EXTCUR_MGRID(5)=0
```



EXTCUR\_MGRID(6)=-1366.22

EXTCUR\_MGRID(7)=0

EXTCUR\_MGRID(8)=0/

Here MGRID\_EXT is the file which contains the model of the CTH coils, RMAJOR and RMINOR set the major and minor radii of the CTH torus, NPHI determines the number of toroidal modes, NTHETA determines the number of poloidal modes, and EXTCUR\_MGRID(\*) are the currents in each of the coils described in MGRID\_EXT. Mgrid will produce a file with the named “ctg.” the value of MGRID\_EXT (in this case “ctg.cth.18b.mo.f5sa”). To use the freshly produced file from mgrid in NIMROD, rename it to “cth.txt” and delete the header material (the first line of “cth.txt” should be numbers).

### C.1.2 Importing to NIMROD

The NIMROD input file is an extensive list of name-lists. While it is best to familiarize oneself with most of the options available, a full rundown of all of the variables is not the intent of this document. As such, only the important variables will be discussed here, and will be divided into their respective name-lists.

NIMROD Variable	Explanation	Value
gridshape	2D shape of the grid	'rect'
geom	periodic shape of the domain	'tor'
xo	major radius of grid	0.75
xmas	minor radius of grid	0.3
mx	# of radial grid points	24
my	# of poloidal grid points	24
poly_degree	polynomial degree of finite elements	5
lphi	# of Fourier modes= $2^{lphi}/3 + 1$	7
poly_distribution	how to space nodes	'gll'

Table C.1: `&grid_input` variables describing the NIMROD mesh

The values in table C.1 reflect those used in this work. They were chosen as a compromise between speed and accuracy. These values do not change throughout the process

of modeling CTH. Figure C.1 shows the poloidal grid produced using the values in table C.1. The uneven spacing of the nodes is due to the use of Gauss-Lobatto spacing (`poly_distribution='gll'`) which can result in better conditioned matrices for the large values of `lphi` necessary for CTH runs.

Setting the magnetic field in NIMROD has two main steps. First, the magnetic field normal to the vacuum vessel is loaded into NIMROD using NIMSET. The important variables for that are as follows:

NIMROD Variable	Explanation	Value
<code>elec_d</code>	electric diffusivity	$10^9$
<code>zero_bnorm</code>	whether or not $ B  = 0$ normal to the vacuum vessel	F

Table C.2: `&physics_input` variables for loading fields into NIMROD

NIMROD Variable	Explanation	Value
<code>dtm</code>	maximum time step	$10^{-13}$
<code>divbd</code>	$\nabla \cdot \vec{B}$ cleaning constant	$10^9$

Table C.3: `&numerical_input` variables for loading fields into NIMROD

NIMROD Variable	Explanation	Value
<code>pert_cos</code>	internal switch on positive/negative	-1
<code>heat_ion_source</code>	internal switch	'stell'

Table C.4: `&closure_input` variables for loading fields into NIMROD

Setting the variables in C.4 tells nimset to run the specific subset of code geared to importing the data from “cth.txt”. After running nimset, a message will appear with a value for a variable called `be0`. That variable sets the value of the magnetic field at the center of the vacuum vessel.

For the second step of the process, change the following variables:

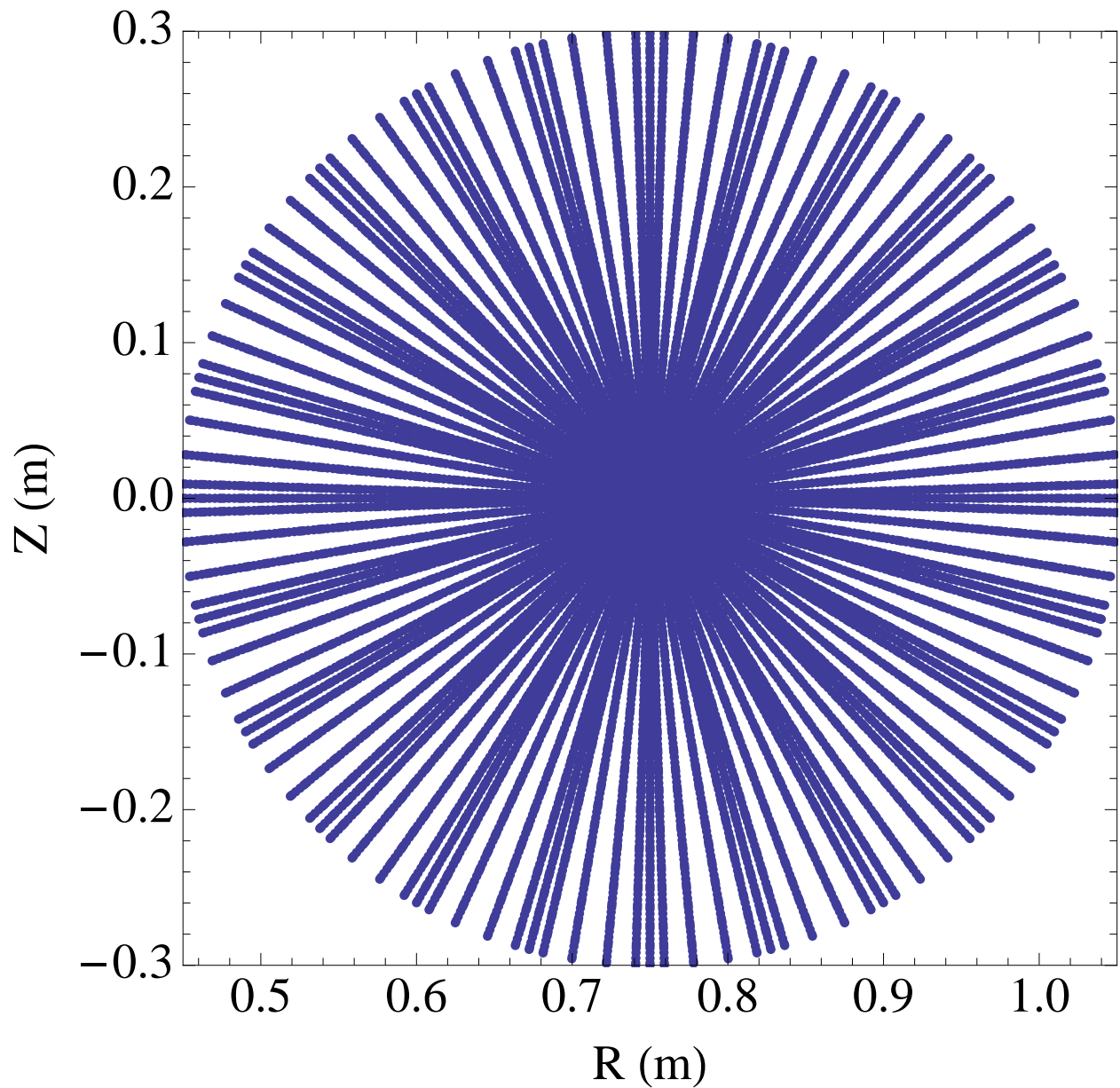


Figure C.1: The NIMROD grid produced by the inputs in table C.1 representing CTH. The uneven spacing of the nodes is due to setting `poly_distribution='gll'`. This setting uses Gauss-Lobatto spacing which can result in better conditioned matrices for the large values of `lphi` necessary for CTH runs.

NIMROD Variable	Explanation	Value
<code>be0</code>	toroidal magnetic field at center of vacuum vessel	0.57749

Table C.5: `&equil_input` variables for setting the initial magnetic field

NIMROD Variable	Explanation	Value
<code>pert_cos</code>	internal switch on positive/negative	-1
<code>heat_ion_source</code>	internal switch	'none'

Table C.6: `&closure_input` variables for setting the initial magnetic field

Note that the value set for `be0` will vary depending on the input fields. Always set it to the value output from `nimset`. Running `nimrod` should diffuse the field into the computational domain. The length of the calculation is controlled by:

NIMROD Variable	Explanation	Value
<code>nstep</code>	maximum number of steps	3500
<code>tmax</code>	maximum value of $t$ in seconds	300

Table C.7: `&numerical_input` variables for controlling the length of the simulation

## C.2 Initial temperature profile

After setting the magnetic field, setting the initial temperature profile follows similarly. First, `nimset` must be called with the following variables:

NIMROD Variable	Explanation	Value
<code>init_type</code>	switch to initialize from previous dump file	'reset'
<code>reset_file</code>	dump file to initialize from	'dump.reset'

Table C.8: `&init_input` variables for resetting from a dump file

`beta` is used to set temperature profiles in `nimset`, so it is set to 0 to avoid complications due to that.

NIMROD Variable	Explanation	Value
<code>be0</code>	toroidal magnetic field at center of vacuum vessel	0.57749
<code>beta</code>	plasma $\beta$	0

Table C.9: `&equil_input` variables for setting an initial temperature profile

NIMROD Variable	Explanation	Value
<code>dtm</code>	maximum time step	$10^{-11}$
<code>divbd</code>	$\nabla \cdot \vec{B}$ cleaning constant	$10^2$

Table C.10: `&numerical_input` variables for setting an initial temperature profile

NIMROD Variable	Explanation	Value
<code>pert_cos</code>	internal switch on positive/negative	-1
<code>heat_ion_source</code>	internal switch	'stell'
<code>set_eq_temp</code>	internal switch	T
<code>odd_pert_str</code>	$T_e$ in eV to be set everywhere but boundary	30

Table C.11: `&closure_input` variables for setting an initial temperature profile

Running `nimset` under these conditions will set the electron temperature to 30eV everywhere except the boundary, which will remain at 0eV. To propagate the temperature, a few switches must be thrown.

NIMROD Variable	Explanation	Value
<code>be0</code>	toroidal magnetic field at center of vacuum vessel	0.57749
<code>beta</code>	plasma $\beta$	1

Table C.12: `&equil_input` variables for advancing an initial temperature profile

Note that the value of `beta` here will not make any difference to the evolution as long as it is positive; if `beta` is zero, `nimrod` will not advance the temperature.

The values of `k_perp` and `k_p11` may be adjusted to the user's needs. After setting these values, running `nimrod` will advance the temperature. When the initial temperature is at a satisfactory state, it is advisable to set `eqn_model='all'` (the default value) so that all of the plasma variables are advanced.

NIMROD Variable	Explanation	Value
pert_cos	internal switch on positive/negative	-1
heat_ion_source	internal switch	'none'
set_eq_temp	internal switch	T
odd_pert_str	$T_e$ in eV to be set everywhere but boundary	30
eqn_model	variable to advance	'T'
k_perp	perpendicular thermal diffusivity	$10^5$
k_pll	parallel thermal diffusivity	$10^{10}$
p_model	model for thermal diffusivity	'anisol'

Table C.13: `&closure_input` variables for advancing an initial temperature profile

### C.3 Initial density profile

The initial density is set very similarly to the initial temperature. To set the initial density, run `nimset` with the following parameters:

NIMROD Variable	Explanation	Value
init_type	switch to initialize from previous dump file	'reset'
reset_file	dump file to initialize from	'dump.reset'

Table C.14: `&init_input` variables for resetting from a dump file

NIMROD Variable	Explanation	Value
be0	toroidal magnetic field at center of vacuum vessel	0.57749
beta	plasma $\beta$	0
ndens	maximum density	$10^{19}$

Table C.15: `&equil_input` variables for setting an initial density profile

NIMROD Variable	Explanation	Value
pert_cos	internal switch on positive/negative	-1
heat_ion_source	internal switch	'stell'
set_eq_temp	internal switch	T
odd_pert_str	$T_e$ in eV to be set everywhere but boundary	30
set_eq_nd	internal switch	T

Table C.16: `&closure_input` variables for setting an initial density profile

## C.4 Final suggestions

As there are many switches which get toggled while setting up a CTH model in NIMROD, there are many easy mistakes to make in an input file. Below are tables of the proper settings for a NIMROD run of interest and possible symptoms which may arise from using incorrect settings:

NIMROD Variable	Name-list	Value	Symptom
<code>be0</code>	<code>&amp;equil_input</code>	see output of <code>nimset</code> in C.1.2	magnetic fields misaligned
<code>beta</code>	<code>&amp;equil_input</code>	1	temperature not evolving
<code>heat_ion_source</code>	<code>&amp;closure_input</code>	'none'	anomalous heating

Table C.17: Common pitfall variables

## Bibliography

- <sup>1</sup> T. E. Evans, R. A. Moyer, P. R. Thomas, J. G. Watkins, T. H. Osborne, J. A. Boedo, E. J. Doyle, M. E. Fenstermacher, K. H. Finken, R. J. Groebner, M. Groth, J. H. Harris, R. J. La Haye, C. J. Lasnier, S. Masuzaki, N. Ohyaabu, D. G. Pretty, T. L. Rhodes, H. Reimerdes, D. L. Rudakov, M. J. Schaffer, G. Wang, and L. Zeng. Suppression of Large Edge-Localized Modes in High-Confinement DIII-D Plasmas with a Stochastic Magnetic Boundary. *Physical Review Letters*, 92(23), 2004.
- <sup>2</sup> Y. Liang, H. R. Koslowski, P. R. Thomas, E. Nardon, B. Alper, P. Andrew, Y. Andrew, G. Arnoux, Y. Baranov, M. Becoulet, M. Beurskens, T. Biewer, M. Bigi, K. Crombe, E. De La Luna, P. de Vries, W. Fundamenski, S. Gerasimov, C. Giroud, M. P. Gryaznevich, N. Hawkes, S. Hotchin, D. Howell, S. Jachmich, V. Kiptily, L. Moreira, V. Parail, S. D. Pinches, E. Rachlew, and O. Zimmermann. Active Control of Type-I Edge-Localized Modes with  $n = 1$  perturbation fields in the JET Tokamak. *Physical Review Letters*, 98(265004), 2007.
- <sup>3</sup> S. A. Sabbagh, J. W. Berkery, R. E. Bell, J. M. Bialek, S. P. Gerhardt, J. E. Menard, R. Betti, D. A. Gates and B. Hu, O. N. Katsuro-Hopkins, B. P. LeBlanc, F. M. Levinton, J. Manickam, K. Tritz, and H. Yuh. Advances in global MHD mode stabilization research on NSTX. *Nuclear Fusion*, 50(025020), 2010.
- <sup>4</sup> M. Okabayashi, J. Bialek, A. Bondeson, M. S. Chance, M. S. Chu, A. M. Garofalo, R. Hatcher, Y. In, G. L. Jackson, R. J. Jayakumar, T. H. Jenson, O. Katsuro-Hopkins, R. J. La Haye, Y. Q. Liu, G. A. Navratil, H. Reimerdes, J. T. Scoville, E. J. Strait, M. Takechi, A. D. Turnbull, P. Gohil, J. S. Kim, M. A. Makowski, J. Manickam, and J. Menard. Control of the resistive wall mode with internal coils in the DIII-D tokamak. *Nuclear Fusion*, 45:1715–1731, 2005.
- <sup>5</sup> C.R. Sovinec, A. H. Glasser, T. A. Gianakon, D. C. Barnes, R. A. Nebel, S. E. Kruger, D. D. Schnack, S. J. Plimpton, A. Tarditi, M. S. Chu, and the NIMROD Team. Non-linear magnetohydrodynamics simulation using high-order finite elements. *Journal of Computational Physics*, 195(1):355–386, March 2004.
- <sup>6</sup> M.G. Schlutt, C.C. Hegna, C.R. Sovinec, S.F. Knowlton, and J.D. Hebert. Numerical simulation of current evolution in the Compact Toroidal Hybrid. *Nuclear Fusion*, 52(103023), 2012.
- <sup>7</sup> E. B. Hooper, C. R. Sovinec, R. Raman, F. Ebrahimi, and J. E. Menard. Resistive MHD simulations of helicity injected startup plasmas in NSTX. *Physics of Plasmas*, 20(092510), 2013.



- <sup>8</sup> V. A. Izzo. Impurity mixing and radiation asymmetry in massive gas injection simulations of DIII-D. *Physics of Plasmas*, 20(056107), 2013.
- <sup>9</sup> J. B. O’Byryan and C.R. Sovinec. Simulated flux-rope evolution during non-inductive startup in Pegasus. *Plasma Physics and Controlled Fusion*, 56(064005), 2014.
- <sup>10</sup> P. Zhu and J. Raeder. Plasmoid formation in current sheet with finite normal magnetic component. *Physical Review Letters*, 110(235005), 2013.
- <sup>11</sup> S. P. Hirshman and J. C. Whitson. Steepest-descent moment method for three-dimensional magnetohydrodynamic equilibria. *Physics of Fluids*, 26(3553), 1983.
- <sup>12</sup> James D. Hanson, Steven P. Hirshman, Stephen F. Knowlton, Lang L. Lao, Edward A. Lazarus, and John M. Shields. V3FIT: a code for three-dimensional equilibrium reconstruction. *Nuclear Fusion*, 49(075031), 2009.
- <sup>13</sup> J. A. Wesson, R. D. Gill, M. Hugon, F. C. Schuller, J. A. Snipes, D. J. Ward, D. V. Bartlett, D. J. Campbell, P. A. Duperrex, A. W. Edwards, R. S. Granetz, N. A. O. Gottardi, T. C. Hender, E. Lazzaro, P. J. Lomas, N. Lopes Cardozo, K. F. Mast, M. F. F. Nave, N. A. Salmon, P. Smeulders, P. R. Thomas, B. J. D. Tubbing, M. F. Turner, and A. Weller. Disruptions in JET. *Nuclear Fusion*, 29(4):641–666, 1989.
- <sup>14</sup> R. S. Granetz, I. H. Hutchinson, and D. O. Overskei. Disruptive MHD Activity During Plasma Current Rise in Alcator A Tokamak. *Nuclear Fusion*, 19(12):1587–1595, 1979.
- <sup>15</sup> A. Scarabosio, A. Ponchelon, and Y. Martin. Plasma shape stabilization of current rise MHD instabilities in TCV. *Plasma Physics and Controlled Fusion*, 49:1041–1060, 2007.
- <sup>16</sup> D. Bonfiglio, S. Cappello, R. Piovan, L. Zanotto, and M. Zuin. 3D nonlinear MHD simulations of ultra-low  $q$  plasmas. *Nuclear Fusion*, 48:12, 2008.
- <sup>17</sup> D. P. Brennan, E. J. Strait, A. D. Turnbull, M. S. Chu, R. J. La Haye, T. C. Luce, T. S. Taylor, S. Kruger, and A. Pletzer. Tearing mode stability studies near ideal stability boundaries in DIII-D. *Physics of Plasmas*, 9(2998), 2002.
- <sup>18</sup> Marco Ariola and Alfredo Pironti. *Magnetic Control of Tokamak Plasmas*. Springer Science and Business Media, 2008.
- <sup>19</sup> M. Shimada, D. J. Campbell, V. Mukhovatov, M. Fujiwara, N Kirneva, K. Lackner, M. Nagami, V. D. Pustovitov, N. Uckand, J. Wesley, N. Asakura, A. E. Costley, A. J. H. Donne, E. J. Doyle, A. Fasoli, C. Gormezano, Y. Gribov, O. Gruber, T. C. Hender, W. Houlberg, S. Ide, Y. Kamada, A. Leonard, B. Lipschultz, A. Loarte, K. Miyamoto, V. Mukhovatov, T. H. Osborne, A. Polevoi, and A. C. C. Sips. Chapter 1: Overview and summary. *Nuclear Fusion*, 47(6), 2007.
- <sup>20</sup> Hans Goedbloed and Stefaan Poedts. *Principles of Magnetohydrodynamics*. Cambridge University Press, 2004.

- <sup>21</sup> Jeffrey Freidberg. *Plasma Physics and Fusion Energy*. Cambridge University Press, 2007.
- <sup>22</sup> Lyman Spitzer. The Stellarator Concept. *Physics of Fluids*, 1:253, 1958.
- <sup>23</sup> M. C. ArchMiller, M. R. Cianciosa, D. A. Ennis, J. D. Hanson, G. J. Hartwell, J. D. Hebert, J. L. Herfindal, S. F. Knowlton, X. Ma, D. A. Maurer, M. D. Pandya, and P. Traverso. Suppression of Vertical Instability in Elongated Current-Carrying Plasmas by Applying Stellarator Rotational Transform. *Physics of Plasmas*, 21(056113), 2014.
- <sup>24</sup> Matthew C. ArchMiller. Plasma Disruption Avoidance and Mitigation using Strong Non-Axisymmetric Shaping with Stellarator Fields. *Bulletin of the American Physical Society*, 58(16):BI2.00004, 2013.
- <sup>25</sup> Jeffrey P. Freidberg. *Ideal MHD*. Cambridge University Press, 2014.
- <sup>26</sup> Lyman Spitzer. *Physics of Fully Ionized Gases*. Interscience, 1956.
- <sup>27</sup> Masahiro Wakatani. *Stellarator and Heliotron Devices*. Oxford University Press, 1998.
- <sup>28</sup> P. L. Pritchett and Y. C. Lee. Linear analysis of the double-tearing mode. *Physics of Fluids*, 23, 1980.
- <sup>29</sup> K. Nykyri and A. Otto. Influence of the Hall term on KH instability and reconnection inside KH vortices. *Annales Geophysicae*, 22(3):935–949, 2004.
- <sup>30</sup> J. C. Rost, L. Lin, and M. Porkolab. Development of a Synthetic Phase Contrast Imaging Diagnostic. *Physics of Plasmas*, 17(062506), 2010.